論文 / 著書情報
Article / Book Information

題目(和文)	
Title(English)	Study of Mirror Kirchhoff Approximation for Predicting Shadowing Gain
著者(和文)	トキン
Author(English)	Xin Du
出典(和文)	学位:博士（工学）, 学位授与機関:東京工業大学, 報告番号:甲第11812号, 授与年月日:2022年3月26日, 学位の種別:課程博士, 審査員:髙田 潤一,髙橋 邦夫,山下 幸彦,秋田 大輔,青柳 貴洋
Citation(English)	Degree:Doctor (Engineering), Conferring organization: Tokyo Institute of Technology, Report number:甲第11812号, Conferred date:2022/3/26, Degree Type:Course doctor, Examiner:,,,,
学位種別(和文)	博士論文
Type(English)	Doctoral Thesis

Study of Mirror Kirchhoff Approximation for Predicting Shadowing Gain

A dissertation submitted in partial fulfillment
of the requirements for the degree of
Doctor of Engineering

by

XIN DU

Supervisor

Professor Jun-ichi Takada

School of Environment and Society
Department of Transdisciplinary Science and Engineering
Tokyo Institute of Technology

March, 2022

Acknowledgments

It is my honour to join the Takada Lab. I am much obliged to my supervisor Professor Jun-ichi Takada for important suggestions, tireless supports, and research guidance. I would like to thank Asst. Prof. Kentaro Saito for kindly advising. I also would like to thank my seniors, Panawit senpai and Nopphon senpai, who help me a lot in my research. Thank you very much.

I am glad to come to Japan, the country that broaden my horizon and let me feel Japanese profound culture in this more than 10 years. It is my honor to get forefront education in Tokyo Instituted of Technology, where I learned a huge knowledge and got so much precious experience for bachelor's degree, master's degree, and doctoral degree.

I would like to thank all Professors in my major department, the Department of Transdisciplinary Science and Engineering, especially Prof. Takahashi, Yamashita, and Akita, who are the examiners for this thesis. I would like also to thank Prof. Aoyagi from the other department, who is also an examiner for this thesis. Not only in study, but they also cared for me in daily life as well.

Especially, I would like to express my gratitude toward ASSURAN International Scholarship Foundation. I have been receiving this scholarship for more than 10 years. Therefore, I could have the motivation and opportunity to bend my mind to studies and enjoy my college life. In the ASSURAN, I met many friends as well. I am also grateful to my dear friends for their comfort, encouragement, and support, when I felt sad or depressed just like a family. Thank you very much.

Finally, I am extremely grateful to my dear parents, whoever took me to this colorful world 29 years ago. You spared no effort to support me grow up in your harvest success.

Xin DU
March' 1 2022

Abstract

Nowadays, millimetre wave bands (mmWaves) has been used for 5G wireless communication system. At mmWaves, attenuation caused by human blockage greatly impact cellphone link performance. An accurate prediction technique of shadowing effect is necessary for understanding the characterization of human blockage and designing future mmWave antennas. Dynamic channel modeling in 5G requires low-computational-cost method for running many frames. Therefore, this research focuses on an accurate and fast prediction method of shadowing effect caused by a 2-dimensional (2D) human-scale object at mmWaves.

Conventionally, full-wave electromagnetic approach, such as method of moment (MoM), has been used to predict the shadowing effect accurately. However, an unreasonable computational cost is a significant drawback for large-scale problems such as a human-size scatterer, especially at mmWave. Therefore, high-frequency asymptotic approximation is expected to reduce the computational complexity. High-frequency asymptotic approximation can be divided into ray-based and source-based approximations. The former, such as uniform theory of diffraction (UTD), is widely used for the reflection and diffraction prediction. UTD has the closed-form analytic solutions resulting in the less computational cost. The latter, such as Kirchhoff approximation (KA), numerically calculate the scattering field. Since KA has good balance between accuracy and computational cost, KA is expected for further development. The drawback of KA is it only considers the single diffraction by modelling the scatterer as a single plane without thickness, which causes prediction error for a thick object. Therefore, the extension of KA for a thick object is needed.

This study aims to develop a 2D mirror Kirchhoff approximation (MKA) for accurately and efficiently predicting the shadowing gain for the thick cylinder. This research proposes the design of the FFT parameters for low calculation time. The applicable range of MKA is extended to the arbitrarily shaped cylinder by multiple planes. This research also proposes the combination of the windowing functions in those multiple planes for better accuracy and lower computational cost.

The concept of MKA for a rectangular cylinder with normal incidence is explained as follows. Two planes expanded by object surfaces facing transmitter (Tx) and receiver (Rx) are used to deal with the double edge diffraction. The fields distributed on the next plane can be obtained by the secondary Huygens ' source generated from the previous plane. The angular spectrum method (ASM) by applying fast Fourier transformation (FFT) is used for a fast calculation speed. The region, where the oscillating integral does not contribute to the final integral, is truncated. For avoiding the discontinuity at truncation boundary, the windowing function based on the Fresnel zone number is chosen. The proposal introduces

the reflection effect between two planes into the double edge diffraction. The proposal is validated for a PEC rectangular cylinder, by comparing with MoM as the reference. The results imply that the proposed method presents a good accuracy.

The design of FFT parameters is proposed for a lower computational cost. Firstly, the discretization in space domain considering the Nyquist sampling criterion for the evanescent wave, which is important for the short distance propagation between two planes, is proposed. Secondly, using Fresnel region approximation in space domain, we find the region far away the edge has a huge discretization error. Therefore, it is better to truncate rather than to numerically integrate the region inaccurately. Then, the spatial windowing size is proposed. Thirdly, using Fresnel region approximation in angular spectrum domain, similar discretization error is observed. The poles in angular spectrum domain, which make a significant contribution for the integral, should be sufficient sampled. That idea proposes the discretization in angular spectrum domain. Fourthly, the truncation size in angular spectrum domain is proposed for better accuracy. With the designed parameters, the computational cost can be extremely lower than before.

The application of MKA is extended for an arbitrarily shaped object. The arbitrarily shaped cylinder is approximated to the combination of several rectangular cylinders. Those rectangular cylinders can be seen as the slices of the arbitrarily shaped cylinder by multiple planes. By applying MKA repeatedly among those planes, the scattered fields can be calculated for the evaluation of the shadowing gain. The new finding is that only the space domain of the zeroth plane and the angular spectrum domain of the last plane need their respective windowing functions, other planes or domains do not. The authors validate the proposed method for an elliptical conductor cylinder with the size of the human body at mmWave. Simulations by changing the object's location, direction, and frequencies are conducted. The results show that the proposed method presents good accuracy with a low root-mean-square error of less than 0.5 dB, compared with the MoM as the reference. Furthermore, the calculation time is improved by 1.4 - 67.2 times compared with the UTD using special functions. The order of computational cost of MKA was $LN \log_2 N$, where N is the FFT size and L is the number of planes.

Finally, the truncation region, interval size, and combination of the windowing functions proposed in this study can achieve an extremely fast speed for calculation within an acceptable accuracy. The extension of the applicable range to the 3-dimensional object is the future topic.

Contents

List of Figures

List of Tables

Chapter 1

Introduction

1.1 Background and Related Works

1.1.1 Necessity of Forward Scattering Prediction

Prediction techniques for the forward scattering problems are widely used such as the forward scattering from the earth's surface in radar study, the forward obstacle searching in the autopilot field, predicting the eclipse in astronomy, and especially the shadowing problem in the fifth generation mobile communication system (5G).

Nowadays, mobile data traffic growth at an accelerated rate can be attributed to the increasing popularity of smartphone. Since sub-6 GHz has become overly saturated, millimetre wave bands (mmWaves), which can provide the additional bandwidth to meet these data traffic demands, has been used for 5G wireless communication system. [1]-[7]

At mmWaves, since free space path loss in the first meter of propagation is increased and diffraction around the obstacle is reduced, the use of Massive multiple input and multiple output (MIMO) to create narrow beams with beamforming technologies (BF) is needed for system operating to maintain an acceptable signal-to-noise radio (SNR) [8]. However, BF with directional antennas will experience the huge shadowing effect caused by humans, furniture, foliage, and cars [9]. Those shadowing effect greatly impact the performance of cellphone link [10]. The phased array antennas of the Massive MIMO have to adapt to find other propagation paths for stable mobile communication [11]. Understanding the characterization of shadowing effect and employing appropriate models for mobile system simulation are important for properly designing future mmWave antennas and beam steering algorithms [12]-[14]. Thus, an accurate prediction technique of shadowing effect is necessary. 5G applies dynamic modelling [15], which requires low-computational-cost method for running many frames. A two-dimension (2D) perfect electric conductor (PEC) cylinder can be approximated to model human body [16]-[18]. Therefore, this research focuses on an accurate and fast prediction method of shadowing effect caused by a 2D human-scale PEC object at mmWaves.

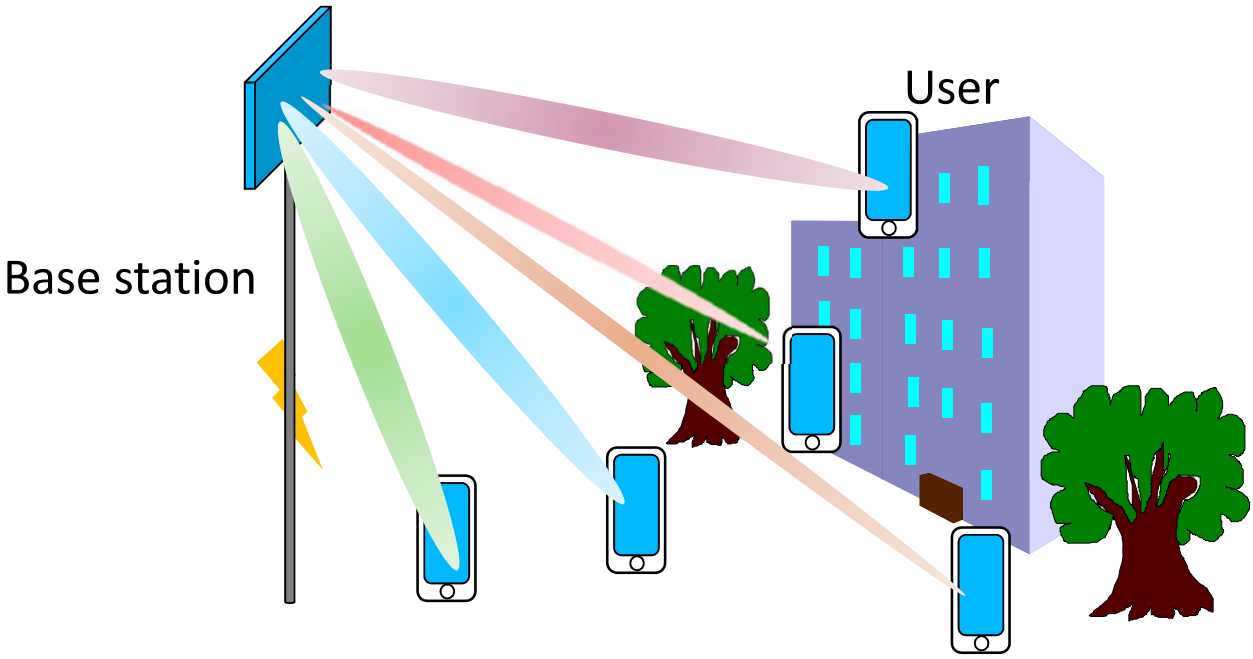

Figure 1.1: Shadowing in 5G

1.1.2 Previous Study

There are mainly two types of prediction techniques, i.e., the empirical model based on measurement and the deterministic model based on theory.

The empirical models (e.g., log normal shadowing [19], Cheung method [20], and Walfisch-Bertoni model [21]), are fast and easy to use, while the results of those methods may need to be calibrated by the experimental data, which is not economical. For an economical prediction, the deterministic models are preferable.

Conventionally, full-wave electromagnetic approaches (e.g., finite-difference time-domain (FDTD) method [22], method of moment (MoM) [23], multilevel fast multipole algorithm (MLFMA) [24], and finite element method (FEM) [25]), have been used to predict the shadowing effect. Those methods solve Maxwell's equations directly, and hence they have good accuracy. However, a high computational cost is a significant drawback for large-scale problems such as a human-size scatterer, especially at mmWave. Therefore, another branch of deterministic model, namely high-frequency asymptotic approximation, is expected to reduce the computational complexity. High-frequency asymptotic approximation can be divided into ray-based and source-based methods.

Ray-based methods including geometrical optics approximation (GO) [26], geometrical theory of diffraction (GTD) [27], and uniform theory of diffraction (UTD) [28] consider electromagnetic fields as rays. The methods based on Fermat's principle have the closed-form analytic solutions, resulting in a lower computational cost. GO describes the propagation phenomena including the incidence, reflection, and refraction, but not the diffraction. GTD introduces diffraction around edges and smooth objects, while its coefficients are divergent

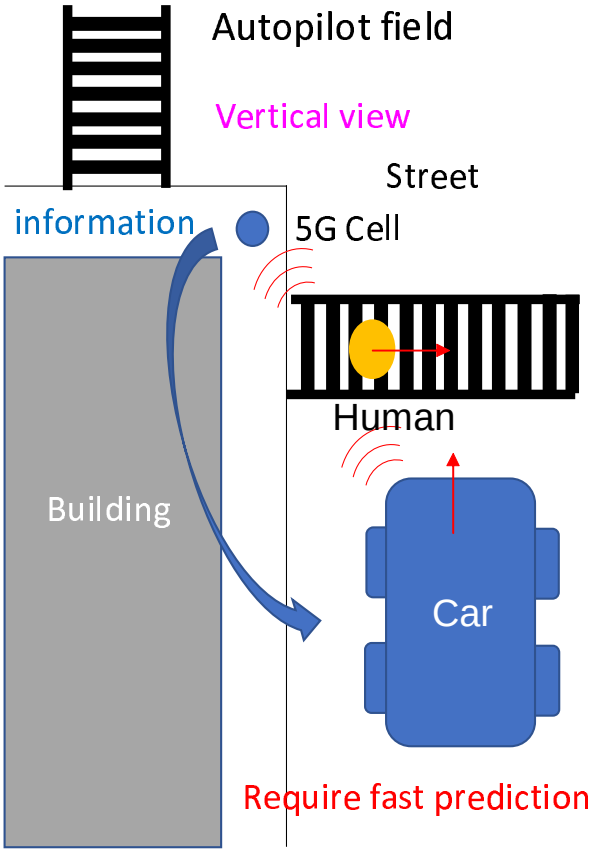

Figure 1.2: Autopilot field

at the shadowing boundary. Its extension UTD uses the Fresnel integral to overcome the discontinuity of GTD near the shadowing boundary [29]-[42]. However, when UTD calculates a creeping wave diffraction [43] from an elliptical cylinder, not only the Fresnel integral but also the ellipse integral needs the additional calculation time. Furthermore, for a complex shaped object, since the reflection point of the curved surface cannot be easily found by the imaging method, reflection point searching requires plenty of time in ray-based method.

Source-based methods, such as physical optics approximation (PO) [44] and Kirchhoff approximation (KA) [45]-[50], consider electromagnetic fields as the equivalent sources. The methods based on Huygens' principle numerically calculate the scattered field for a complex shaped region and hence they have a good balance between accuracy and computational complexity. In PO calculation, the scattered field is calculated from the shadowing object, and can be split into the reflection radiation to the specular direction and the shadow radiation to the forward direction [51]. For the forward scattering problem, the contribution is mainly determined by the shadow radiation. However, since the shadow radiation is calculated by the integration over the cross-section of the geometrical shadow region [44], PO has the difficulty to evaluate the influence of the thickness for the forward scattering problem. In KA calculation, the scattered field is calculated from the vacuum region around the shadowing object, and hence KA is more suitable for the forward scattering problem. Although KA is the numerical approach, which may be slower than the analytic approach, it is still

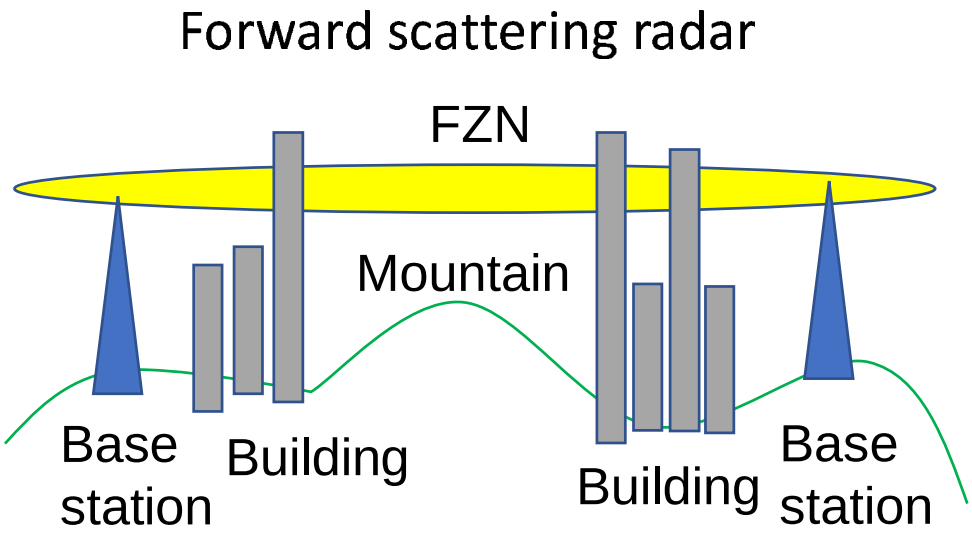

Figure 1.3: Forward radar study

extremely fast due to the lower computational complexity of the angular spectrum method (ASM) [52]-[73]. ASM uses fast Fourier transform (FFT) to transfer the field between the space and angular spectrum domains. The drawback of KA is that KA only considers the single diffraction by modelling the scatterer as a screen without thickness, which causes prediction error for a thick object [74]-[77]. Therefore, the extension of KA for a thick object is needed. In addition, a small FFT size is expected to reduce the computational cost.

The hybrid methods by introducing GTD creeping wave into PO such as physical theory of diffraction (PTD) [78]-[98] can predict the forward scattering problem preferably. Although PTD combines the advantages of PO and GTD to deal with the forward scattering problem for a thick object, both special functions and numerical integral require substantial computational costs. Knife-edge diffraction method (KEDM) [99], [100] and its extension Bullington method [101] analytically calculate KA scattered field in a closed form for reducing the computational cost. However, similar to KA, those methods only consider the scatterer as a screen. Therefore, the accuracy for a thick object is a significant issue.

This study aims to develop a fast and accurate method based on KA to predict the shadowing gain for the thick cylinder. The reasons for selecting KA as the foundation are explained as follows. Firstly, KA is more suitable for the forward scattering problem [47] comparing with PO and hence it is expected to deal with the prediction of shadowing. Secondly, since the scattered field is obtained by integration over the lit region of the scattering surface in the source-based calculation [47], KA can partially consider the geometrical shape of the shadowing object, unlike KEDM, GO, GTD, and UTD. Thirdly, KA applying FFT is extremely fast as opposed to FDTD, MoM, FEM, and PTD. These advantages show that KA is a reasonable choice for further development.

The applicable range of KA is extended to a thick cylinder by multiple planes. Although

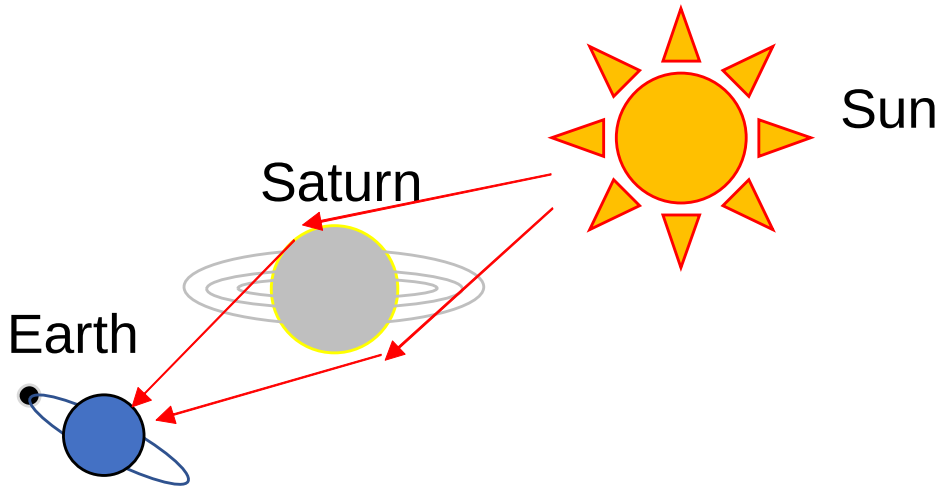

Figure 1.4: Eclipse in astronomy

the formulation processes are quite different, the idea of multiple planes is mathematically the same as the wide-angle split-step parabolic equation (SSPE) [102] and beam propagation method (BPM) [103]. In SSPE and BPM calculation, they widely discuss Tukey and Hanning windows for the forward scattering problems [104]-[108], while they need a large truncation region resulting in high computational cost. On the other hand, in PO calculation, the windowing function based on the Fresnel zone number (FZN) [109]-[114] can achieve a small truncation region within an acceptable accuracy, while those works only consider the backward scattering problems. Moreover, none of the above works have designed the windowing function and interval in the angular spectrum domain. Those factors affect the computational cost and accuracy, and hence lack of the designed parameters of FFT is a common issue for all the FFT-based methods. The truncation region, resolution size, and the combination of the windowing functions proposed in this study are not discussed in those methods [115]-[141]. Those proposals can achieve an extremely fast speed for calculation within an acceptable accuracy. Therefore, the proposals can be also applicable for SSPE and BPM.

1.2 Motivations

Motivation 1: conventional KA is inaccurate for a thick object.

Motivation 2: conventional numerical methods have high computational cost comparing with the analytical methods.

1.3 Research Objectives

Objective 1: the goal of this study is to develop a 2D mirror Kirchhoff approximation (MKA) for accurately predicting the shadowing gain caused by a thick cylinder.

Objective 2: this study extends Objective 1 within a low computational cost, which shall achieve a faster speed compared with UTD, by proposing the design of FFT parameters and the combination of the windowing functions.

1.4 Importance of This Research

This research can provide a fast and accurate forward scattering prediction method of a thick object EM simulation. Not only EM wave, but also other strong-wave forward scattering problems can apply this method. It also contributes to other academic or industry field.

The applicable range of KA is extended to a thick object by MKA. This study proposes the design of the truncation region and resolution of FFT. In the space domain, the windowing function based on FZN is extended to the forward scattering problem. In the angular spectrum domain, a rectangular windowing function is proposed to use for accuracy and computational cost. The paper also proposes a combination of windowing functions in multiple planes for better accuracy and lower calculation time. The truncation region, resolution and combination of the windowing functions proposed in this study can also be applicable to SSPE and BPM for a fast calculation with an acceptable accuracy.

1.5 Thesis Structure

Thesis structure is explained as follows.

Chapter 2 will introduce current predicting methods including MoM, UTD, and KA. The detailed formulations will be provided. The calculation approaches for the desired field will be explained. The issues of the respective methods will be discussed.

Chapter 3 will introduce the concept of MKA. Detailed formulations will be provided and explained. Simulations for validated the MKA will be conducted for a rectangular cylinder. The results of accuracy will be compared with MoM.

Chapter 4 will propose the design of the simulation parameters for MKA. Detailed formulations will be provided and explained.

Chapter 5 will extend the applicable range of MKA to an arbitrarily shaped cylinder by multiple planes. The combination of windowing functions for accuracy and computational cost will be proposed. Simulations for validated the proposal will be conducted for an elliptical cylinder. The results will be compared with MoM and UTD in terms of the accuracy and computational cost. Evaluations and discussions will be done by varying the simulation parameters. The limitations and the future applicabilities will be discussed.

Chapter 6 will discuss the conclusion, the contributions, and the future work.

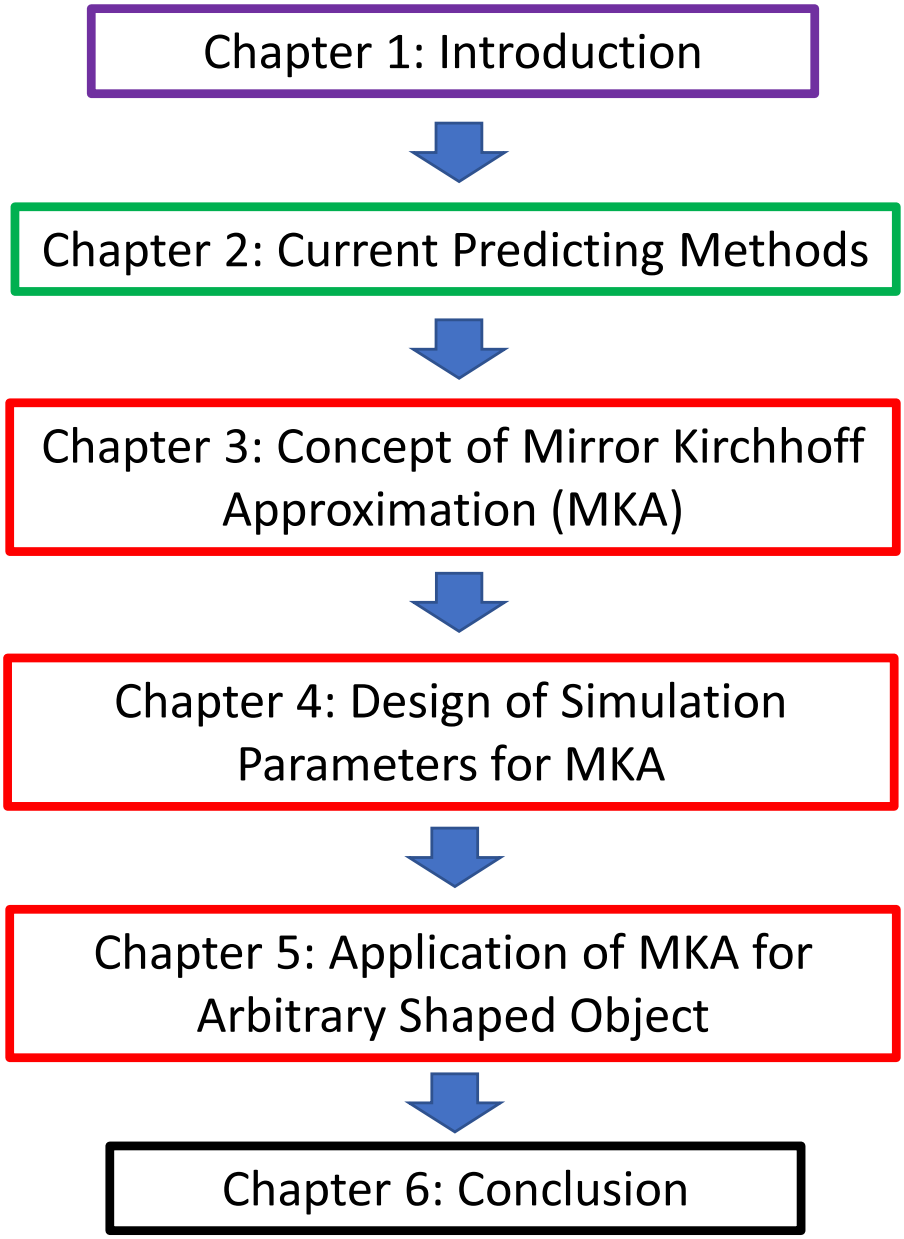

Figure 1.5: Thesis structure

Chapter 2

Current Predicting Methods

2.1 Introduction

In this chapter, three methods used in this study will be introduced. There are full-wave MoM for the reference of accuracy, analytic-approximation UTD for the reference of calculation time, and numerical-approximation KA for the further development.

A scenario, where a PEC shadowing object is put between transmitter (Tx) and receiver (Rx), is considered. In perpendicular polarization, only y-component of electric field works, and hence the vector equations can be simplified to scalar equations. Assuming the problem is uniform along y-axis, the 3D problem can be simplified to the 2D problem as shown in Fig. 2.1.

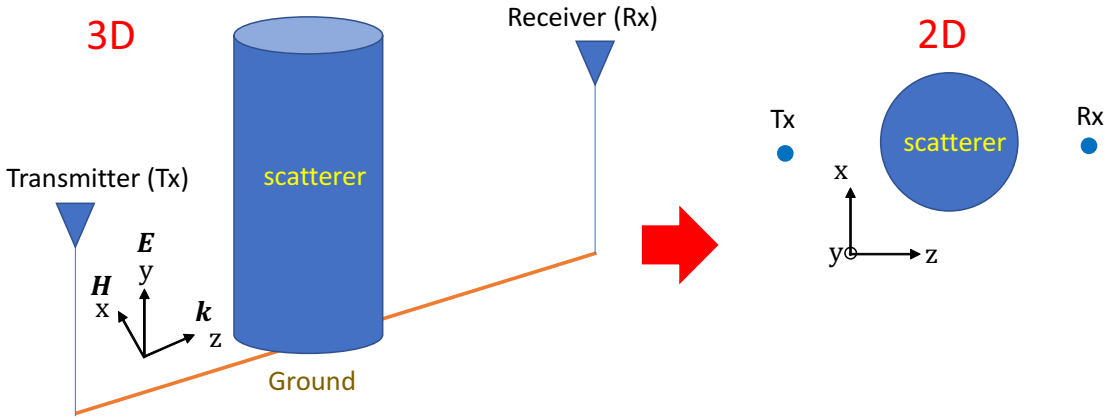

Figure 2.1: 2D problem

where, $\boldsymbol{E}$ is the electric field (later call it field). $\boldsymbol{H}$ is the magnetic field. $\boldsymbol{k}$ is the wave vector.

2.2 Method of Moment (MoM)

Method of moment (MoM) uses integration equation to calculate electromagnetic fields in the frequency domain. The Green's theory derives the 2D electrical field integral equation (EFIE) for exterior region in perpendicular polarization as

$$\frac{1}{2}E = E^{\text{inc}} - \frac{\text{j}}{4}\int_C \left(E\frac{\partial H_0^{(2)}(k_0\rho)}{\partial n} - \frac{\partial E}{\partial n}H_0^{(2)}(k_0\rho) \right) \text{d}l \tag{2.1}$$

where E is the unknown total field at the observation point. E^{inc} is the incident field. $\boldsymbol{n}$ is outward normal vector of object. k_0 is the wave number in free space. $H_0^{(2)}(\cdot)$ represents the second kind of Hankel function for 0 order. ρ is the distance from the source point to the observation point.

By applying EFIE for a PEC object, which has the boundary condition of $E = 0$, we have

$$E^{\text{inc}} = -\frac{\text{j}}{4}\int_C H_0^{(2)}(k_0\rho)J\text{d}l \tag{2.2}$$

$$J = \frac{\partial E}{\partial n} \tag{2.3}$$

where J is the unknown inductive current.

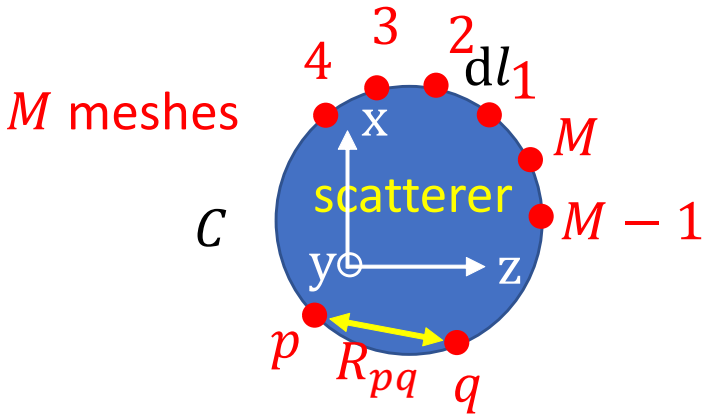

Figure 2.2: Method of moment

Suppose that the surface of object is sampled by M meshes as shown in Fig. 2.2. By applying the piecewise constant as basis functions and using point matching method, we can have the matrix form as

$$\begin{pmatrix} a_{11} & \cdots & a_{1q} & \cdots & a_{1M} \\ \vdots & \ddots & & & \vdots \\ a_{p1} & & a_{pq} & & a_{pM} \\ \vdots & & & \ddots & \vdots \\ a_{M1} & \cdots & a_{Mq} & \cdots & a_{MM} \end{pmatrix} \begin{pmatrix} J_1 \\ \vdots \\ J_p \\ \vdots \\ J_M \end{pmatrix} = \begin{pmatrix} E_1^{\text{inc}} \\ \vdots \\ E_p^{\text{inc}} \\ \vdots \\ E_M^{\text{inc}} \end{pmatrix} \tag{2.4}$$

$$a_{pq} = -\frac{\mathrm{j}}{4}\int_{\Delta C_q} H_0^{(2)}(k_0\rho_{pq})\mathrm{d}l \tag{2.5}$$

where, J_p and E_p^{inc} are the inductive current and incident field at mesh p, respectively. ρ_{pq} is the distance between meshes p and q.

Note that, if ρ_{pq} is zero ($p = q$), $H_0^{(2)}(k_0\rho_{pq})$ will become a singularity, which cannot be solved by the numerical approach. An analytic approach is used as

$$a_{pp} \approx -\frac{\mathrm{d}l}{2\pi}\left(\ln\frac{k_0\mathrm{d}l}{4} + \mathrm{j}\frac{\pi}{2} + \gamma_0 - 1\right) \tag{2.6}$$

where γ_0 is the Euler constant.

By solving the matrix, we can obtain the unknown inductive current. Then, the scattered field can be calculated by radiation integration as

$$E^{\mathrm{scat}} = \frac{\mathrm{j}}{4}\int_C H_0^{(2)}(k_0\rho^{\mathrm{scat}})J\mathrm{d}l \tag{2.7}$$

where E^{scat} is the scattered field. ρ^{scat} is the distance between each mesh at object to Rx.

Finally, the desired field is calculated by the summation of incident field and scattered field. The issue of MoM is the high computational cost. At mmWaves, the M becomes larger causing the increase of size of matrix. Since the order to solve this matrix is M^3, the high computational cost is needed.

2.3 Geometrical Optics (GO), Geometrical Theory of Diffraction (GTD), and Uniform Theory of Diffraction (UTD)

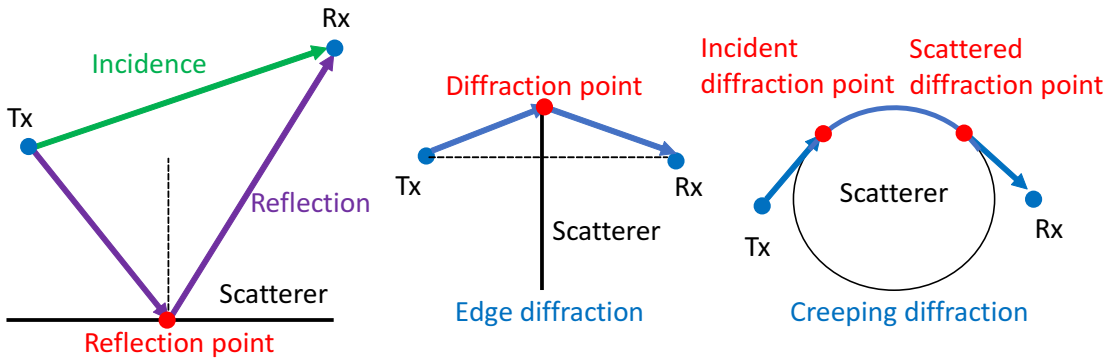

Figure 2.3: Propagation phenomena

Geometrical optics (GO), geometrical theory of diffraction (GTD), and uniform theory of diffraction (UTD) approximate electromagnetic fields as rays. GO can deal with the propagation phenomena include incidence and reflection. GTD introduces the diffraction into GO, which is important for the forward scattering problem. The types of diffraction phenomena are introduced, i.e., edge diffraction which is diffraction from edge, and creeping wave diffraction which is diffraction from the curved surface. However, GTD coefficient is divergent at SB causing error issue. Its extension, UTD, solves the accuracy issue of GTD by introducing Fresnel integral. Since those methods analytically calculate desired fields in a closed form, it has a low computational cost.

A 2D PEC elliptical cylinder is considered as the cross section of human body. Then, the creeping diffraction and specular reflection waves dominate the desired fields. Due to accuracy issue of GO and GTD, UTD is chosen for the further comparison. The UTD coefficients can be calculated as follows.

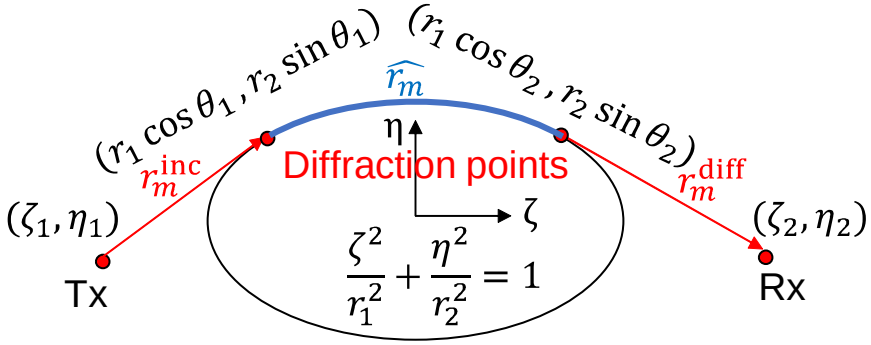

(a) Model of creeping wave diffraction.

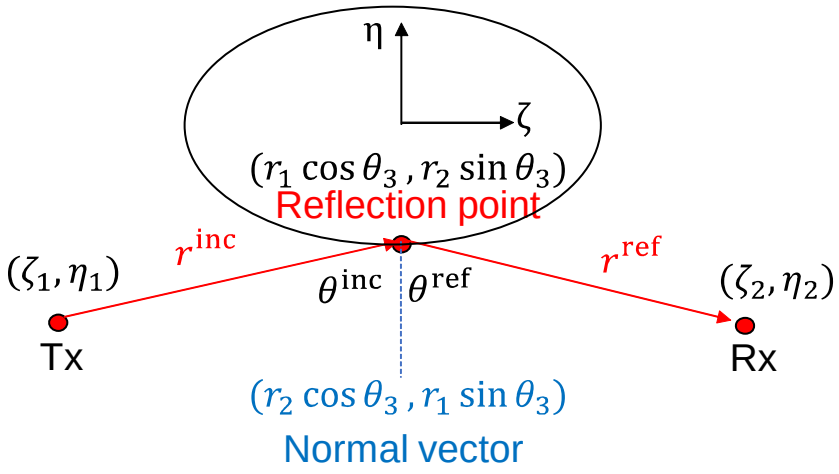

(b) Model of specular reflection.

Figure 2.4: Rotation conversion to a standard ellipse in ζ-η domain.

For the convenience, the rotation matrix translates the arbitrary rotated ellipse to a standard ellipse in ζ-η domain with the origin at the center of the ellipse as shown in Fig. 2.4.

Considering one creeping diffraction ray in Fig. 2.4(a), the authors find the incident and scattered diffraction points $(r_1\cos\theta_{1,2}, r_2\sin\theta_{1,2})$ by (2.8).

$$\theta_{1,2} = \arcsin\frac{1}{\sqrt{\frac{\zeta_{1,2}^2}{r_1^2}+\frac{\eta_{1,2}^2}{r_2^2}}} - \arctan\frac{\zeta_{1,2}r_2}{\eta_{1,2}r_1} \tag{2.8}$$

where r_1 and r_2 are the semi-major and semi-minor axes of the ellipse. (ζ_1, η_1) and (ζ_2, η_2) are the coordinates of Tx and Rx, respectively. θ_1 and θ_2 are the parameters of the incident and scattered diffraction points, respectively.

The curve length between the incident and scattered diffraction points is calculated by (2.9).

$$\widehat{r_m} = r_2\left(\mathrm{E}(\theta_2|1-\frac{r_1^2}{r_2^2}) - \mathrm{E}(\theta_1|1-\frac{r_1^2}{r_2^2})\right) \tag{2.9}$$

where $\widehat{r_m}$ is the curve length. $\mathrm{E}(\cdot)$ is the incomplete elliptic integral of the second kind.

The curvature radius $\rho_{1,2}$ at two diffraction points is calculated by (2.10).

$$\rho_{1,2} = \frac{\sqrt{(r_1^4 r_2^2\sin^2\theta_{1,2} + r_1^2 r_2^4\cos^2\theta_{1,2})^3}}{r_1^4 r_2^4} \tag{2.10}$$

The parameters of the creeping diffraction wave are calculated by (2.11)–(2.14).

$$M_{1,2} = \left(\frac{k_0\rho_{1,2}}{2}\right)^{\frac{1}{3}} \tag{2.11}$$

$$L_m = \frac{r_m^{\mathrm{inc}} r_m^{\mathrm{diff}}}{r_m^{\mathrm{inc}} + r_m^{\mathrm{diff}}} \tag{2.12}$$

$$\xi^d = \left(\frac{k_0}{2}\right)^{\frac{1}{3}} \frac{(r_1 r_2)^{\frac{2}{3}}}{r_2}\left(\mathrm{K}(\theta_2|1-\frac{r_1^2}{r_2^2}) - \mathrm{K}(\theta_1|1-\frac{r_1^2}{r_2^2})\right) \tag{2.13}$$

$$X^d = \frac{k_0 L_m (\xi^d)^2}{2M_1 M_2} \tag{2.14}$$

where r_m^{inc} is the distance between Tx and the incident diffraction point. r_m^{diff} is the distance between Rx and the scattered diffraction point. $\mathrm{K}(\cdot)$ is the incomplete elliptic integral of the first kind. $M_{1,2}, L_m, \xi^d, X^d$ are the UTD parameters mentioned in [43].

Finally, (2.15) gives the formula for the diffraction coefficient, which calculates the diffraction field.

$$D = -\sqrt{M_1 M_2}e^{-\mathrm{j}k_0\widehat{r_m}}\sqrt{\frac{2}{k_0}}\{\frac{e^{-\mathrm{j}\frac{\pi}{4}}}{2\sqrt{\pi}\xi^d}[1-F(X^d)] + \hat{P}(\xi^d)\} \tag{2.15}$$

where $F(\cdot)$ is the modified Fresnel integral. $\hat{P}(\cdot)$ is the Pekeris' caret function, which is approximated by (2.16).

$$\hat{P}(\xi) \approx \begin{cases} -\frac{e^{-\mathrm{j}\frac{\pi}{4}}}{\sqrt{\pi}} \sum_{p=1}^{\infty} \frac{e^{\mathrm{j}\frac{\pi}{6}} e^{\xi \alpha_p e^{-\mathrm{j}\frac{5}{6}\pi}}}{2(\mathrm{Ai}'(\alpha_p))^2} & (\xi > 2) \\ \left(p^*(\xi) - \frac{1}{2\sqrt{\pi}\xi}\right) e^{-\mathrm{j}\frac{\pi}{4}} & (-3 \le \xi \le 2) \\ \sqrt{\frac{-\xi^3}{4}} e^{\mathrm{j}\frac{\xi^3}{12}} & (\xi < -3) \end{cases} \tag{2.16}$$

where $\mathrm{Ai}(\cdot)$ is the Airy function and its p^{th} root is α_p. The complex conjugate of $p^*(\cdot)$ is given in [147].

For the specular reflection ray in Fig. 2.4(b), the reflection point cannot be found analytically. The authors find it numerically as follows. Since the normal vector at the reflection point $(r_1 \cos\theta_3, r_2 \sin\theta_3)$ is $(r_2 \cos\theta_3, r_1 \sin\theta_3)$, in the complex domain, the law of reflection $\theta^{\mathrm{inc}} = \theta^{\mathrm{ref}}$ is equivalent to (2.17).

$$z_1 = (\zeta_1 - r_1 \cos\theta_3) + \mathrm{j}(\eta_1 - r_2 \sin\theta_3) \tag{2.17a}$$
$$z_2 = r_2 \cos\theta_3 + \mathrm{j} r_1 \sin\theta_3 \tag{2.17b}$$
$$z_3 = (\zeta_2 - r_1 \cos\theta_3) + \mathrm{j}(\eta_2 - r_2 \sin\theta_3) \tag{2.17c}$$
$$\arg(\frac{z_3}{z_2}) = \arg(\frac{z_2}{z_1}) \tag{2.17d}$$

where z_1 is the complex number corresponding to the vector pointing from the reflection point to Tx. z_2 is the complex number corresponding to the normal vector at the reflection point. z_3 is the complex number corresponding to the vector pointing from the reflection point to Rx. θ_3 is the parameter of the reflection point. The authors numerically solve the equation (2.17) to search θ_3 by MATLAB vpasolve.

The parameters of the reflection wave are calculated by (2.18)–(2.21).

$$\rho_3 = \frac{\sqrt{(r_1^4 r_2^2 \sin^2\theta_3 + r_1^2 r_2^4 \cos^2\theta_3)^3}}{r_1^4 r_2^4} \tag{2.18}$$
$$M_3 = \left(\frac{k_0 \rho_3}{2}\right)^{\frac{1}{3}} \tag{2.19}$$
$$\xi^r = -2M_3 \cos\theta^{\mathrm{inc}} \tag{2.20}$$
$$X^r = \frac{2k_0 r^{\mathrm{inc}} r^{\mathrm{ref}} \cos^2\theta^{\mathrm{inc}}}{r^{\mathrm{inc}} + r^{\mathrm{ref}}} \tag{2.21}$$

where r^{inc} is the distance between Tx and the reflection point. r^{ref} is the distance between Rx and the reflection point. ρ_3 is the curvature radio at the reflection point. M_3, ξ^r, X^r are the UTD parameters mentioned in [43]. θ^{inc} is the incident angle.

Finally, (2.22) gives the formula for the reflection coefficient, which calculates the reflection field.

$$R = -\sqrt{\frac{-4}{\xi^r}} e^{-\mathrm{j}\frac{(\xi^r)^3}{12}} \{ \frac{e^{-\mathrm{j}\frac{\pi}{4}}}{2\sqrt{\pi}\xi^r} [1 - F(X^r)] + \hat{P}(\xi^r) \} \tag{2.22}$$

Finally, the desired field is calculated by the summation of incident field, reflection field, and diffraction field. The calculation of UTD is also in a closed form like GTD. However, UTD uses Fresnel and ellipse integrals. Those special functions need additional computational cost.

2.4 Physical Optics (PO) and Kirchhoff Approximation (KA)

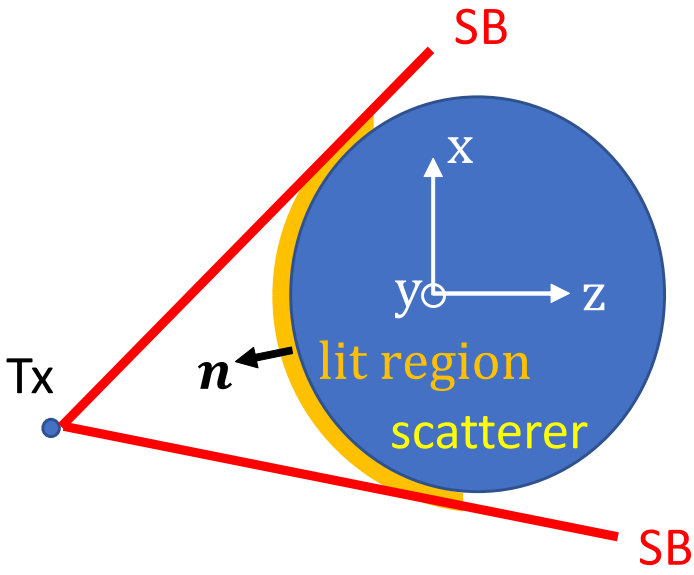

Figure 2.5: Physical Optics

Physical optics (PO) and Kirchhoff approximation (KA) approximate electromagnetic fields as waves generated on PEC and vacuum planes, respectively, based on the Huygens 窶 摺 resnel principle. PO approximates scatter as infinite tangential PEC plane. In PO, the inductive current are only generated on the illuminated side of object as shown in Fig. 2.5. The inductive current is approximated as

$$J \approx \begin{cases} 2\dfrac{\partial E^{\mathrm{inc}}}{\partial n} & \text{(for lit region)} \\ 0 & \text{(for shadowed region)} \end{cases} \tag{2.23}$$

Same as MoM, the desired field can be calculated by radiation integration. PO is suitable for the backward scattering problem as shown in Fig. 2.6. However, shadowing problem is a forward scattering problem.

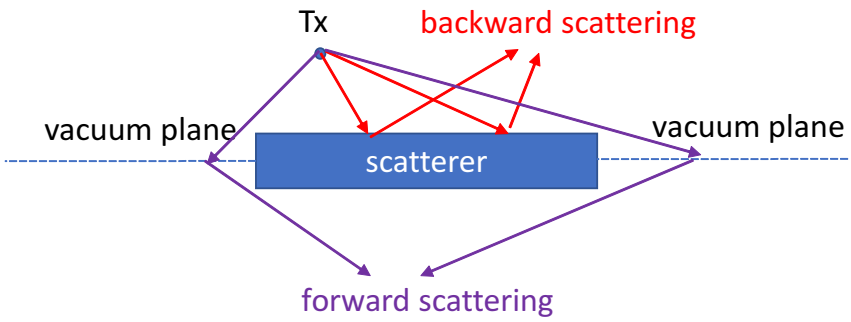

Figure 2.6: Forward and backward scattering problems

KA is more suitable for the forward scattering problem. Total field at vacuum plane is approximated as incident field only.

$$E \approx \begin{cases} E^{\text{inc}} & \text{(for vacuum plane)} \\ 0 & \text{(for shadowing object)} \end{cases} \tag{2.24}$$

The desired field can be calculated by radiation integration or angular spectrum method (ASM) [52, 142]. However, KA can only deal with the single diffraction problem as shown in Fig. 2.7.

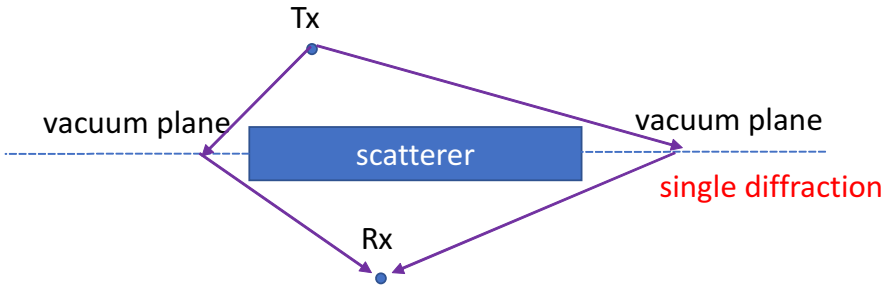

Figure 2.7: Kirchhoff Approximation

The extension of KA for the multiple diffraction problem is needed. The computational cost of KA is higher than analytical approach like UTD, while it is lower than full-wave MoM. Therefore, KA has good balance between the accuracy and computational cost.

2.5 Connection of Each Method

The connection of Section 2.4 and Section 2.2 is described as follows. Both Section 2.4 and Section 2.2 are the numerical methods based on boundary element. However, Section 2.4 uses approximation for the unknown variables at boundary while Section 2.2 solves those variables by using implicit method. Therefore, Section 2.2 has the better accuracy while Section 2.2 has the lower computational cost comparing with each other.

The connection of Section 2.3 and Section 2.4 is described as follows. Section 2.4 calculates the desired field by radiation integration, where the regions far away from the stationary phase points and edges do not contribute to the final integral due to the cancellation of rapidly oscillating function. The stationary phase point caused by peak of field or discontinuity at edge are corresponding to the reflection or diffraction point in Section 2.3. Thus, we can simply say that Section 2.4 numerically calculates integration over the boundary while Section 2.3 analytically calculates the field at the stationary phase point and edge.

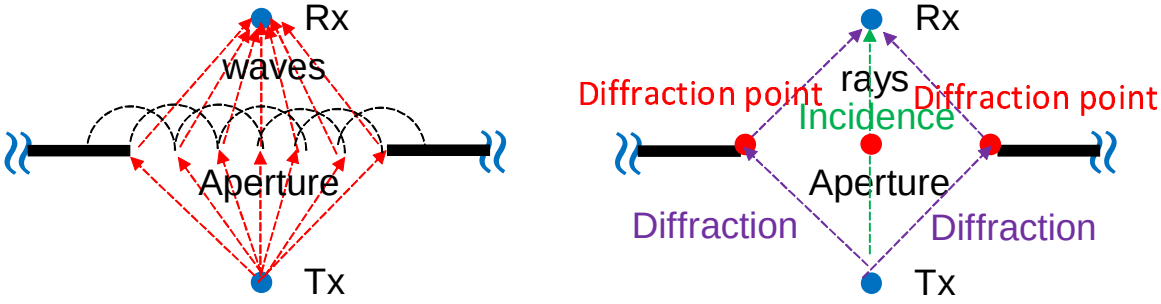

Figure 2.8: Source-based and ray-based methods

2.6 Conclusion

In this Chapter, the methodologies used in the this research were introduced. The detailed formulations of each method were provided. The calculation approaches for the desired field were explained. The issues of the respective methods were discussed. The connections of each method were described.

Chapter 3

Concept of Mirror Kirchhoff Approximation (MKA)

3.1 Introduction

This chapter will propose an accurate scattered field prediction method based on Kirchhoff Approximation called 'Mirror Kirchhoff Approximation' (MKA) for evaluating the shadowing effect. The idea and detailed formulations of the proposal will be presented. The proposed method will be validated for a PEC rectangular cylinder, by comparing with MoM as a reference.

3.2 Idea of MKA

The model of the proposal shown in Fig. 3.1 explains the idea in an easily understood manner. A rectangular cylinder is considered as the shadowing object. Tx and Rx face the front and back surfaces of the rectangular, respectively. The infinite large planes expanded from the front and back surface of the rectangular cylinder are defined as the zeroth and first planes, respectively. Additionally, the infinite plane through Rx and paralleling to the first plane is defined as the second plane.

MKA uses those multiple planes to calculate the multiple diffraction. The total electric fields distributed on the zeroth plane can be approximated by KA. Then, the fields distributed on the first plane can be obtained by the secondary Huygens' sources generated from the zeroth plane. Repeating the approach in the same manner, the fields distributed on the second plane including Rx can be calculated as well. Finally, the shadowing effect can be evaluated by comparing receiving electric field at Rx and in free space.

In MKA calculation, the propagation wave between the two planes is not only outstretched, and but also includes reflection effect from the shadowing object. Since the introduction of reflection uses mirror image theory as shown in Fig. 3.2, this method is named 'Mirror Kirchhoff Approximation'.

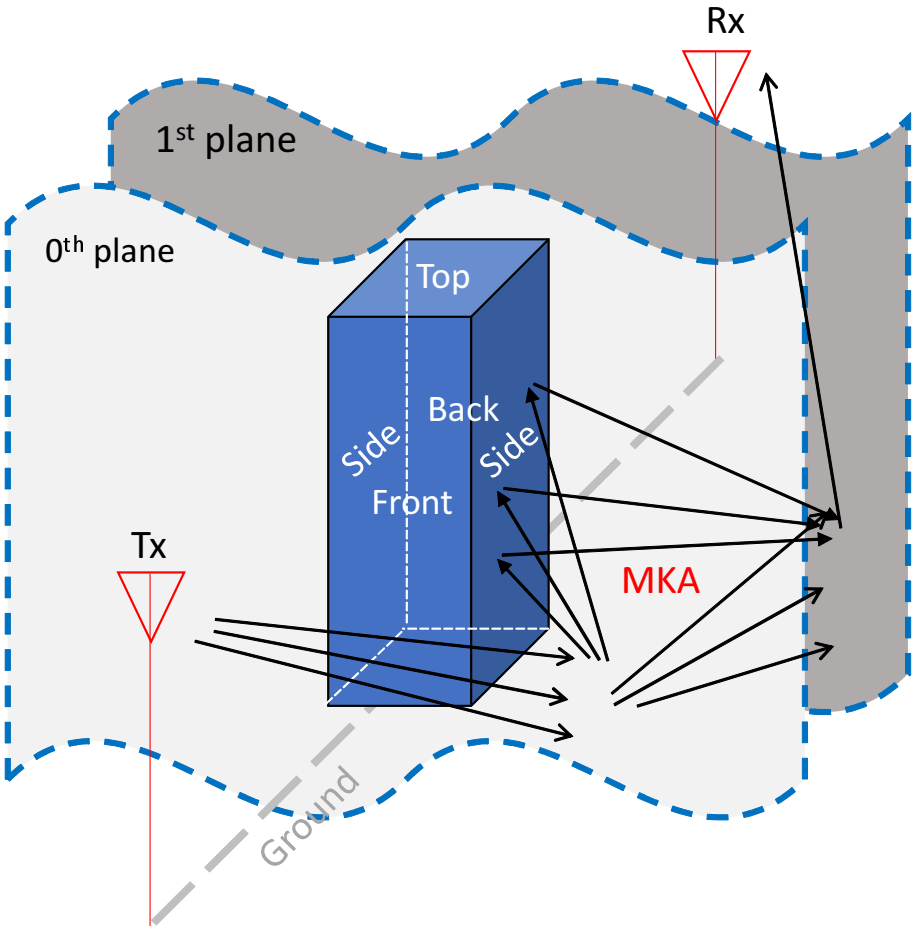

Figure 3.1: Model of MKA

3.3 Formulations of MKA for A Rectangular Cylinder

The fields distributed on the region of interest can be determined by using the surface current. However, the complexity of the surface current determined by both the points of source plane and the points of the observation plane is too large when the region of interest is large. It is more efficient to use the angular spectrum method (ASM) [52, 142] by applying FFT since the complexity of computation can be reduced from $O(N^2)$ to $O(N \log_2 N)$, where N is FFT size.

2D problem is considered by assuming the problem is uniform along y-axis in a Cartesian coordinates system. The LoS path is defined as z-axis. Figure 3.3 shows that ASM calculates the propagation between two parallel planes $z = ld$ and $z = (l + 1)d$ as

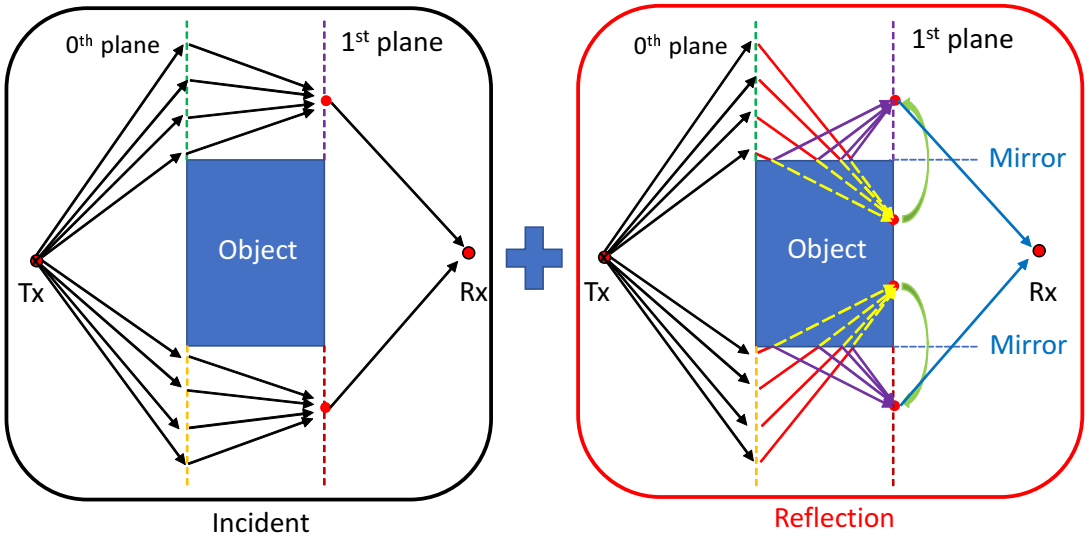

Figure 3.2: 2D Model of proposal

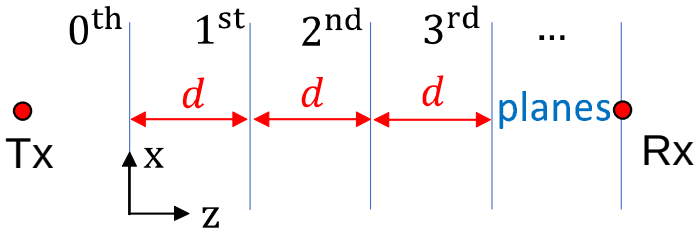

Figure 3.3: Model of angular spectrum method.

$$\tilde{E}_{l,i}(k_{\mathrm{x}}) = \int_{-\infty}^{\infty} E_{l,i}(x) e^{\mathrm{j}k_{\mathrm{x}}x} \mathrm{d}x \tag{3.1}$$

$$E_{l+1,i}(x) = \frac{1}{2\pi} \int_{-\infty}^{\infty} \tilde{E}_{l,i}(k_{\mathrm{x}}) e^{-\mathrm{j}k_{\mathrm{x}}x} e^{-\mathrm{j}k_{\mathrm{z}}d} \mathrm{d}k_{\mathrm{x}} \tag{3.2}$$

$$k_{\mathrm{z}} = \begin{cases} +\sqrt{k_0^2 - k_{\mathrm{x}}^2} & (|k_{\mathrm{x}}| \leq k_0) \\ -\mathrm{j}\sqrt{k_{\mathrm{x}}^2 - k_0^2} & (|k_{\mathrm{x}}| > k_0) \end{cases} \tag{3.3}$$

where x is the parameter of the x-space domain. k_{x} and k_{z} are the parameters of the angular spectrum domain corresponding to the x-space and z-space domain, respectively. $E_{l,i}(\cdot)$ is the total fields in the l^{th} plane $z = ld$ $(l = 0, 1, ..., L)$ for region i $(i = 1, 2)$. Regions 1 and 2 are the vacuum regions above and below the shadowing object, respectively. $\tilde{E}_{l,i}(\cdot)$ is the IFT of $E_{l,i}$. d is the distance between two planes. The cases of $|k_{\mathrm{x}}| \leq k_0$ and $|k_{\mathrm{x}}| > k_0$ in (3.3) represent the propagation and evanescent waves, respectively. Usually, the calculation ignores the evanescent wave $(|k_{\mathrm{x}}| > k_0)$ when d is large. That is because the complex exponential factor $e^{-\mathrm{j}k_{\mathrm{z}}d}$ becomes the decay exponential factor $e^{-\sqrt{k_{\mathrm{x}}^2 - k_0^2}d}$ and vanishes when d is large. It is known as the evanescent wave where the energy is not transferred but decays exponentially.

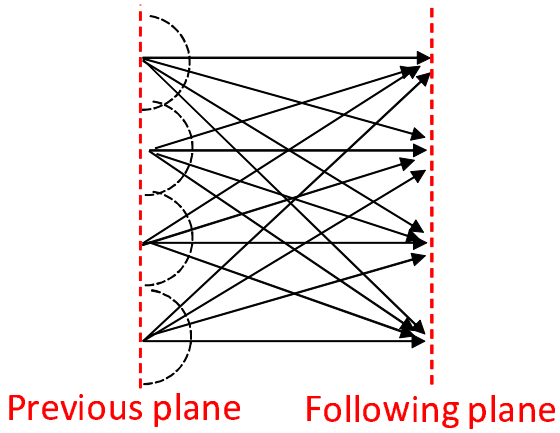

Figure 3.4: Integral of surface current by cylindrical-wave propagation

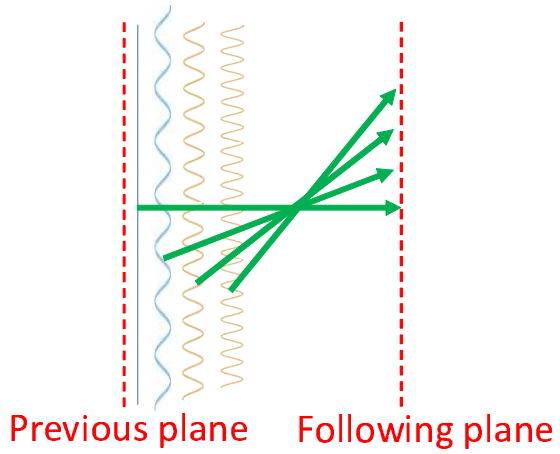

Figure 3.5: ASM by plane-wave propagation

To apply FFT, discretization for the numerical calculation and truncation for the integral over the finite interval are needed in the space and angular spectrum domains. Suppose the range of FFT in x-space domain is X and the spatial sampling interval is Δx, the intervals of the space and angular spectrum domains are Δx and $2\pi/X$, respectively. FFT size N is determined by $X/\Delta x$.

Figure 3.6 shows the model of environment. An object shadows the line-of-sight (LoS) path between a Tx and a Rx. The distances from the zeroth plane to Tx and Rx are b and c, respectively. The equations of the zeroth, first, and second planes are $z = 0$, $z = d$, and $z = c$, respectively. The coordinate of the i^{th} edge in the l^{th} plane is $w_{l,i}$. The spatial and angular spectrum parameters x and k_{x} can be discretized by (3.4) and (3.5), where u, p are the discrete indexes of x and k_{x}, respectively.

$$x = u\Delta x \quad (u = 1 - \frac{N}{2}, -\frac{N}{2}, ..., -1, 0, 1, ..., \frac{N}{2}) \tag{3.4}$$

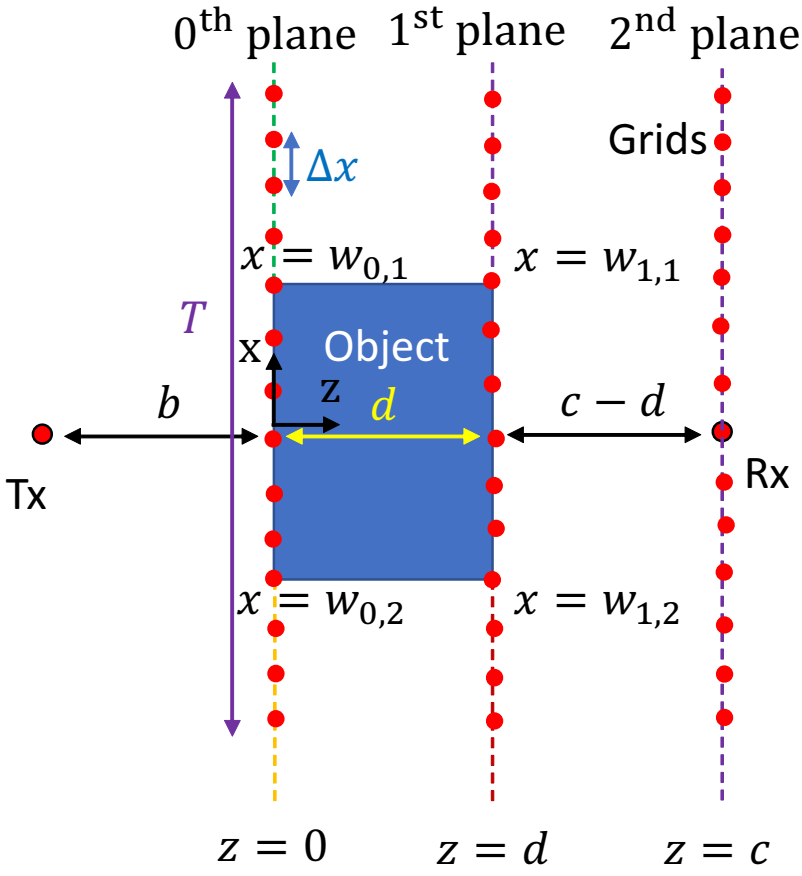

Figure 3.6: Image of discretization

$$k_{\mathrm{x}} = p\frac{2\pi}{X} \quad (p = 1 - \frac{N}{2}, -\frac{N}{2}, ..., -1, 0, 1, ..., \frac{N}{2}) \tag{3.5}$$

Truncation for the integral over the finite interval is needed. The region, where the integral of the rapidly oscillating field distributed on planes does not contribute to the final integral due to the cancellation, can be truncated. For avoiding the discontinuity at boundary, which causes addtional diffraction error, the windowing function [109]-[114] based on the Fresnel zone number is chosen as

$$W_{l,i}^{\mathrm{Sp}}(x) = \begin{cases} \frac{1}{2}(\cos(\frac{n(x) - n(w_{l,i})}{n(a_{l,i}) - n(w_{l,i})}\pi) + 1) & (|x - w_{l,i}| \leq a_{l,i}) \\ 0 & (|x - w_{l,i}| > a_{l,i}) \end{cases} \tag{3.6}$$

$$n(x) = \frac{\sqrt{x^2 + b^2} + \sqrt{x^2 + c^2} - (b + c)}{\frac{\lambda}{2}} \tag{3.7}$$

where $W_{l,i}^{\mathrm{Sp}}(\cdot)$ is the spatial windowing function for the edge of $w_{l,i}$. $a_{l,i}$ is the windowing size for the edge of $w_{l,i}$. $n(\cdot)$ is the Fresnel zone number. Fresnel zone can be considered as a ellipse region with the foci in Tx and Rx as shown in Fig. 3.8. Since the propagation path

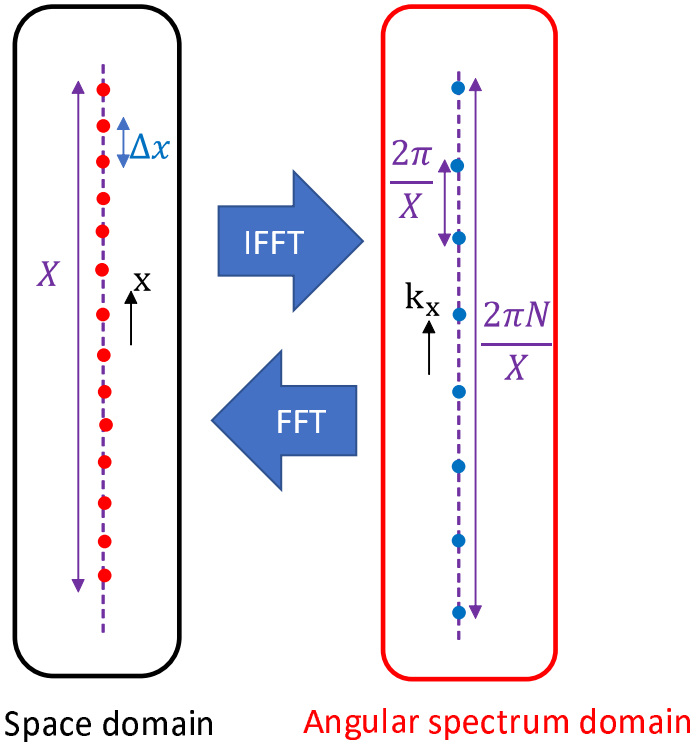

Figure 3.7: Discretization in the two domains

within the first Fresnel zone always has less than half wavelength phase rotation comparing with the LoS path, the energy is concentrated in primary Fresnel zone. That is the reason for the windowing function using Fresnel zone number.

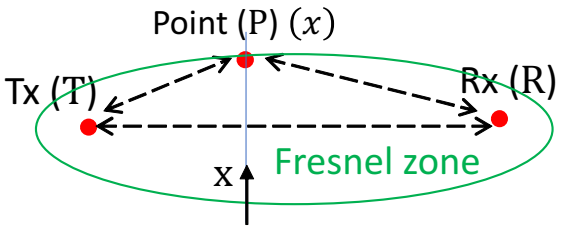

Figure 3.8: Fresnel zone

As shown in Fig. 3.9, the truncation error become smaller after the truncation via the above windowing function.

An electric line source with the cylindrical wave is considered as Tx. The field distributed on the zeroth plane can be calculated by KA as

$$E_{0,i}(u) = -\frac{k_0^2 I_0}{4\omega_0 \epsilon_0} H_0^{(2)}(k_0 \rho(u)) \tag{3.8}$$

where, I_0 is the magnitude of field of source and it can be arbitrary value since the calculation of shadowing cancels it. ω_0 is the angular frequency. ϵ_0 is the permittivity of vacuum. $\rho(u)$

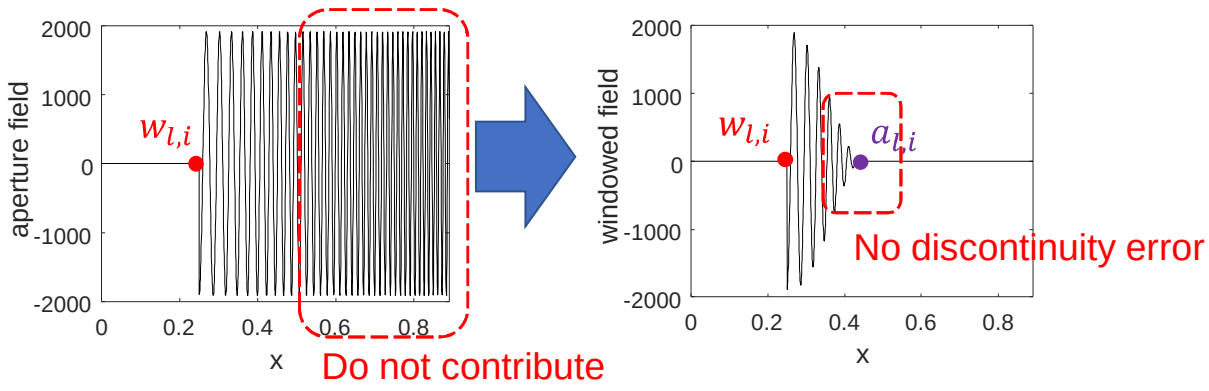

Figure 3.9: Aperture fields before and after the windowing truncation

is the distance vector pointing from Tx to point (u) on the zeroth plane.

The field distributed on the first plane can be calculated by the implementation of ASM as

$$\tilde{E}_{0,i}(p) = \frac{1}{2\pi} \sum_{u=1-\frac{N}{2}}^{\frac{N}{2}} E_{0,i}(u) W_{0,i}^{\mathrm{Sp}}(u) e^{\mathrm{j}2\pi(\frac{up}{N})} \frac{X}{N} \tag{3.9}$$

$$E_{1,i}(u) = \sum_{p=1-\frac{N}{2}}^{\frac{N}{2}} \tilde{E}_{0,i}(p) e^{-\mathrm{j}k_z d} e^{-\mathrm{j}2\pi(\frac{up}{N})} \frac{2\pi}{X} \tag{3.10}$$

The reflection from the shadowing object is introduced into the calculation of the double edge diffraction as

$$E_{1,i}^{\mathrm{MKA}}(u) = E_{1,i}(u) - E_{1,i}(2\left[\frac{w_{1,i}}{\Delta x}\right] - u) \tag{3.11}$$

where, $[\cdot]$ is the round function. The second term of right hand side corresponds to image field by mirror theory.

The field received at Rx on the second plane can be calculated by ASM again as

$$\tilde{E}_{1,i}(p) = \frac{1}{2\pi} \sum_{u=1-\frac{N}{2}}^{\frac{N}{2}} E_{1,i}^{\mathrm{MKA}}(u) W_{1,i}^{\mathrm{Sp}}(u) e^{\mathrm{j}2\pi(\frac{up}{N})} \frac{X}{N} \tag{3.12}$$

$$E^{\mathrm{Des}} = \sum_{i=1}^{2} \sum_{p=1-\frac{N}{2}}^{\frac{N}{2}} \tilde{E}_{1,i}(p) e^{-\mathrm{j}k_z(c-d)} e^{-\mathrm{j}2\pi(\frac{\left[\frac{x^{\mathrm{Rx}}}{\Delta x}\right]p}{N})} \frac{2\pi}{X} \tag{3.13}$$

where, x^{Rx} is the x-coordinate of Rx. The fields $E_{1,i}^{\mathrm{MKA}}$ for the region $i = 1, 2$ are calculated separately, until they reaches to the last plane where two fields are merged as shown in Fig. 3.10.

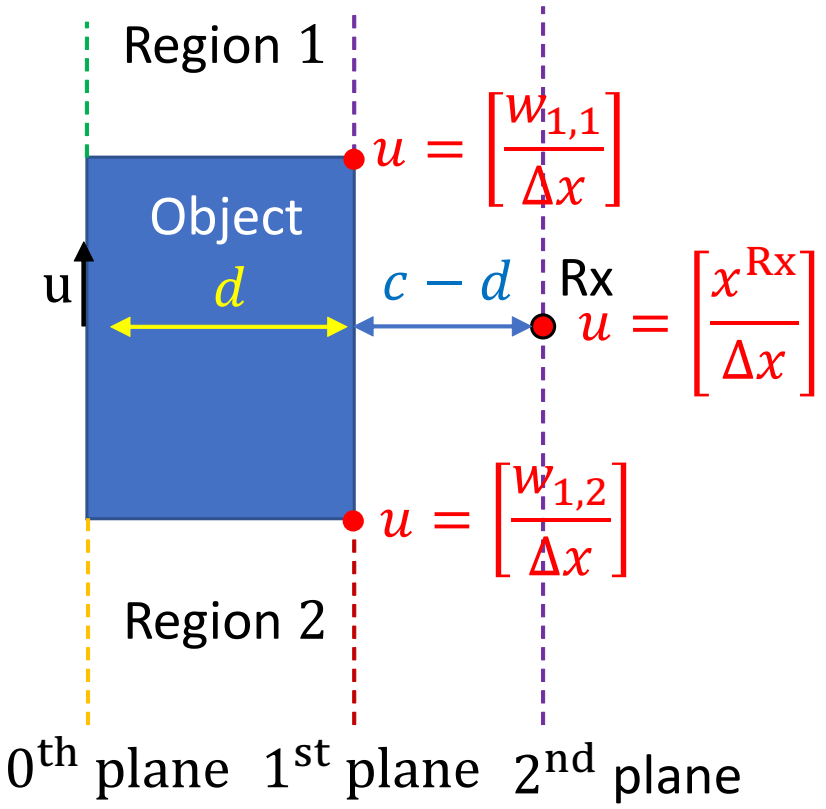

Figure 3.10: Image of formulations

For the final step, the total field in free space E^{Free} and the shadowing gain SG are determined by (3.14) and (3.15), respectively.

$$E^{\mathrm{Free}} = -\frac{k_0^2 I_0}{4\omega_0 \epsilon_0} H_0^{(2)}(k_0(b+c)) \tag{3.14}$$

.

$$\mathrm{SG} = 20 \log_{10} \frac{|E^{\mathrm{Des}}|}{|E^{\mathrm{Free}}|} \quad [\mathrm{dB}] \tag{3.15}$$

3.4 Simulations for A Rectangular Cylinder

This section introduces simulation for a rectangular cylinder by applying MKA. Simulation scenarios are explained in Subsection 3.4.1. Simulation results are shown in Subsection 3.4.2.

3.4.1 Simulation Scenarios

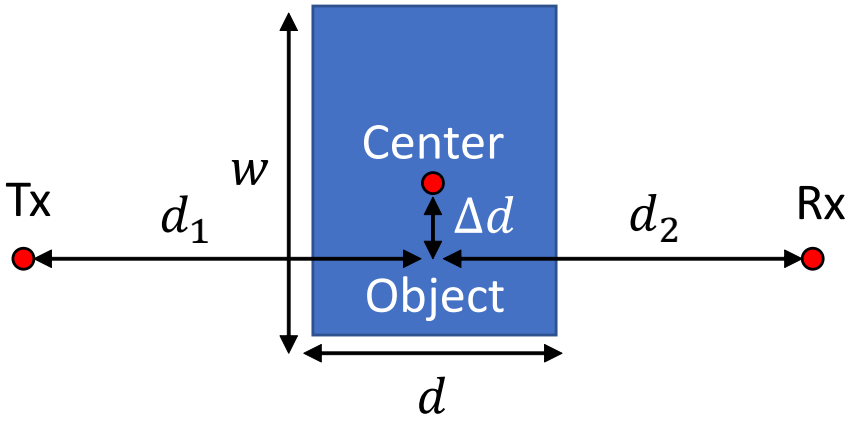

Figure 3.11: The environment of simulation (y-z vertical view)

As shown in Fig. 3.11, the environment of the simulation is explained as follows. w is the width of the rectangular cylinder. d is the thickness of the rectangular cylinder. d_1 is the distance between the center of the rectangular cylinder and Tx. d_2 is the distance between the center of the rectangular cylinder and Rx. f is frequency of simulation. Δd is the distance between the center of the rectangular cylinder and Tx-Rx line. The Δd is changed from -90λ m to 0 m with an interval of 0.1λ m. $\Delta d < 0$ means rectangular cylinder was located at the lower side of the Tx-Rx line. $\Delta d > 0$ means rectangular cylinder was located at the upper side of the Tx-Rx line. The d is changed from 0.001 m to 0.3 m with an interval of 0.001 m. The f is changed from 17 GHz to 66.5 GHz with an interval of 0.5 GHz. Each parameter of the environment and MKA are shown in Table 3.1 and Table 3.2, respectively.

Table 3.1: Environment Parameter

Parameter	Value
f (GHz)	17 : 0.5 : 66.5
d_1 (m)	2
d_2 (m)	8
w (m)	0.5
d (m)	0.001 : 0.001 : 0.3
Δd (λ)	-90 : 0.1 : 0

The windowing size is set for the convergence of results. The plane should be enough large for including the whole surface of the shadowing object and ensuring a good resolution of frequency spectral parameters [52].

Table 3.2: Parameters of MKA

Parameter	Value
FFT size N	2^{17}
Grid interval Δx (m)	0.1λ
Window size $n(a) - n(w_{l,i})$	19

For validating the accuracy of the proposed MKA, MoM as a reference is simulated. The piecewise constant function is selected as the basis function. MoM with point matching method for electric field integral equation is implemented by using MATLAB. To obtain the convergence result, the mesh size is set to $\frac{\lambda}{10}$.

3.4.2 Simulation Results

Firstly, when the thickness was fixed, the frequency was fixed at 66.5 GHz, and the distance was changed, the shadowing gain results of MKA and MoM were shown in Fig. 3.12 - Fig. 3.15 for $d = 0.01$ m, $d = 0.03$ m, $d = 0.1$ m and $d = 0.3$ m, respectively. The horizontal axis was Δd (m) introduced in Fig. 5.4. The vertical axis was shadowing gain result in decibel (dB) scale.

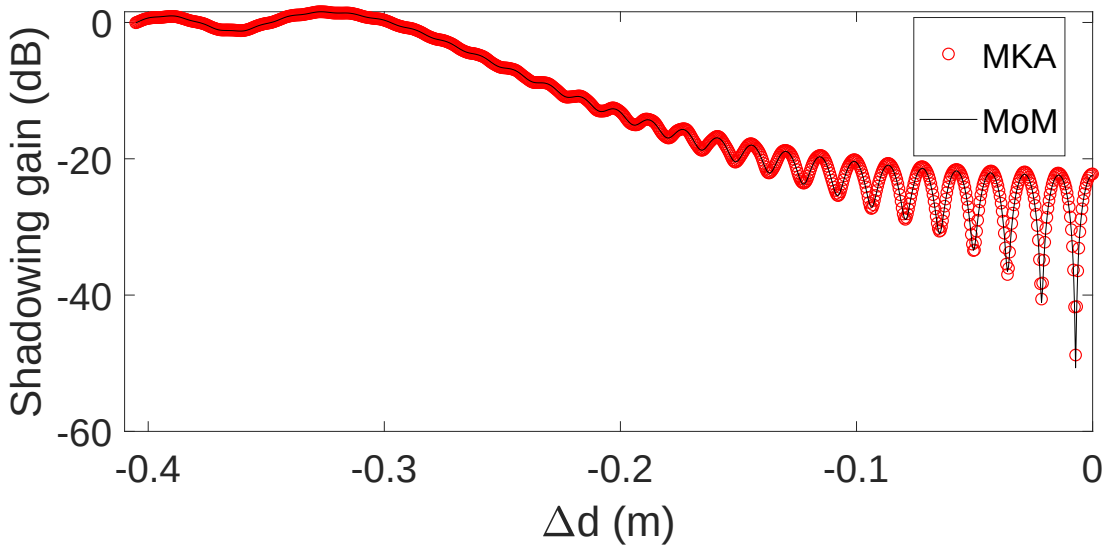

Figure 3.12: The plot of distance and shadowing gain for $d = 0.01$ m and $f = 66.5$ GHz

From the results, for each case, the proposed MKA was in good agreement with MoM. The proposal was validated by comparing with MoM for the shadowing characterization of the object's locations.

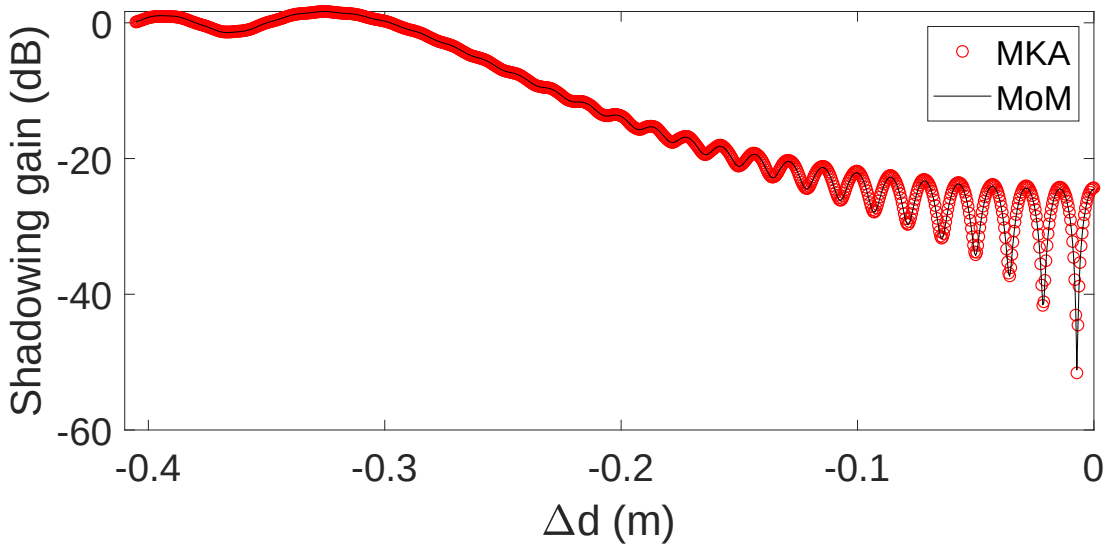

Figure 3.13: The plot of distance and shadowing gain for $d = 0.03$ m and $f = 66.5$ GHz

Secondly, when the distance was fixed at 0 m, the frequency was fixed at 66.5 GHz, and the thickness was changed, the relationship between thickness and shadowing gain was shown in Fig. 3.16. The horizontal axis was d (m) introduced in Fig. 5.4.

From the results, the proposed method provided good prediction results for the object with any thickness. The proposal was validated by comparing with MoM for the shadowing characterization of the object's thickness.

Thirdly, when the distance was fixed at 0 m, the thickness was fixed at 0.3 m, and the frequency was changed from 17 GHz to 66.5 GHz, the relationship between frequency and shadowing gain was shown in Fig. 3.17.

From the results, the proposed method provided good prediction results for the object with any frequencies. The proposal was validated by comparing with MoM for the shadowing characterization of the object's frequencies.

Furthermore, the calculation time was compared between MKA and MoM. The platform of calculating computer was Windows 10 Home. The processor of the calculating computer is an Intel(R) Core(TM) i7-8750H CPU @ 2.20 GHz. The usable installed memory of the calculating computer is 15.8 GB. The system type of the calculating computer is 64-bit operating system with a x64-based processor. The usable installed memory of the calculating computer was 15.8 GB. The simulation software was MATLAB. The result of the relation between thickness and calculation time was shown in Fig. 3.18 for $\Delta d = 0$ m and $f = 66.5$ GHz. The result of the relation between frequency and calculation time was shown in Fig. 3.19 for $\Delta d = 0$ m and $d = 0.3$ m. The vertical axis was calculation time (s) on a logarithmic scale.

The calculation time of the proposed MKA was about 0.21 s for any thickness or fre-

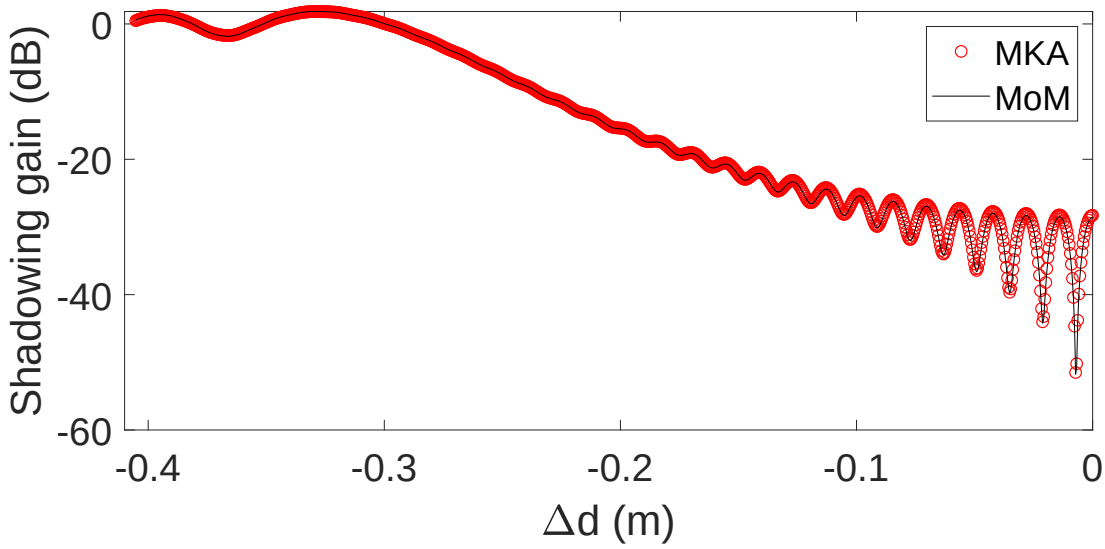

Figure 3.14: The plot of distance and shadowing gain for $d = 0.1$ m and $f = 66.5$ GHz

quency. The calculation time of MoM was about from 82.45 s to 192.12 s for increasing thickness at $f = 66.5$ GHz and from 14.07 s to 192.12 s for increasing frequency at $d = 0.3$ m. Comparing with full-wave MoM, the MKA could provide a fast calculation speed.

3.5 Conclusion

In this Chapter, the concept of MKA was introduced. Detailed formulations were provided and explained. Simulations for validated the proposal were conducted for a rectangular cylinder. The results were compared with MoM in terms of accuracy and computational cost. Objective 1 has been achieved.

However, two issues were remaining. Firstly, the MKA's parameters in Table 3.2 is not designed. The calculation time with FFT size of $N = 2^{17}$ was overly high. If we formulated those parameters reasonably, the computational cost might be less than UTD. Chapter four designed those parameters. Secondly, current MKA was only suitable for the rectangular cylinder. The extension for the arbitrarily shaped cylinder was needed. Chapter five extended MKA.

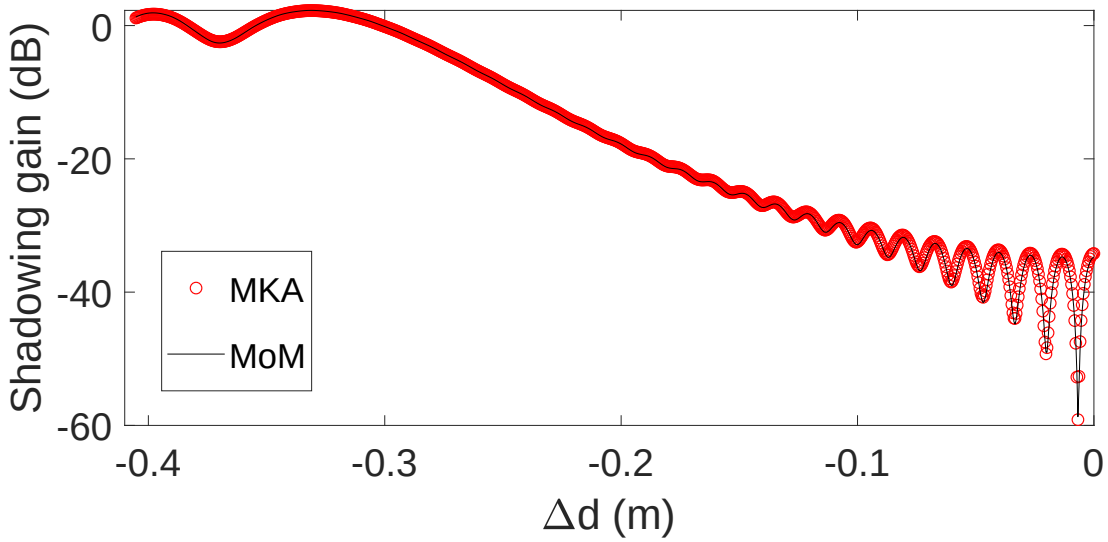

Figure 3.15: The plot of distance and shadowing gain for $d = 0.3$ m and $f = 66.5$ GHz

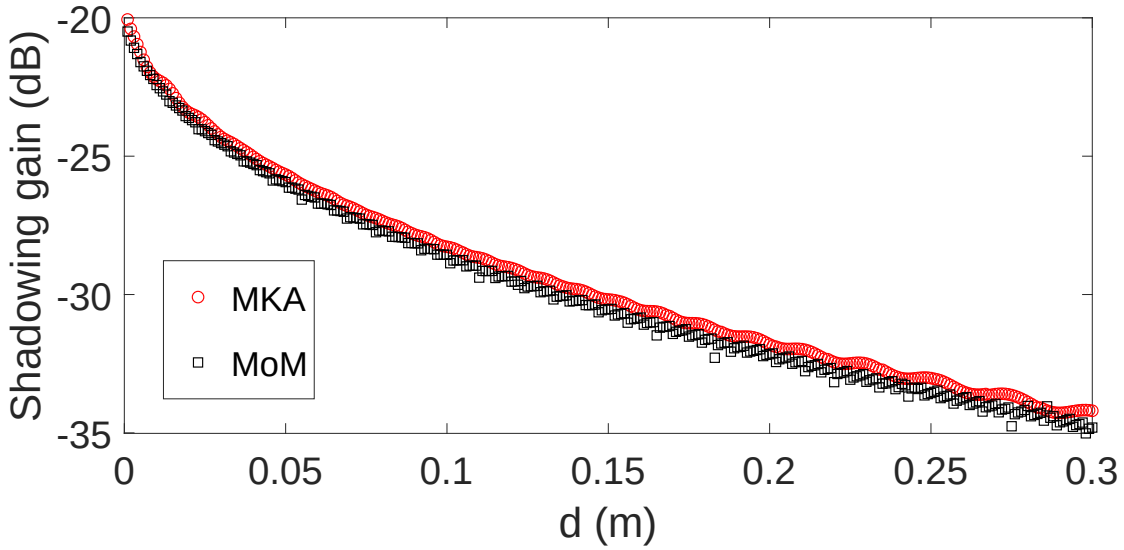

Figure 3.16: The relation between thickness and shadowing gain for $\Delta d = 0$ m and $f = 66.5$ GHz

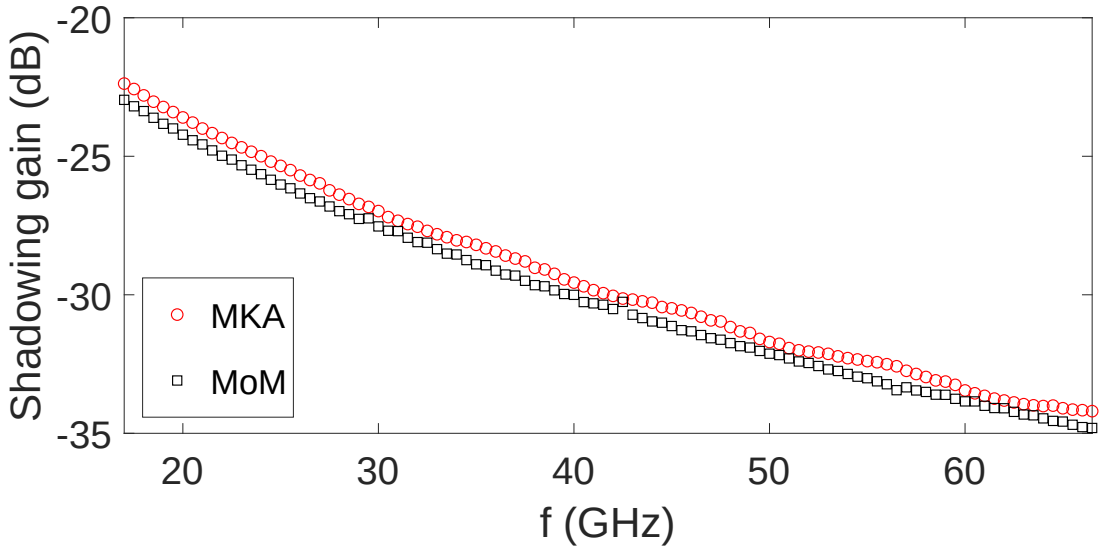

Figure 3.17: The relation between frequency and shadowing gain for $\Delta d = 0$ m and $d = 0.3$ m

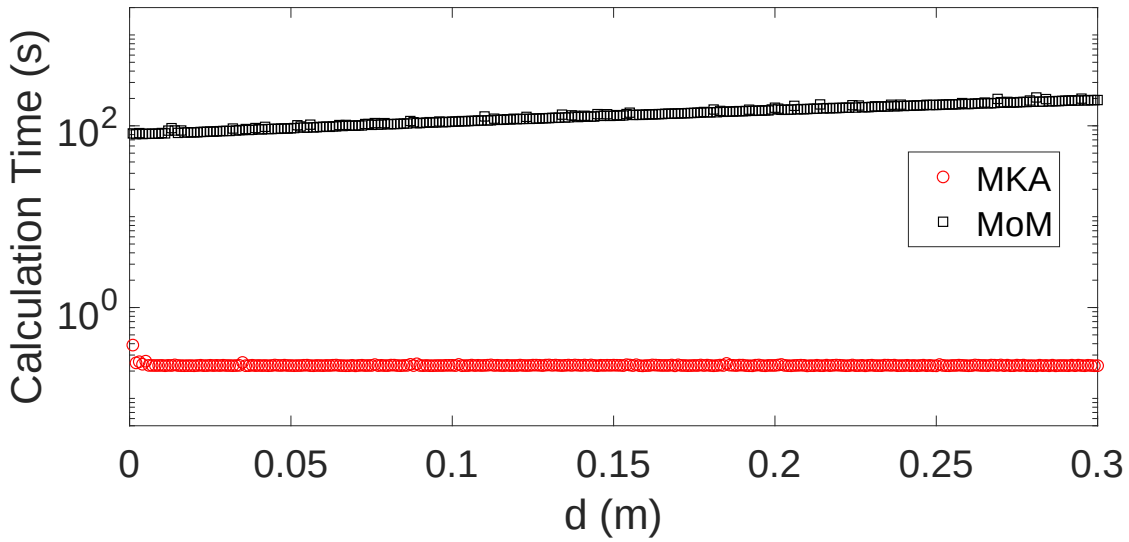

Figure 3.18: The relation between thickness and calculation time for $\Delta d = 0$ m and $f = 66.5$ GHz

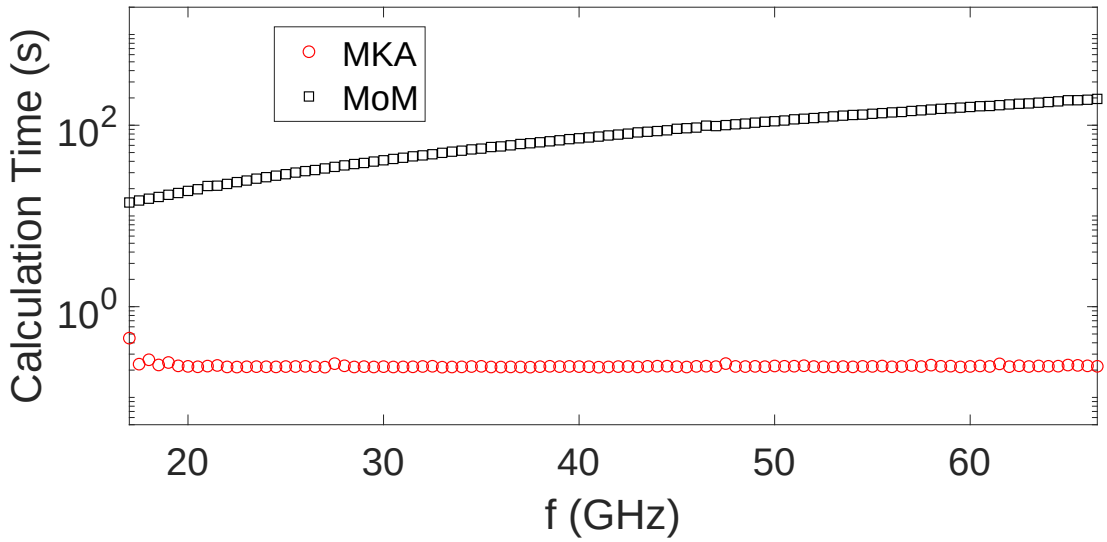

Figure 3.19: The relation between frequencies and calculation time for $\Delta d = 0$ m and $d = 0.3$ m

Chapter 4

Design of Simualtion Parameters for MKA

4.1 Introduction

This chapter will introduce the design of simulation parameters for MKA. Since FFT size is determined by $X/\Delta x$, there are two ways to reduce the calculation complexity, i.e., increasing Δx and decreasing X.

Normally, $[-X/2, X/2]$ and $[-k_0, k_0]$ are considered as the ranges of truncated regions in the space and angular spectrum domains, respectively. However, by using the Nyquist [143] and $\lambda/10$ sampling criteria, the author proposes $[-a, a]$ $(2a < X)$ and $[-k_{\mathrm{w}}, k_{\mathrm{w}}]$ $(k_{\mathrm{w}} < k_0)$ as the ranges of truncated regions in the space and angular spectrum domains, respectively, for better accuracy and lower calculation cost.

Section 4.2 proposes Δx, which considers the Nyquist sampling criterion for including the evanescent wave. Section 4.3 proposes a and updates Δx to $\Delta x'$, which considers the $\lambda/10$ sampling criterion. Section 4.4 and Section 4.5 propose X and k_{w}, respectively.

4.2 Discretization in Space Domain

This section discusses the spatial resolution. Usually, the calculation ignores the evanescent wave ($|k_{\mathrm{x}}| > k_0$). However, when the value of d is small, the evanescent wave with the value of $e^{-\sqrt{k_{\mathrm{x}}^2 - k_0^2}d}$ still contributes to the calculation. The author defines the negligible value of factor $e^{-\sqrt{k_{\mathrm{x}}^2 - k_0^2}d}$ as ϵ. Then, the condition of $e^{-\sqrt{k_{\mathrm{x}}^2 - k_0^2}d} = \epsilon$ gives the maximum value of k_{x} as (4.1) and the Nyquist sampling criterion $\Delta x \leq \pi / \max(k_{\mathrm{x}})$ calculates the proposed Δx by (4.2).

$$\max(k_{\mathrm{x}}) = \sqrt{k_0^2 + \left(\frac{\ln \epsilon}{d}\right)^2} \tag{4.1}$$

$$\Delta x = \frac{\pi}{\sqrt{k_0^2 + (\frac{\ln \epsilon}{d})^2}} \tag{4.2}$$

4.3 Truncation in Space Domain

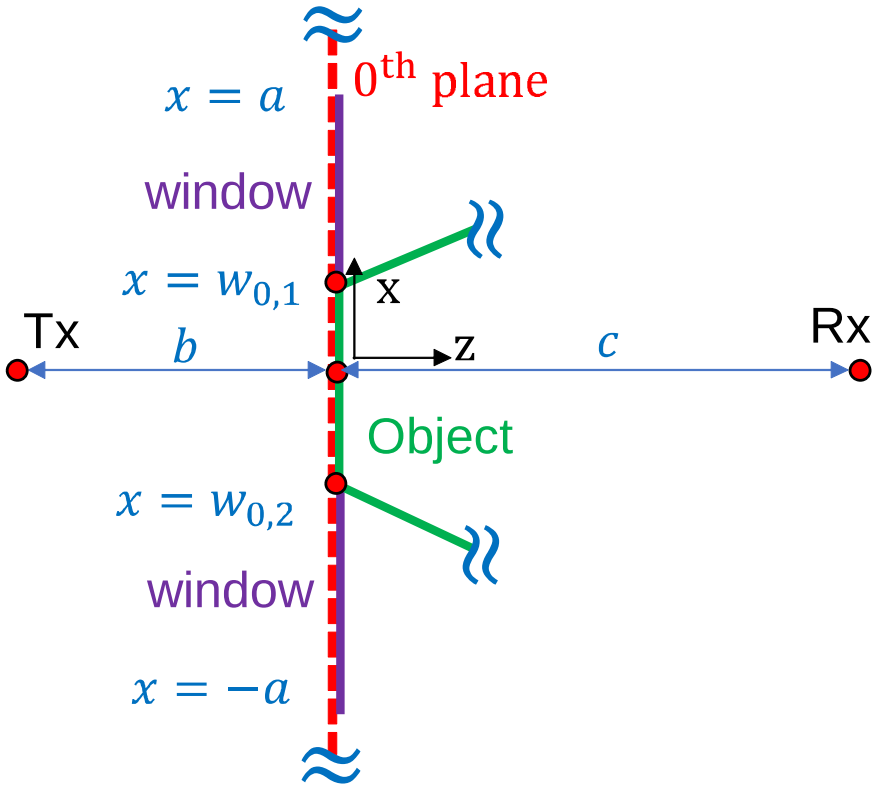

Figure 4.1: Model of spatial window for the zeroth plane.

The proposed Δx may not satisfy $\lambda/10$ sampling criterion, which is widely used for accuracy [144]. The meaning of $\lambda/10$ sampling criterion is that there are at least ten sampling points in one phase period (one cycle of phase rotation), which is sufficient. This section formulates the size of the spatial truncation region and updates the spatial interval when considering $\lambda/10$ sampling criterion.

Figure 4.1 shows the model of truncation by the spatial window. An object shadows the line-of-sight (LoS) path, which is defined as z-axis, between a transmitter (Tx) and a receiver (Rx). The point of the surface of the object closest to Tx is defined as zeroth plane $z = 0$, which is perpendicular to z-axis. The distances from the zeroth plane to Tx and Rx are b and c, respectively. $w_{0,i}$ $(i = 1, 2)$ is the x-coordinate of two object edges in the zeroth plane. a is the window size. The cylindrical wave incident to the zeroth plane can be calculated using the Hankel function of the second kind $H_0^{(2)}(k_0\sqrt{x^2 + b^2})$. Assuming $k_0 b \gg 1$ and $x \ll b$, the Fresnel region approximation [145] is applied as (4.3).

$$H_0^{(2)}\left(k_0\sqrt{x^2 + b^2}\right) \approx H_0^{(2)}(k_0 b)e^{-\mathrm{j}\frac{k_0}{2b}x^2} \tag{4.3}$$

Figure 4.4 shows an example of the plots of left and right hand sides of (4.3) with the values of $b = 2.15$ m and $k_0 = 1394$ rad/m ($\lambda = 4.5$ mm) [144] to validate Fresnel region approximation. We can find that Fresnel region approximation provides good accuracy near the edge.

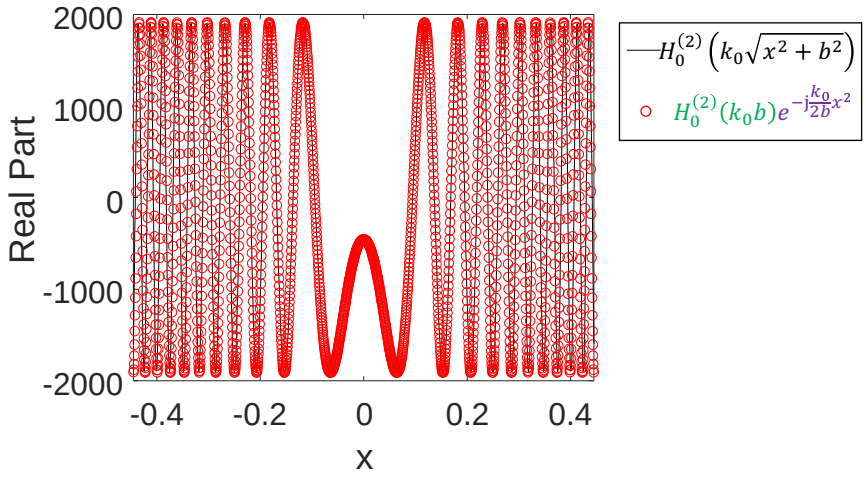

Figure 4.2: Comparison between Fresnel region approximation and original function.

Equation (4.3) gives two key intuitions (P1–P2):

- **P1: Constant Amplitude in Space Domain**
  The complex amplitude term $H_0^{(2)}(k_0 b)$ is constant at approximately $x \simeq 0$. Truncation by a rectangular windowing function will cause the boundary discontinuity, which takes the extra truncation error in the edge. Thus, there is a need for a decay windowing function to reduce the truncation error.

- **P2: Decreasing Phase Period in Space Domain**
  The phase term $e^{-\mathrm{j}\frac{k_0}{2b}x^2}$ is x^2-dependent around $x = 0$. Thus, the phase period around $x = 0$ is much larger than λ and decreases when x is larger. However, the phase period converges to λ, as shown in Fig. 4.3.

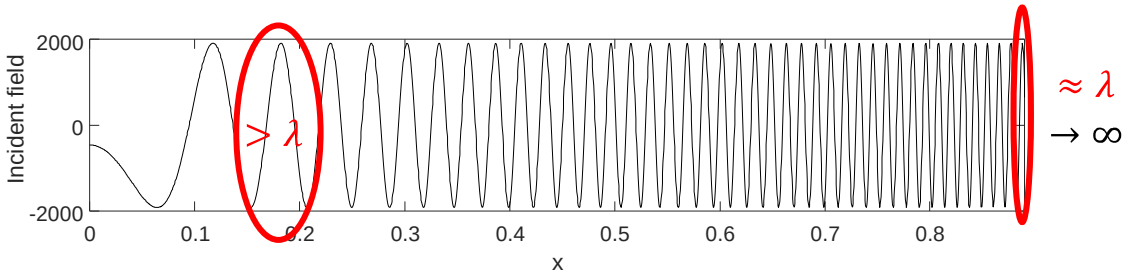

Figure 4.3: Decreasing phase period of aperture fields

Figure 4.4(a) shows an example of the plot of Hankel function with the same parameters as Fig. 4.2 to visualize the behaviour of the above key intuitions P1–P2. The black line is the plot with the interval of $\lambda/10$ as a reference. The red points are the plot with the interval of proposed Δx in (4.2), which is larger than $\lambda/10$. We can observe that there are more than ten red sampling points in the phase period near z-axis. Thus, for the shadowing problem where a region of interest is near the edge, the interval of Δx near the edge can satisfy ten sampling points within one phase period there.

The region far away from the edge, where the integral of the rapidly oscillating function $E_{0,i}(x)e^{\mathrm{j}k_{\mathrm{x}}x}$ does not contribute to the final integral due to the cancellation, can be truncated. The vanishing region can be numerically integrated in vain if the number of samples per phase period is sufficiently large, e.g., 10. However, the interval of Δx in phase period far away from the edge may not provide sufficient sampling points according to key intuition P2. The numerical integration of vanishing region is erroneous when the number of samples per phase period is insufficiently small. Therefore, it is better to truncate rather than to inaccurately numerically integrate the region. The radiation integral can be cancelled if the phase change number $n_{\mathrm{p}} \geq 7$ (at least 7π phase change) [109]. Figure 4.4(b) is the windowed truncation of Fig. 4.4(a) with the values of $w_{0,1} = -w_{0,2} = 0.25$ m and $n_{\mathrm{p}} = 7$. The author updates Δx of (4.2) to $\Delta x'$ as (4.4), which can satisfy each phase period within the window that should be sampled by at least n_{s} sampling points ($n_{\mathrm{s}} = 10$ for $\lambda/10$ sampling criterion). The derivation of (4.4) is shown in Appendix A.

$$\Delta x' = \min_{i=1,2} \left(\Delta x, \frac{\sqrt{w_{0,i}^2 + \frac{2bn_{\mathrm{p}}\pi}{k_0}} - \sqrt{w_{0,i}^2 + \frac{2b(n_{\mathrm{p}}-2)\pi}{k_0}}}{n_{\mathrm{s}}} \right) \tag{4.4}$$

For the LoS case, $w_{0,i}$ is replaced by 0 in (3.6)–(4.4). Appendix A also derives the spatial windowing size a as (4.5).

$$a = \frac{n_{\mathrm{s}}^2 k_0 \Delta x'^2 + 4\pi b}{2n_{\mathrm{s}} k_0 \Delta x'} \tag{4.5}$$

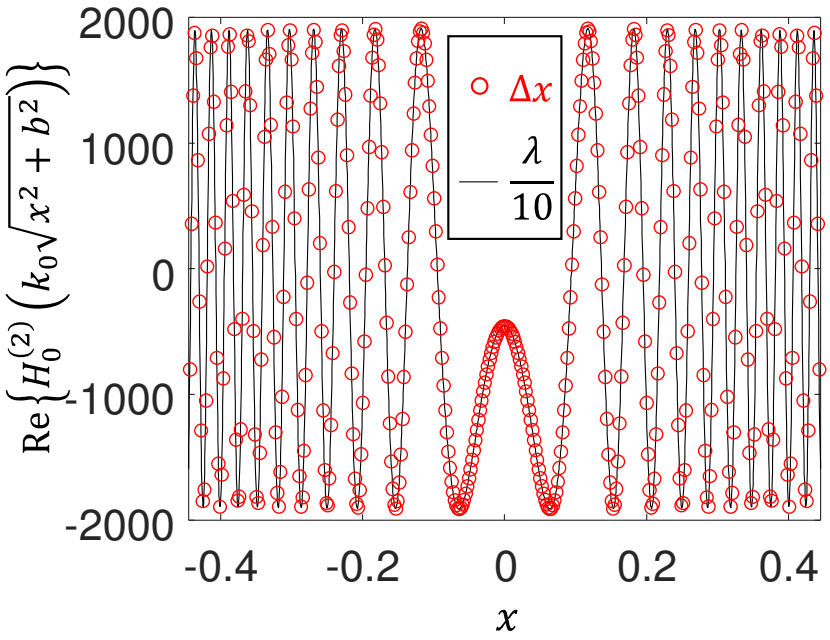

(a) Before the windowing truncation.

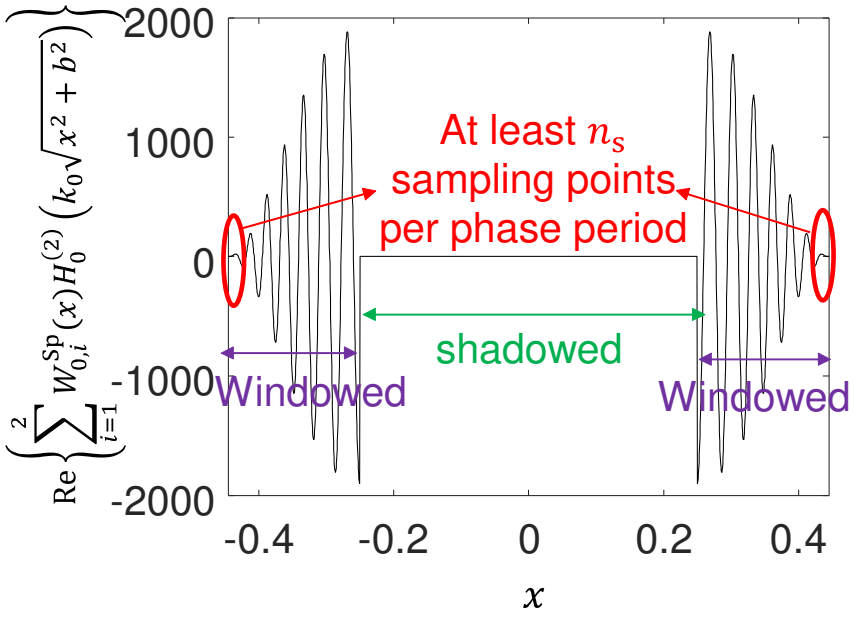

(b) After the windowing truncation.

Figure 4.4: The field distributed on the zeroth plane.

4.4 Discretization in Angular Spectrum Domain

Although in real MKA calculation, numerical approach is used, this section provides an analytical approach, not to calculate the shadowing results, but for to formulates the angular spectrum resolution. The windowed field distributed on the region $|x-w_{0,i}| \leq a$ of the zeroth plane is approximated as

$$\frac{n(x)-n(w_{0,i})}{n(a)-n(w_{0,i})} \approx \frac{x^2-w_{0,i}^2}{a^2-w_{0,i}^2} \quad (\text{for } \; w_{0,i}, a, x \ll b, c) \tag{4.6}$$

$$E_{0,i}(x) \approx \frac{1}{2} H_0^{(2)}(k_0 b) e^{-\mathrm{j}\frac{k_0}{2b}x^2} (\cos(\frac{x^2-w_{0,i}^2}{a^2-w_{0,i}^2}\pi)+1) \tag{4.7}$$

substituting (4.7) into (3.1), $\tilde{E}_{0,i}(k_\mathrm{x})$ can be analytically approximated as

$$\begin{aligned}
\tilde{E}_{0,i}(k_\mathrm{x}) \approx H_0^{(2)}(k_0 b) \Bigg[& \frac{1}{2}\sqrt{\frac{b\pi}{k_0}} e^{\mathrm{j}\frac{bk_\mathrm{x}^2}{2k_0}} \left\{ C\left(\frac{\frac{a}{b}k_0-k_\mathrm{x}}{\sqrt{\frac{k_0\pi}{b}}}\right) - \mathrm{j}S\left(\frac{\frac{a}{b}k_0-k_\mathrm{x}}{\sqrt{\frac{k_0\pi}{b}}}\right) - C\left(\frac{\frac{w_{0,i}}{b}k_0-k_\mathrm{x}}{\sqrt{\frac{k_0\pi}{b}}}\right) \right. \\
& \left. + \mathrm{j}S\left(\frac{\frac{w_{0,i}}{b}k_0-k_\mathrm{x}}{\sqrt{\frac{k_0\pi}{b}}}\right) \right\} + \frac{1}{4}\sqrt{\frac{\pi}{2\left(\frac{k_0}{2b}-\frac{\pi}{a^2-w_{0,i}^2}\right)}} e^{\mathrm{j}\left(\frac{k_\mathrm{x}^2}{4\left(\frac{k_0}{2b}-\frac{\pi}{a^2-w_{0,i}^2}\right)}-\frac{w_{0,i}^2\pi}{a^2-w_{0,i}^2}\right)} \\
& \times \left\{ C\left(\frac{2\left(\frac{k_0}{2b}-\frac{\pi}{a^2-w_{0,i}^2}\right)a-k_\mathrm{x}}{2\pi\left(\frac{k_0}{2b}-\frac{\pi}{a^2-w_{0,i}^2}\right)}\right) - \mathrm{j}S\left(\frac{2\left(\frac{k_0}{2b}-\frac{\pi}{a^2-w_{0,i}^2}\right)a-k_\mathrm{x}}{2\pi\left(\frac{k_0}{2b}-\frac{\pi}{a^2-w_{0,i}^2}\right)}\right) \right. \\
& \left. - C\left(\frac{2\left(\frac{k_0}{2b}-\frac{\pi}{a^2-w_{0,i}^2}\right)w_{0,i}-k_\mathrm{x}}{2\pi\left(\frac{k_0}{2b}-\frac{\pi}{a^2-w_{0,i}^2}\right)}\right) + \mathrm{j}S\left(\frac{2\left(\frac{k_0}{2b}-\frac{\pi}{a^2-w_{0,i}^2}\right)w_{0,i}-k_\mathrm{x}}{2\pi\left(\frac{k_0}{2b}-\frac{\pi}{a^2-w_{0,i}^2}\right)}\right) \right\} \\
& + \frac{1}{4}\sqrt{\frac{\pi}{2\left(\frac{k_0}{2b}+\frac{\pi}{a^2-w_{0,i}^2}\right)}} e^{\mathrm{j}\left(\frac{k_\mathrm{x}^2}{4\left(\frac{k_0}{2b}+\frac{\pi}{a^2-w_{0,i}^2}\right)}+\frac{w_{0,i}^2\pi}{a^2-w_{0,i}^2}\right)} \left\{ C\left(\frac{2\left(\frac{k_0}{2b}+\frac{\pi}{a^2-w_{0,i}^2}\right)a-k_\mathrm{x}}{2\pi\left(\frac{k_0}{2b}+\frac{\pi}{a^2-w_{0,i}^2}\right)}\right) \right. \\
& - \mathrm{j}S\left(\frac{2\left(\frac{k_0}{2b}+\frac{\pi}{a^2-w_{0,i}^2}\right)a-k_\mathrm{x}}{2\pi\left(\frac{k_0}{2b}+\frac{\pi}{a^2-w_{0,i}^2}\right)}\right) - C\left(\frac{2\left(\frac{k_0}{2b}+\frac{\pi}{a^2-w_{0,i}^2}\right)w_{0,i}-k_\mathrm{x}}{2\pi\left(\frac{k_0}{2b}+\frac{\pi}{a^2-w_{0,i}^2}\right)}\right) \\
& \left. + \mathrm{j}S\left(\frac{2\left(\frac{k_0}{2b}+\frac{\pi}{a^2-w_{0,i}^2}\right)w_{0,i}-k_\mathrm{x}}{2\pi\left(\frac{k_0}{2b}+\frac{\pi}{a^2-w_{0,i}^2}\right)}\right) \right\} \Bigg]
\end{aligned} \tag{4.8}$$

where $S(\cdot), C(\cdot)$ are the Fresnel integrals and the integral formula is applied as

$$\int \cos(\alpha x^2+\beta x+\gamma)\mathrm{d}x = \sqrt{\frac{\pi}{2\alpha}}\left\{\cos\left(\frac{\beta^2}{4\alpha}-\gamma\right)C\left(\frac{\beta+2\alpha x}{\sqrt{2\pi\alpha}}\right)+\sin\left(\frac{\beta^2}{4\alpha}-\gamma\right)S\left(\frac{\beta+2\alpha x}{\sqrt{2\pi\alpha}}\right)\right\} + \text{constant} \quad (\alpha,\beta,\gamma-\text{arbitrary coefficients}) \tag{4.9}$$

Using the asymptotic forms of $S(\cdot), C(\cdot)$ as

$$S(x) \sim \frac{1}{2}-\frac{1}{\pi x}\cos\left(\frac{\pi}{2}x^2\right) \tag{4.10a}$$

$$C(x) \sim \frac{1}{2}+\frac{1}{\pi x}\sin\left(\frac{\pi}{2}x^2\right) \tag{4.10b}$$

an asymptotic form of $\tilde{E}_{0,i}(k_\mathrm{x})$ can be analytically calculated as

$$\tilde{E}_{0,i}(k_\mathrm{x}) \sim H_0^{(2)}(k_0 b)\mathrm{j}\left[e^{-\mathrm{j}\left(\frac{a^2k_0}{2b}-ak_\mathrm{x}\right)}\left\{\frac{\frac{1}{2}}{\frac{a}{b}k_0-k_\mathrm{x}}-\frac{\frac{1}{4}}{\frac{a}{b}k_0-\frac{2a\pi}{a^2-w_{0,1}^2}-k_\mathrm{x}}-\frac{\frac{1}{4}}{\frac{a}{b}k_0+\frac{2a\pi}{a^2-w_{0,1}^2}-k_\mathrm{x}}\right\}\right.$$
$$\left.-e^{-\mathrm{j}\left(\frac{w_{0,1}^2k_0}{2b}-w_{0,1}k_\mathrm{x}\right)}\left\{\frac{\frac{1}{2}}{\frac{w_{0,1}}{b}k_0-k_\mathrm{x}}+\frac{\frac{1}{4}}{\frac{w_{0,1}}{b}k_0-\frac{2w_{0,1}\pi}{a^2-w_{0,1}^2}-k_\mathrm{x}}+\frac{\frac{1}{4}}{\frac{w_{0,1}}{b}k_0+\frac{2w_{0,1}\pi}{a^2-w_{0,1}^2}-k_\mathrm{x}}\right\}\right] \tag{4.11}$$

There are three reasons that the above analytical results cannot be used to directly evaluate the shadowing gain. Firstly, the above analytical results use many approximations causing the additional errors to the final results. Secondly, to evaluate the final results, we need to integral the above results again and again. However, unfortunately, there is no analytic solution for the further integration. Thirdly, even for (4.8), which has no asymptotic approximation compared with (4.11), the calculation time of (4.8) may slower than numerical approach since it uses a lot of special functions. Although (4.11) can only provide the rough approximation compared with numerical integration, it still gives three key intuitions (P3–P5):

- **P3: Amplitude Poles in Angular Spectrum Domain**
  From (4.11), we can find that $k_\mathrm{x}=k_0a/b$ and $k_\mathrm{x}=k_0w_{0,i}/b$ are the highest poles of the asymptotic form of $\tilde{E}_{0,i}(k_\mathrm{x})$. Those values correspond to the directions of incident rays to the edges of window and object in ray tracing. The peaks of oscillating $\tilde{E}_{0,i}(k_\mathrm{x})$ around those poles make the significant contribution to the integral.

- **P4: Constant Phase Period of $\tilde{E}_{0,i}(k_\mathrm{x})$**
  The phase of $\tilde{E}_{0,i}(k_\mathrm{x})$ is k_x-dependent. Thus, the phase period with the size of $2\pi/|w_{0,i}|$ and $2\pi/a$ are constant everywhere of k_x.

- **P5: Decay Amplitude in Angular Spectrum Domain**
  The envelope of $\tilde{E}_{0,i}(k_\mathrm{x})$ is k_x^{-1}-dependent. $\tilde{E}_{0,i}(k_\mathrm{x})$ decays fast when k_x is far away from peaks. This characteristic influences the selection of the windowing function.

The above gives the characteristics of $\tilde{E}_{0,i}(k_\mathrm{x})$. However, for conducting the next FT by (3.2), the complex factor $\tilde{E}_{0,i}(k_\mathrm{x})e^{-\mathrm{j}k_\mathrm{z}d}$ should be analyzed. The author approximates the complex factor $e^{-\mathrm{j}k_\mathrm{z}d}$ near $k_\mathrm{x}=0$ as (4.12).

$$e^{-\mathrm{j}k_\mathrm{z}d}=e^{-\mathrm{j}\sqrt{k_0^2-{k_\mathrm{x}}^2}d}\approx e^{-\mathrm{j}(k_0-\frac{{k_\mathrm{x}}^2}{2k_0})d} \tag{4.12}$$

Equation (4.12) is identical for the Fresnel region approximation (4.3) but in the angular spectrum domain. This approximation gives key intuition P6:

- **P6: Decreasing Phase Period of $e^{-\mathrm{j}k_\mathrm{z}d}$**
  The phase of $e^{-\mathrm{j}k_\mathrm{z}d}$ is ${k_\mathrm{x}}^2$-dependent near the line of sight. Thus, $e^{-\mathrm{j}k_\mathrm{z}d}$ has a deceasing phase period with an increase in $|k_\mathrm{x}|$.

The phase of $\tilde{E}_{0,i}(k_\mathrm{x})e^{-\mathrm{j}k_\mathrm{z}d}$ can be classified into two cases C1 and C2, by using (4.11) and (4.12).

- **C1: Constant Phase Period in Angular Spectrum Domain for Small d**
  In case of small d ($d<2a$), from the inequality relation (4.13), $\tilde{E}_{0,i}(k_\mathrm{x})$ dominates the phase of $\tilde{E}_{0,i}(k_\mathrm{x})e^{-\mathrm{j}k_\mathrm{z}d}$. Thus, by key intuition P4, the phase period is constant in the angular spectrum domain.

$$\frac{d}{2k_0}{k_\mathrm{x}}^2\leq\frac{d}{2}k_\mathrm{x}<ak_\mathrm{x} \tag{4.13}$$

- **C2: Decreasing Phase Period in Angular Spectrum Domain for Large d**
  In case of large d, factor $e^{-\mathrm{j}k_\mathrm{z}d}$ dominates the phase of $\tilde{E}_{0,i}(k_\mathrm{x})e^{-\mathrm{j}k_\mathrm{z}d}$. Thus, by key intuition P6, the phase period is decreasing in the angular spectrum domain.

Using the above phase informations, the author proposes X corresponding to the angular spectrum interval as follows. From key intuition P3, the phase period at poles should be sampled by n_s points for accuracy in the angular spectrum domain. For the LoS condition, $k_\mathrm{x}=0$ corresponding to the directions of the direct ray is the main peak. For the NLoS condition, the poles of $\tilde{E}_{0,i}(k_\mathrm{x})e^{-\mathrm{j}k_\mathrm{z}d}$ are $k_\mathrm{x}=k_0a/b$ and $k_\mathrm{x}=k_0w_{0,i}/b$, which is the same as the poles of $\tilde{E}_{0,i}(k_\mathrm{x})$ due to $|\tilde{E}_{0,i}(k_\mathrm{x})e^{-\mathrm{j}k_\mathrm{z}d}|=|\tilde{E}_{0,i}(k_\mathrm{x})|$. Additionally, for case without the spatial windowing truncation, since the terms including a in (4.11) vanish for $a\to\infty$, pole of $k_\mathrm{x}=k_0a/b$ and phase term of ak_x disappear. Using the phase informations of cases C1 and C2, the author proposes X as (4.14).

$$X_1=n_\mathrm{s}a \tag{4.14a}$$

$$X_2=\frac{n_\mathrm{s}da}{b} \tag{4.14b}$$

$$X_3=\max_{i=1,2}n_\mathrm{s}|w_{0,i}| \tag{4.14c}$$

$$X_4=\max_{i=1,2}\frac{n_\mathrm{s}d|w_{0,i}|}{b} \tag{4.14d}$$

where X_1 is the proposed X in case C1 or case C2 for the LoS condition with the spatial windowing truncation. X_2 is the proposed X in case C2 for the NLoS condition with the spatial windowing truncation. X_3 is the proposed X in case C1 or case C2 for the LoS condition without the spatial windowing truncation. X_4 is the proposed X in case C2 for the NLoS condition without the spatial windowing truncation. The derivation of (4.14) is shown in Appendix B.

4.5 Truncation in Angular Spectrum Domain

This section formulates the size of the angular spectrum truncation region. In case C1, there is no need to consider the extra discretization error by equally sampled points since the phase period is almost constant. However, there is a vast discretization error for equally-sampling points in case C2 since the phase period decreases with the increase of $|k_{\mathrm{x}}|$.

The region far away from the poles in the angular spectrum domain, where the integral of the oscillating function does not contribute to the final integral, should be truncated rather than inaccurately numerically integrate the insufficiently sampled region. The angular spectrum domain is truncated by using the rectangular windowing function for case C2. The rectangular windowing function is chosen because the amplitude of $\tilde{E}_{0,i}(k_{\mathrm{x}})e^{-\mathrm{j}k_{\mathrm{z}}d}$ is $|\tilde{E}_{0,i}(k_{\mathrm{x}})|$, which decays fast according to key intuition P5. Thus, a rectangular windowing function results in a negligibly small truncation error. Figures 4.5(a) and (b) show the examples before and after the truncation with the value of $d = 7.85$ m in the same condition as Fig. 4.4(b) [144]. The windowing function for the angular spectrum domain is (4.15).

$$W^{\mathrm{An}}(k_{\mathrm{x}}) = \begin{cases} 1 & (|k_{\mathrm{x}}| \leq k_{\mathrm{w}}) \\ 0 & (|k_{\mathrm{x}}| > k_{\mathrm{w}}) \end{cases} \tag{4.15}$$

where $W^{\mathrm{An}}(\cdot)$ is the angular spectrum windowing function. k_{w} is the window size in the angular spectrum domain and is proposed as (4.16).

$$k_{\mathrm{w}} = \frac{k_0 X_\alpha}{n_{\mathrm{c}} d} \quad (\alpha = 1, 2, 3, 4) \tag{4.16}$$

where, n_{c} is the Nyquist sampling number per phase period, i.e., 2. The derivation of (4.16) is shown in Appendix B. Appendix B also explains the reason for using the Nyquist sampling criterion in the angular spectrum domain, which is different from $\lambda/10$ sampling criterion in the space domain.

4.6 Conclusion

In this Chapter, the design of the simulation parameters for MKA was proposed. We evaluated FFT size for the double diffraction mentioned in [144]. Comparing FFT size with value of 2^{17} set in Chapter 3 for one test, the MKA with the designed parameters only need $2^{10} \sim 2^{11}$ points for one test.

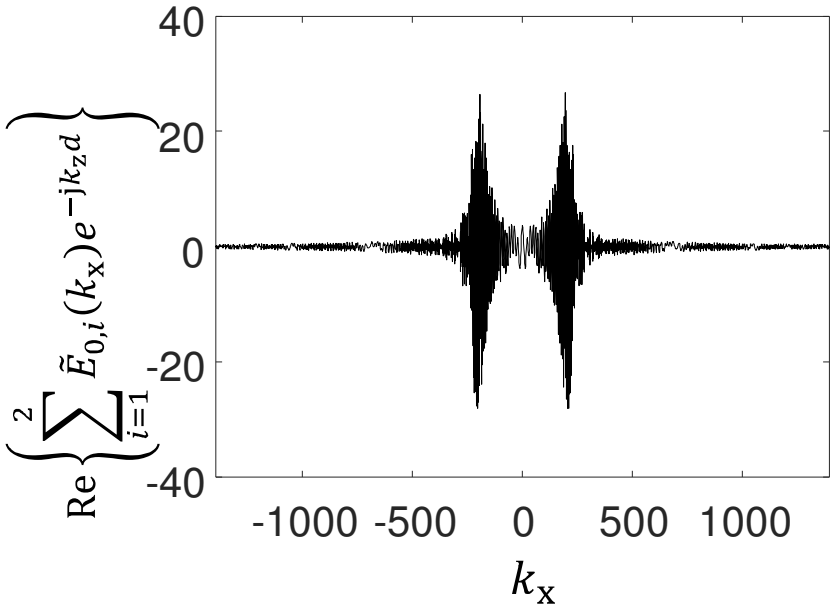

(a) Before the windowing truncation.

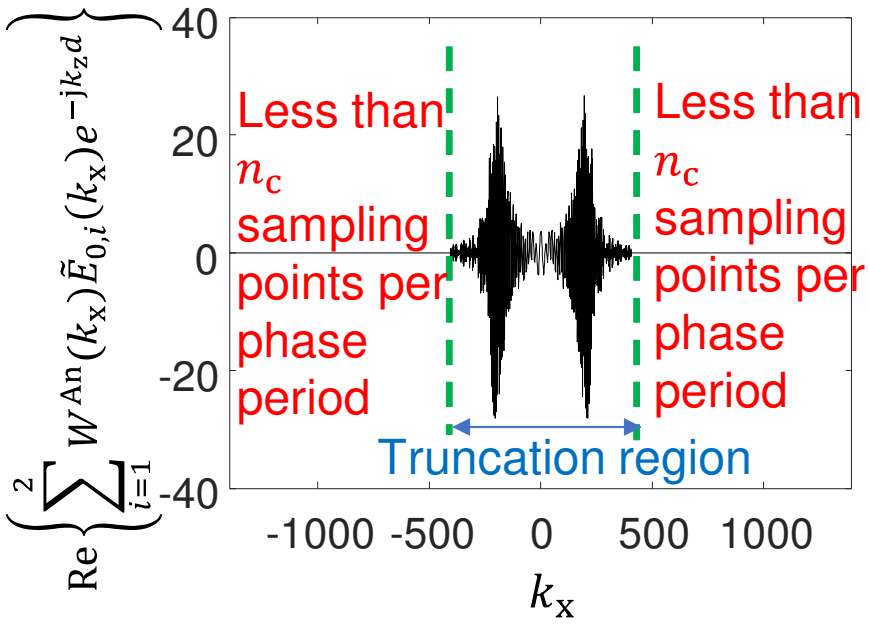

(b) After the windowing truncation.

Figure 4.5: The plot of the real part of $\sum_{i=1}^{2}\tilde{E}_{0,i}(k_x)e^{-jk_zd}$.

Chapter 5

Application of MKA for An Arbitrarily Shaped Object

5.1 Introduction

This chapter will extend MKA for an arbitrarily shaped object. The finding of the combination of windowing functions for the accuracy and computational cost will be introduced and explained. The proposed method will be simulated for a PEC elliptical cylinder in terms of the accuracy and computational cost. The accuracy of proposal will be validated by comparing with MoM as the reference. The computational cost of proposal will be compared with UTD. Evaluations and discussions will be done by varying the simulation parameters. The limitations and the future applicabilities will be discussed.

5.2 Extension of MKA for An Arbitrarily Shaped Object

This section introduce the application of MKA for an arbitrarily shaped object. The arbitrarily shaped cylinder is approximated to the combination of several rectangular cylinders as shown in Fig. 5.1. Those rectangular cylinders can be seen as the slices of the arbitrarily shaped cylinder by multiple planes as shown in Fig. 5.2. The accuracy of the above step approximation for an arbitrarily shaped object is validated by MoM, as shown in Appendix E. In Fig. 5.2, distances b and $c - Ld$ are large while d is small. There are $(L + 1)$ planes, and all the planes need to be perpendicular to Tx - Rx line [146]. The interval between two planes is determined by the maximum propagation angle θ_{m} [102] as (5.1).

$$d = \frac{\lambda}{\theta_{\mathrm{m}}^2} \tag{5.1}$$

By applying MKA repeatedly among those planes as (5.2), the scattered fields can be calculated for evaluating the shadowing gain.

$$E_{l+1,i}^{\mathrm{MKA}}(x) = E_{l+1,i}(x) - E_{l+1,i}(2w_{l+1,i} - x) \tag{5.2}$$

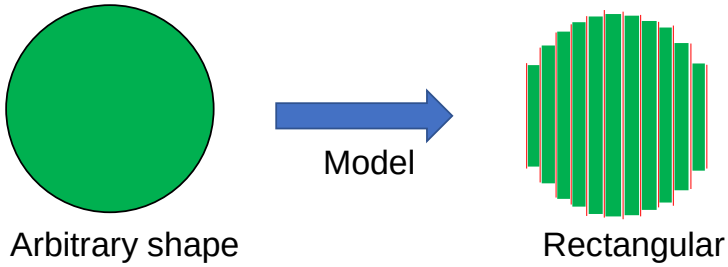

Figure 5.1: The modeling of the extended MKA.

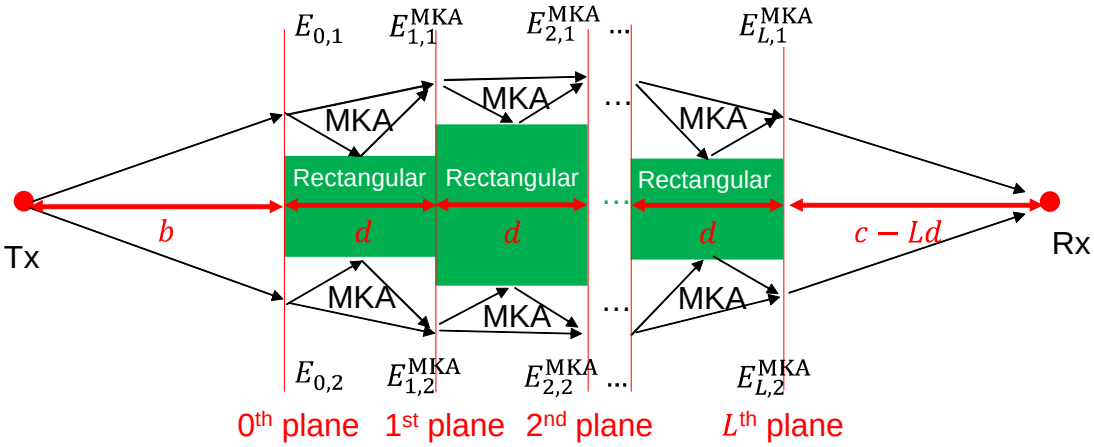

Figure 5.2: The extended MKA for the arbitrarily shaped object.

where $E_{l+1,i}^{\mathrm{MKA}}(\cdot)$ is the field calculated by MKA [144] in the $(l+1)^{\mathrm{th}}$ plane. $w_{l+1,i}$ is the coordinate of two edges in the $(l+1)^{\mathrm{th}}$ plane. The second term on the right-hand side is the mirror image. The fields $E_{l+1,i}^{\mathrm{MKA}}(\cdot)$ for the region $i = 1, 2$ are calculated separately, until they reach the last plane where two fields are merged.

The new finding is that, only the space domain of the zeroth plane and the angular spectrum domain of the last plane need their respective windowing functions, while other planes or domains do not. To prove the finding, there is a need to clarify what condition needs or does not need the windowing function. According to Chapter 4, the meaning of the windowing function is to truncate the region, where they cannot contribute to the integral. However, those regions have discretization errors caused by the equal sampling interval in a decreasing phase period. Thus, the constant phase period does not need a windowing function, and vice versa for the decreasing phase period. The author explains the characteristic of phase period for each plane in both domains as follows.

For the zeroth plane, the Hankel function in the space domain has a decreasing phase period according to key intuition P2. Thus, there is a need to take the spatial windowing function. However, since the change of the phase period in the small truncation region is insignificant, the phase period of the windowed Hankel function $E_{0,i}(x)$ is constant in the

truncation region. On the other hand, in the angular spectrum domain, $\tilde{E}_{0,i}(k_\mathrm{x})e^{-\mathrm{j}k_\mathrm{z}d}$ has a constant phase period according to key intuition P4. Since d is small, $\tilde{E}_{0,i}(k_\mathrm{x})$ has a constant phase period according to case C1. Thus, there is no need to take the angular spectrum windowing function.

For the first plane, since $\tilde{E}_{0,i}(k_\mathrm{x})$ dominates $\tilde{E}_{0,i}(k_\mathrm{x})e^{-\mathrm{j}k_\mathrm{z}d}$ according to case C1, $E_{1,i}(x)$ has almost the same constant phase period with $E_{0,i}(x)$ as (5.3). Thus, there is no need to take the spatial windowing function.

$$\begin{aligned}
&\arg\left(E_{1,i}(x)\right)\\
&=\arg\left(\mathcal{F}(\tilde{E}_{0,i}(k_\mathrm{x})e^{-\mathrm{j}k_\mathrm{z}d})\right) &\text{(5.3a)}\\
&\sim\arg\left(\mathcal{F}(\tilde{E}_{0,i}(k_\mathrm{x}))\right) &\text{(5.3b)}\\
&=\arg\left(W_{0,i}^{\mathrm{Sp}}(x)E_{0,i}(x)\right) &\text{(5.3c)}
\end{aligned}$$

where $\mathcal{F}(\cdot)$ and $\mathcal{F}^{-1}(\cdot)$ are FFT and IFFT, respectively. $\arg(\cdot)$ is the phase function.

Considering (5.3) as the initial condition, and repeating (5.4) and (5.5) inductively, the author proves that $E_{l+1,i}(x)$ and $\tilde{E}_{l+1,i}(k_\mathrm{x})e^{-\mathrm{j}k_\mathrm{z}d}$ have a constant phase period like $E_{0,i}(x)$ and $\tilde{E}_{0,i}(k_\mathrm{x})e^{-\mathrm{j}k_\mathrm{z}d}$, respectively. Thus, there is no need for the windowing function in both the space and angular spectrum domain until the last plane.

$$\begin{aligned}
&\arg\left(E_{l+1,i}(x)\right)\\
&=\arg\left(\mathcal{F}(\tilde{E}_{l,i}(k_\mathrm{x})e^{-\mathrm{j}k_\mathrm{z}d})\right) &\text{(5.4a)}\\
&\sim\arg\left(\mathcal{F}(\tilde{E}_{l,i}(k_\mathrm{x}))\right) &\text{(5.4b)}\\
&=\arg\left(E_{l,i}^{\mathrm{MKA}}(x)\right) &\text{(5.4c)}\\
&=\arg\left(E_{l,i}(x)-E_{l,i}(2w_{l,i}-x)\right) &\text{(5.4d)}
\end{aligned}$$

$$\begin{aligned}
&\arg\left(\tilde{E}_{l+1,i}(k_\mathrm{x})e^{-\mathrm{j}k_\mathrm{z}d}\right)\\
&\sim\arg\left(\tilde{E}_{l+1,i}(k_\mathrm{x})\right) &\text{(5.5a)}\\
&=\arg\left(\mathcal{F}^{-1}(E_{l+1,i}^{\mathrm{MKA}}(x))\right) &\text{(5.5b)}\\
&=\arg\left(\mathcal{F}^{-1}(E_{l+1,i}(x)-E_{l+1,i}(2w_{l+1,i}-x))\right) &\text{(5.5c)}\\
&=\arg\left((\tilde{E}_{l,i}(k_\mathrm{x})+\tilde{E}_{l,i}(-k_\mathrm{x})e^{\mathrm{j}2k_\mathrm{x}w_{l+1,i}})e^{-\mathrm{j}k_\mathrm{z}d}\right) &\text{(5.5d)}
\end{aligned}$$

Finally, for the last plane in the angular spectrum domain, since $e^{-\mathrm{j}k_\mathrm{z}(c-Ld)}$ dominates $\tilde{E}_{l,i}(k_\mathrm{x})e^{-\mathrm{j}k_\mathrm{z}(c-Ld)}$ for the large $c-Ld$, $\tilde{E}_{l,i}(k_\mathrm{x})e^{-\mathrm{j}k_\mathrm{z}(c-Ld)}$ has a decreasing phase period according to case C2. Thus, there is a need to take the angular spectrum windowing function.

Above all, we can conclude that only the space domain of the zeroth plane and the angular spectrum domain of the last plane need their separate windowing functions in case C2.

Since there is no windowing function in the space domain of the last plane, and the propagating distance from the last plane to Rx is a large value, X_4 in (4.14) should be considered to calculate the range of FFT. However, in the last plane, two terms of X_4 in (4.14) should be replaced. One is d should be replaced by $c - Ld$ since $c - Ld$ is the propagating distance in the last plane. Another is $w_{0,i}$ should be replaced by $w_{L,i}$ since $k_{\mathrm{x}} = kw_{L,i}/b$ corresponding to the direction of incident ray to the edge of object in the last plane becomes the pole in the angular spectrum domain. In addition, since there is a windowing function in the space domain of the zeroth plane, and the propagating distance from the zeroth plane to the first plane is a small value, X_1 in (4.14) should also be considered to calculate the range of FFT. For the planes between the zeroth and last, since there is no windowing function in the space domain, and the propagating distance between two planes is a small value, X_3 in (4.14) should also be considered to calculate the range of FFT. Therefore, for satisfying the above all, X and k_{w} are updated to X' and k'_{w} by (5.6) and (5.7), respectively.

$$X' = \max_{l\neq 0,L} \max_{i=1,2} \left(\frac{n_{\mathrm{s}}(c - Ld)|w_{L,i}|}{b + Ld}, n_{\mathrm{s}}a, n_{\mathrm{s}}|w_{l,i}| \right) \tag{5.6}$$

$$k'_{\mathrm{w}} = \frac{k_0 X'}{n_{\mathrm{c}}(c - Ld)} \tag{5.7}$$

Figure 5.3 shows the flow chart of MKA calculation. The green block corresponds to the proposal of the designed parameters. The red remarks are the findings of the windowing functions. The order of the calculation time for MKA with the proposed parameters is (5.8).

$$t^{\mathrm{MKA}} \sim O\left(LN \log_2 N\right) \tag{5.8}$$

where $N = X_\alpha/\Delta x'$. t^{MKA} is the computational cost of MKA. The detailed computational complexity is shown in Appendix D.

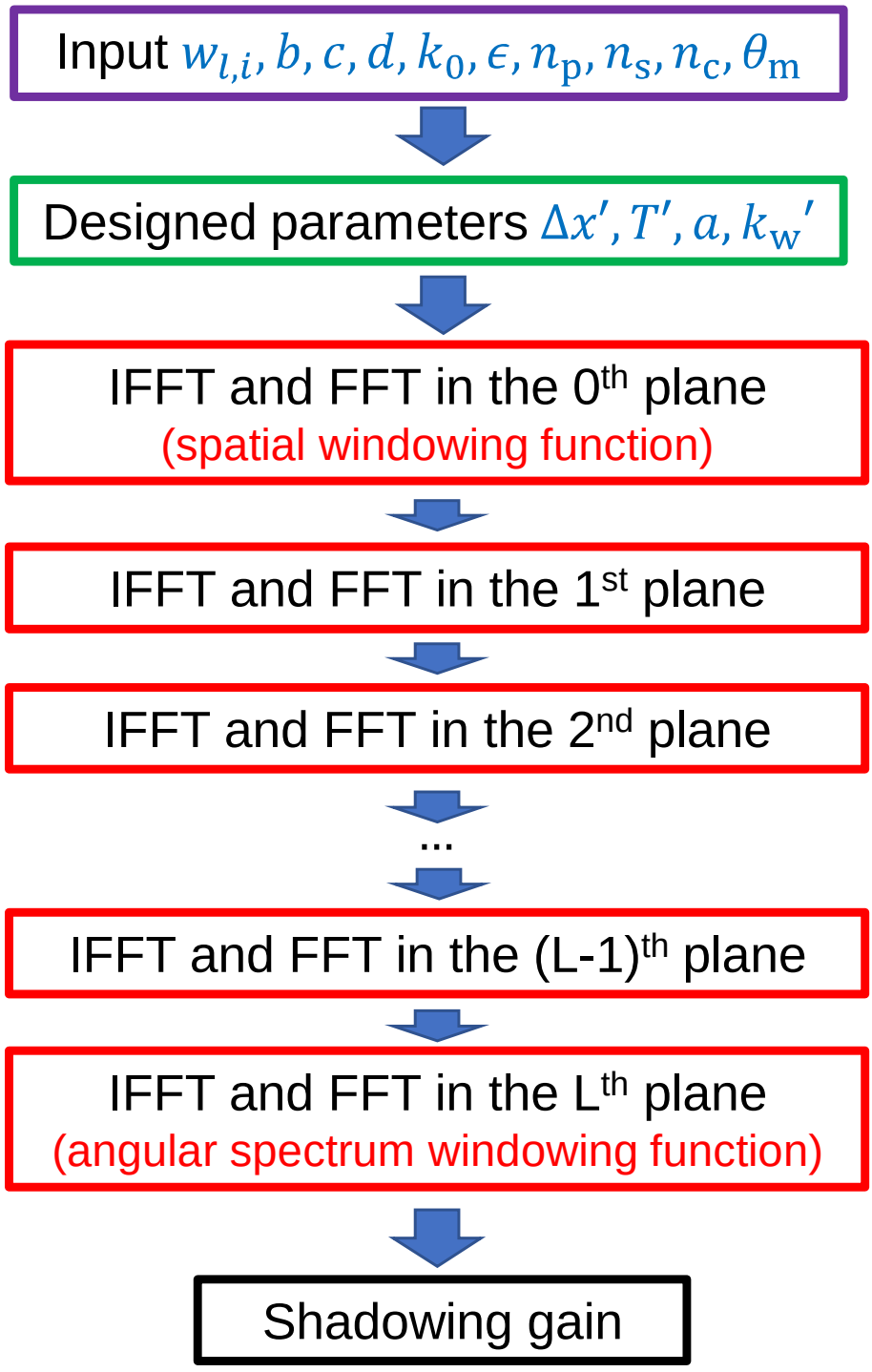

Figure 5.3: Flow chart of MKA calculation.

5.3 Simulations for An Arbitrarily Shaped Cylinder

This section introduces simulation for an arbitrarily shaped cylinder by applying MKA with the designed FFT parameters mentioned in Chapter 4 and the combination of the windowing functions mentioned in this Chapter. Simulation scenarios are explained in Subsection 5.3.1. Simulation results are shown in Subsection 5.3.2. Evaluations and discussions are shown in Subsection 5.3.3.

5.3.1 Simulation Scenarios

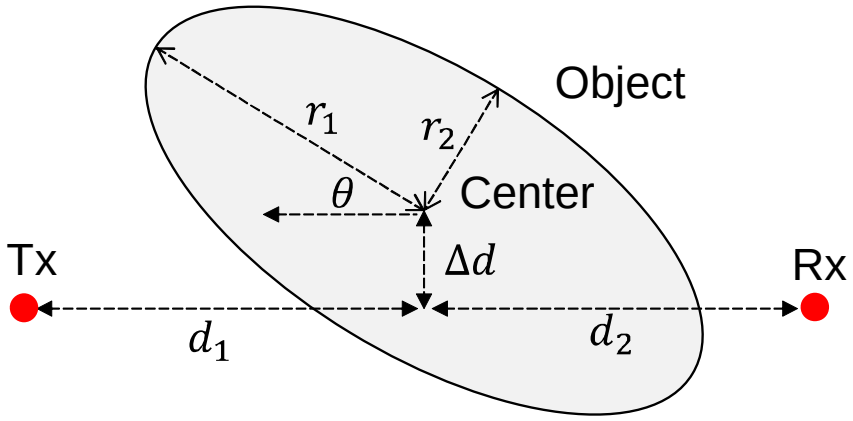

Figure 5.4: Simulation environment in x-z domain.

The author validates the proposed method for an elliptical conductor cylinder, which models the cross section of human body. As shown in Fig. 5.4, an elliptical conductor cylinder is placed between Tx and Rx. An electric line source with the cylindrical wave in the perpendicular polarization is considered at mmWave. r_1 and r_2 denote the semi-major and semi-minor axes of the ellipse, respectively. f denotes the frequency. d_1 denotes the horizontal distance between the center of the ellipse and Tx. d_2 denotes the horizontal distance between the center of the ellipse and Rx. Δd denotes the offset between the center of the ellipse and Tx-Rx line. θ denotes the rotation angle of the ellipse.

There are two simulation scenarios. Scenario 1 varies Δd from -100λ to 100λ with an interval of 0.5λ. Scenario 2 varies f from 17 GHz to 66.5 GHz with an interval of 0.5 GHz at $\Delta d = 0$ m. Considering the human-size shadowing problem, the author sets the parameters of each scenario as shown in Table 5.1 and Table 5.2, respectively. For each scenario, three rotation angles are considered, i.e., $\theta = 0°$, $\theta = 45°$, and $\theta = 90°$.

The processor of the calculating computer is an Intel(R) Core(TM) i7-8750H CPU @ 2.20 GHz. The usable installed memory of the calculating computer is 15.8 GB. The system type of the calculating computer is 64-bit operating system with a x64-based processor. The simulation software is MATLAB.

Table 5.1: Parameters of Scenario 1

Parameters	**Values**
θ (°)	0, 45, 90
θ_{m} (°)	30, 45, 45
r_1 (λ)	50
r_2 (λ)	20
d_1 (λ)	444.4
d_2 (λ)	1777.8
Δd (λ)	$-100 : 0.5 : 100$
n_{p}	7
n_{s}	10
n_{c}	2
ϵ	10^{-6}

Table 5.2: Parameters of Scenario 2

Parameters	**Values**
f (GHz)	$17 : 0.5 : 66.5$
θ (°)	0, 45, 90
θ_{m} (°)	30, 45, 45
r_1 (m)	0.25
r_2 (m)	0.1
d_1 (m)	2
d_2 (m)	8
Δd (m)	0
n_{p}	7
n_{s}	10
n_{c}	2
ϵ	10^{-6}

Computation time of MKA is compared with that of UTD. To discuss the calculation time later, the author gives the detailed UTD simulation approaches in Chapter 2.

MoM using EFIE as the reference of accuracy is simulated. The piecewise constant function is selected as the basis function of MoM and point matching method is implemented. The mesh size of MoM is set to $\lambda/10$ for accuracy. The author gives the detailed MoM simulation approaches in Chapter 2.

5.3.2 Simulation Results

For scenario 1, the shadowing gain results of UTD, MKA and MoM were shown in Fig. 5.5. The horizontal axis was Δd (λ). The vertical axis was the shadowing gain results in decibel (dB) scale. The results show that the accuracy of the proposal is validated by comparing with MoM for varying the location of the object.

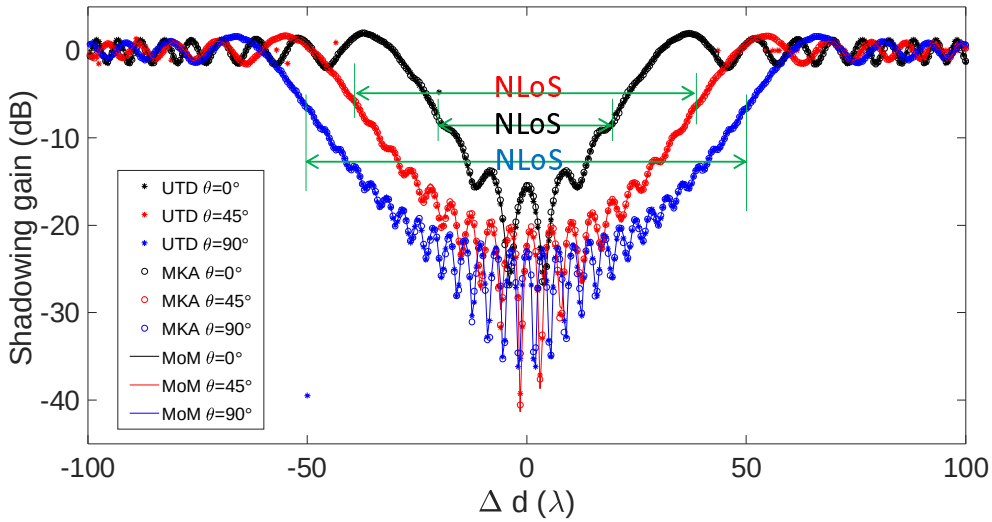

Figure 5.5: The plots of the shadowing gain for scenario 1.

The relative calculation time of MKA was shown in Fig. 5.6. The horizontal axis was Δd (λ). The vertical axis was the relative calculation time referenced by UTD. The improvement of calculation time was compared with UTD for varying the location of the object.

For scenario 2, the shadowing gain results of UTD, MKA and MoM were shown in Fig. 5.7. The horizontal axis was f (GHz). The vertical axis was the shadowing gain results in dB scale. The results show that the accuracy of the proposal is validated by comparing with MoM for varying the frequencies.

The relative calculation time of MKA was shown in Fig. 5.8. The horizontal axis was f (GHz). The vertical axis was the relative calculation time. The improvement of calculation time was compared with UTD for varying the frequencies.

Considering the MoM as the reference, the author calculated the root-mean-square error (RMSE) by (5.9).

$$\mathrm{RMSE} = \sqrt{\sum_{j=1}^{m} \frac{\left(\mathrm{SG}_j^{\mathrm{Method}} - \mathrm{SG}_j^{\mathrm{MoM}}\right)^2}{m}} \tag{5.9}$$

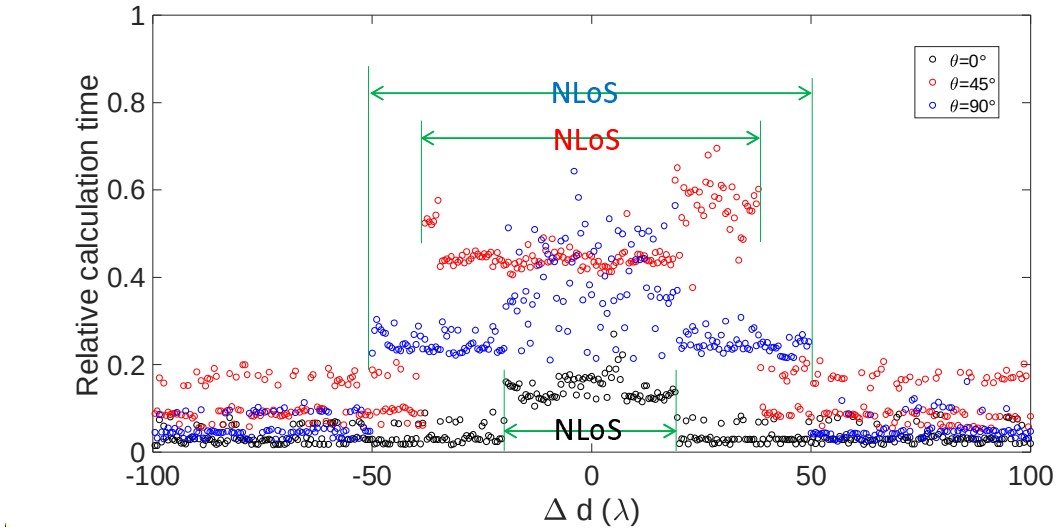

Figure 5.6: The plots of the relative calculation time for scenario 1.

Table 5.3: Comparison of UTD and MKA for scenario 1

Methods	RMSE (dB)	Computational time (ms)
UTD ($\theta = 0°$)	0.25	94.9 – 3179.5
MKA ($\theta = 0°$)	0.22	12.9 – 63.1
UTD ($\theta = 45°$)	0.46	94.7 – 912.9
MKA ($\theta = 45°$)	0.25	42.5 – 76.4
UTD ($\theta = 90°$)	1.65	93.6 – 915.9
MKA ($\theta = 90°$)	0.32	21.6 – 70.6

where $\mathrm{SG}_j^{\mathrm{MoM}}$ is the shadowing gain calculated by MoM in dB scale for the j^{th} test, $\mathrm{SG}_j^{\mathrm{Method}}$ is the shadowing gain calculated by UTD or MKA in dB scale for the j^{th} test. m is the total number of tests.

The comparisons of the RMSE and the computational time between UTD and MKA for each scenario were shown in Table 5.3 and Table 5.4, respectively.

The results showed that the proposed low computational cost MKA presented good accuracy with a low RMSE of less than 0.5 dB by comparing with the MoM as the reference.

The author evaluated the dominant parts of the calculation time for UTD and MKA as follows. For the LoS case of $f = 66.5$ GHz, $\theta = 0°, \Delta d = 50\lambda$, there were one reflection ray and one incident ray for UTD calculation. UTD took 446.6 ms in (2.17) for reflection point searching and 17.9 ms in (2.22) for one modified Fresnel integral, while MKA took 16.8 ms for the entire calculation. For the NLoS case of $f = 66.5$ GHz, $\theta = 0°, \Delta d = 0$ m, there were two creeping diffraction rays for UTD calculation. UTD took 34.7 ms in (2.9) for two incomplete elliptic integrals of the second kind, 38.4 ms in (2.13) for two incomplete elliptic integrals of the first kind, and 32.7 ms in (2.15) for two modified Fresnel integrals,

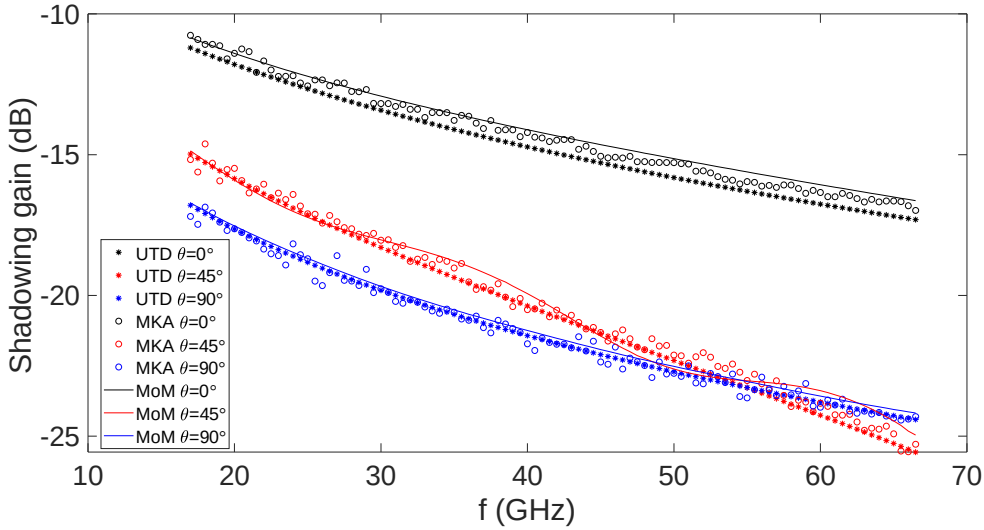

Figure 5.7: The plots of the shadowing gain for scenario 2.

Table 5.4: Comparison of UTD and MKA for scenario 2

Methods	RMSE (dB)	Computational time (ms)
UTD ($\theta = 0°$)	0.59	104.5 – 199.3
MKA ($\theta = 0°$)	0.25	2.2 – 47.9
UTD ($\theta = 45°$)	0.46	103.5 – 116.1
MKA ($\theta = 45°$)	0.44	6.0 – 74.7
UTD ($\theta = 90°$)	0.18	104.5 – 120.1
MKA ($\theta = 90°$)	0.31	3.4 – 45.9

while MKA took 19.6 ms for the entire calculation. The calculation time of the proposal was improved by 1.4 – 67.2 times compared with the UTD using the special functions and reflection point searching.

The memories for MKA and UTD were also compared. UTD took 138 – 197 MB for one test, while MKA took 30 – 47 MB for one test. The MATLAB code of MKA was shown in Appendix F.

5.3.3 Evaluations and Discussions

This subsection varied the parameters of ϵ, θ_{m}, n_{s}, n_{c}, and n_{p} to evaluate the accuracy and computational cost by using RMSE and the mean values of the relative computational time, respectively.

Firstly, the values of ϵ were varied from 10^{-1} to 10^{-10}. The other parameters were fixed as $\theta_{\mathrm{m}} = 30°, 45°, 45°$ for $\theta = 0°, 45°, 90°$, $n_{\mathrm{s}} = 10$, $n_{\mathrm{c}} = 2$, and $n_{\mathrm{p}} = 7$, respectively. The results were shown in Fig. 5.9 - Fig. 5.12 for RMSE and the mean values of the relative computational time in scenarios 1 and 2, respectively. From results, we found that ϵ with

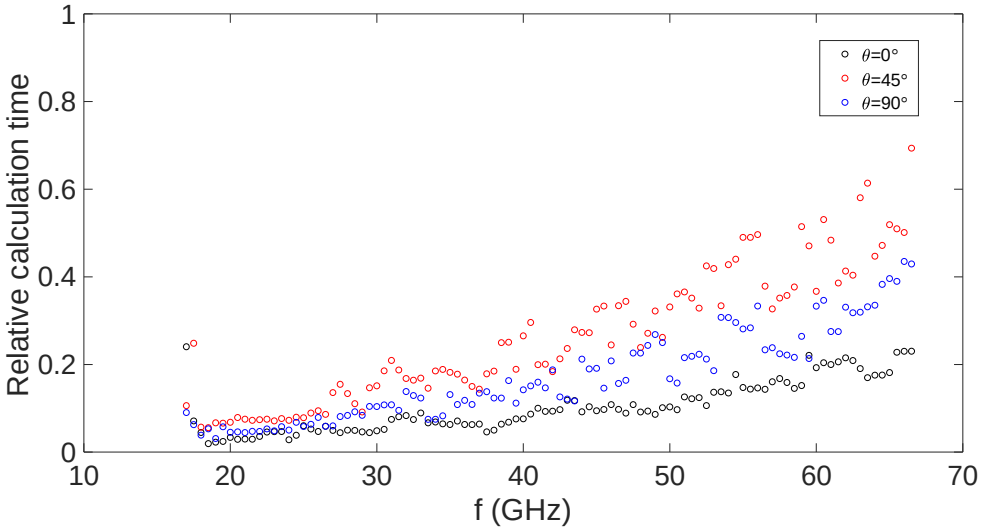

Figure 5.8: The plots of the relative calculation time for scenario 2.

the values smaller than 10^{-5} could provide low and converge RMSE with the values less than 0.5 dB. In addition, the computational time became higher with the decrease of ϵ since FFT size became larger. Thus, the author chose $\epsilon = 10^{-6}$ for considering the balance between the computational cost and accuracy.

Secondly, the values of θ_{m} were varied from 15° to 45°. The other parameters were fixed as $\epsilon = 10^{-6}$, $n_{\mathrm{s}} = 10$, $n_{\mathrm{c}} = 2$, and $n_{\mathrm{p}} = 7$, respectively. The reasons for selecting only $\theta_{\mathrm{m}} = 15°$, $\theta_{\mathrm{m}} = 30°$, and $\theta_{\mathrm{m}} = 45°$ were discussed in Appendix C. The results were shown in Fig. 5.13 - Fig. 5.16 for RMSE and the mean values of the relative computational time in scenarios 1 and 2, respectively. From results, we found that, for $\theta = 0°$, $\theta_{\mathrm{m}} = 30°, 45°$ could provide RMSE less than 0.5 dB, and for $\theta = 45°, 90°$, $\theta_{\mathrm{m}} = 45°$ could provide RMSE less than 0.5 dB. In addition, the computational time became higher with the increase of θ_{m} since the planes number became more. Thus, the author chose $\theta_{\mathrm{m}} = 30°, 45°, 45°$ for $\theta = 0°, 45°, 90°$, respectively. The reason for using different θ_{m} was considered that ellipses with respective θ had the different mean value of the slope. The detailed calculations of the mean value of the slope were also shown in Appendix C.

Thirdly, the values of n_{s} were varied from 5 to 20. The other parameters were fixed as $\epsilon = 10^{-6}$, $\theta_{\mathrm{m}} = 30°, 45°, 45°$ for $\theta = 0°, 45°, 90°$, $n_{\mathrm{c}} = 2$, and $n_{\mathrm{p}} = 7$, respectively. The results were shown in Fig. 5.17 - Fig. 5.20 for RMSE and the mean values of the relative computational time in scenarios 1 and 2, respectively. From results, we found that $n_{\mathrm{s}} = 10$ could provide the lowest RMSE. The reason why RMSE with $n_{\mathrm{s}} = 20$ was higher than it with $n_{\mathrm{s}} = 10$ was considered as follows. According to the proof in Appendix B, the transition regions B and D in Fig. B.1 with $n_{\mathrm{s}} = 20$ were larger than the transition regions but with $n_{\mathrm{s}} = 10$ for a fixed n_{c}. The discretization error became larger due to inaccurately integrate those larger transition regions, where insufficiently sampled regions with less than ten points per phase period existed. The increase of the discretization error resulted a higher RMSE for $n_{\mathrm{s}} = 20$, compared with $n_{\mathrm{s}} = 10$. In addition, the computational time became higher

with the increase of n_s since the range of FFT became larger.

Fourthly, the values of n_c were varied from 2 to 10. The other parameters were fixed as $\epsilon = 10^{-6}$, $\theta_m = 30°, 45°, 45°$ for $\theta = 0°, 45°, 90°$, $n_s = 10$, and $n_p = 7$, respectively. The results were shown in Fig. 5.21 - Fig. 5.24 for RMSE and the mean values of the relative computational time in scenarios 1 and 2, respectively. From results, we found that $n_c = 2$ could provide the lowest RMSE. The reason was also related to Appendix B. According to the proof in Appendix B, the peaks with the heights less than n_c/n_s of the highest peak were truncated. For a fixed n_s, the increase of n_c would cause more peaks vanished. Those vanished peaks with the higher heights would influence the accuracy of the next FT. The increase of the truncation error resulted a higher RMSE for a larger n_c. In addition, the computational time almost did not change with the increase of n_c since their ranges of FFT were the same for a fixed n_s.

Fifthly, the pairs of (n_s, n_c) were varied from $(1, 5)$ to $(4, 20)$, which always satisfied $n_s = 5n_c$. The other parameters were fixed as $\epsilon = 10^{-6}$, $\theta_m = 30°, 45°, 45°$ for $\theta = 0°, 45°, 90°$, and $n_p = 7$, respectively. The results were shown in Fig. 5.25 - Fig. 5.28 for RMSE and the mean values of the relative computational time in scenarios 1 and 2, respectively. From results, we found that $n_s = 5n_c$ presented a better accuracy by comparing with only fixing either n_s or n_c. The reason was considered that $n_s = 5n_c$ could provide a good balance between the discretization and truncation error. However, the computational time became larger with the increase of n_s since the range of FFT became larger. Therefore, the pair of (n_s, n_c) was proposed as $(2, 10)$ for accuracy and computational cost.

Sixthly, the values of n_p were varied from 1 to 10. The other parameters were fixed as $\epsilon = 10^{-6}$, $\theta_m = 30°, 45°, 45°$ for $\theta = 0°, 45°, 90°$, $n_s = 10$, and $n_c = 2$, respectively. The results were shown in Fig. 5.29 - Fig. 5.32 for RMSE and the mean values of the relative computational time in scenarios 1 and 2, respectively. From results, we found that RMSE did not change for varying n_p with the small values. The reason was related to Appendix A. According to (A.6) in Appendix A, for n_p with a small value, Δx dominated the $\Delta x'$ and was n_p-independent. Therefore, RMSE did not change for varying n_p with the small values.

Finally, the values of n_p were varied from 17 to 107. The other parameters were fixed as $\epsilon = 10^{-6}$, $\theta_m = 30°, 45°, 45°$ for $\theta = 0°, 45°, 90°$, $n_s = 10$, and $n_c = 2$, respectively. The results were shown in Fig. 5.33 - Fig. 5.36 for RMSE and the mean values of the relative computational time in scenarios 1 and 2, respectively. From results, we found that RMSE changed for varying n_p with the large values. The reason was also related to Appendix A. According to (A.6) in Appendix A, for n_p with a large value, Δx_i dominated the $\Delta x'$ and was n_p-dependent. We found that the values of n_p from 7 to 57 provided a low RMSE less than 0.5 dB. That was because for large n_p, windowing size in space domain would become larger, and hence more discretization error would be inaccurately integrated. Moreover, the computational time became larger with the increase of n_p since $\Delta x'$ became smaller. Therefore, we chose $n_p = 7$ for considering the accuracy and computational cost.

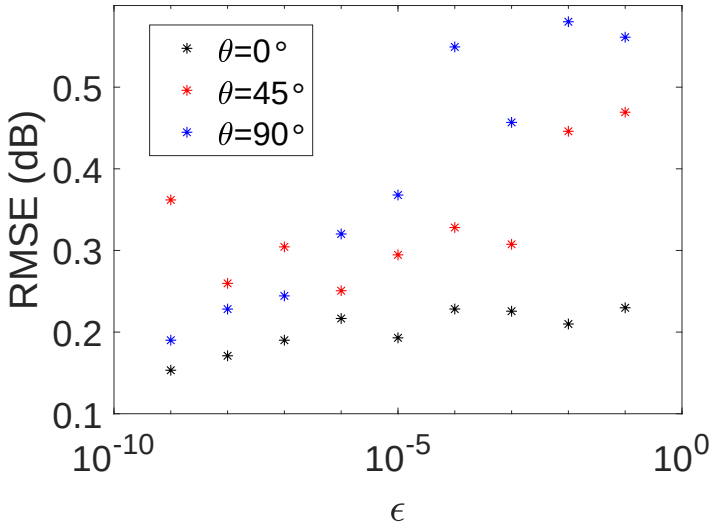

Figure 5.9: The relations between RMSE and ϵ for scenario 1.

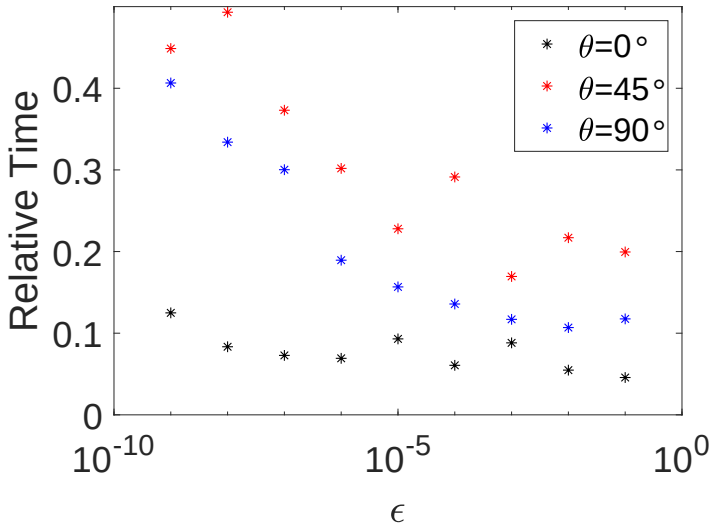

Figure 5.10: The relations between the mean values of the relative computational time and ϵ for scenario 1.

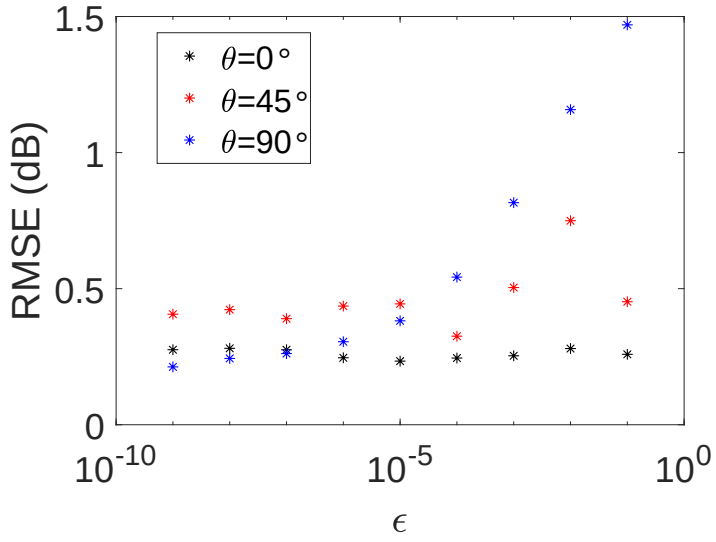

Figure 5.11: The relations between RMSE and ϵ for scenario 2.

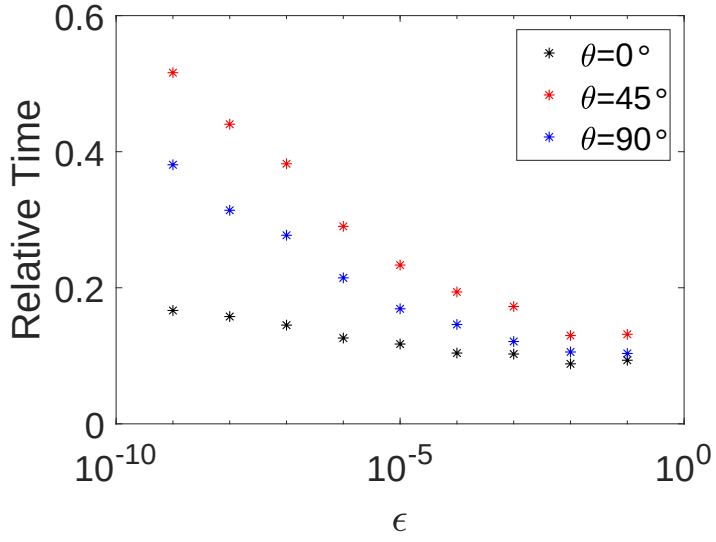

Figure 5.12: The relations between the mean values of the relative computational time and ϵ for scenario 2.

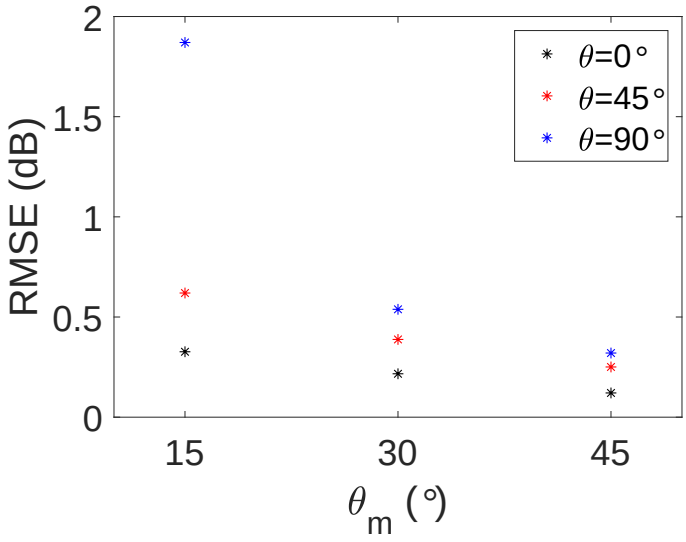

Figure 5.13: The relations between RMSE and θ_m for scenario 1.

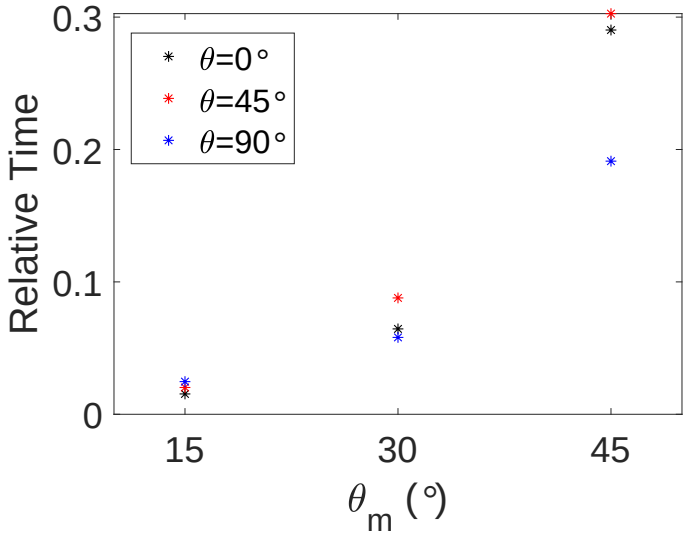

Figure 5.14: The relations between the mean values of the relative computational time and θ_m for scenario 1.

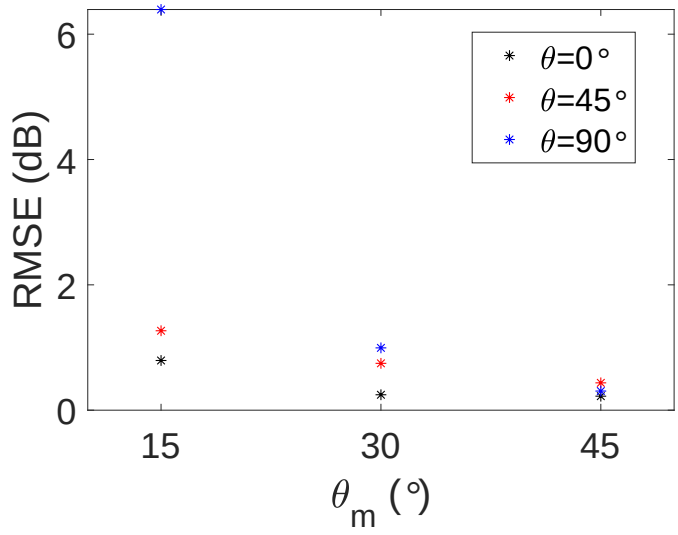

Figure 5.15: The relations between RMSE and θ_m for scenario 2.

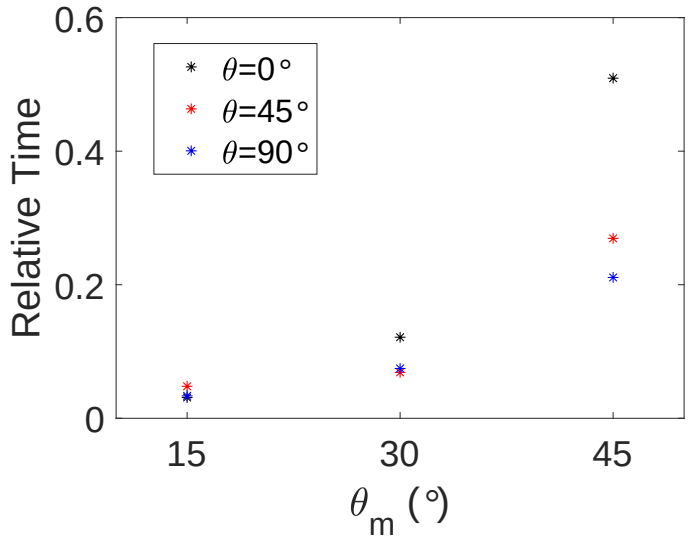

Figure 5.16: The relations between the mean values of the relative computational time and θ_m for scenario 2.

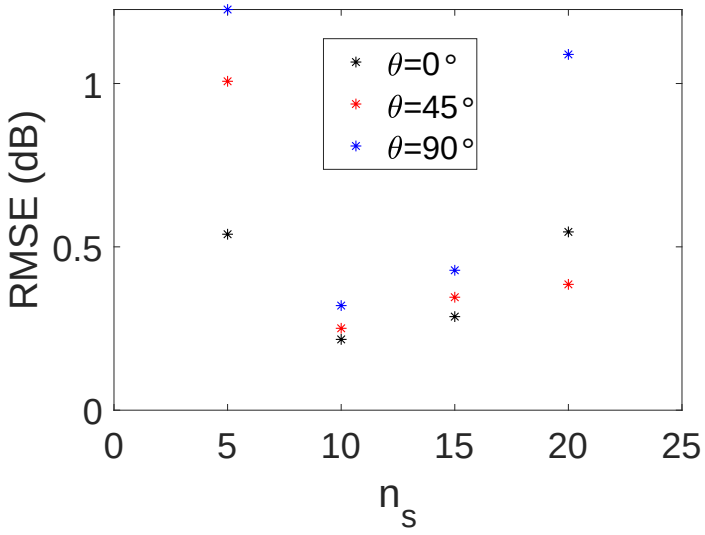

Figure 5.17: The relations between RMSE and n_s for scenario 1.

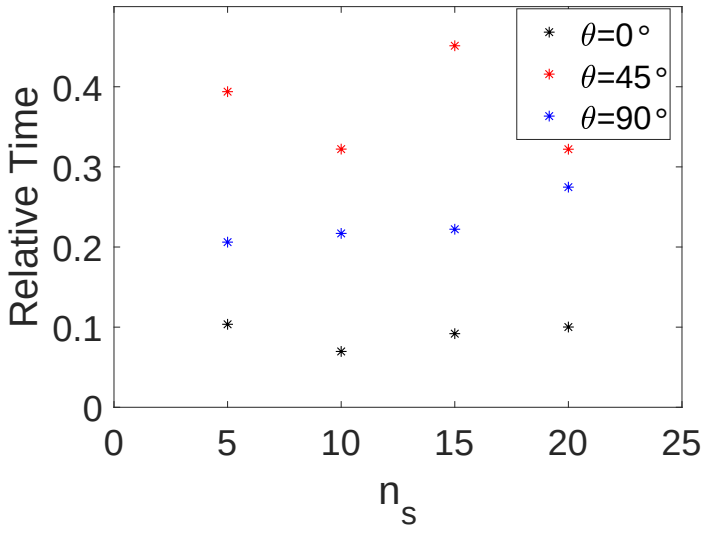

Figure 5.18: The relations between the mean values of the relative computational time and n_s for scenario 1.

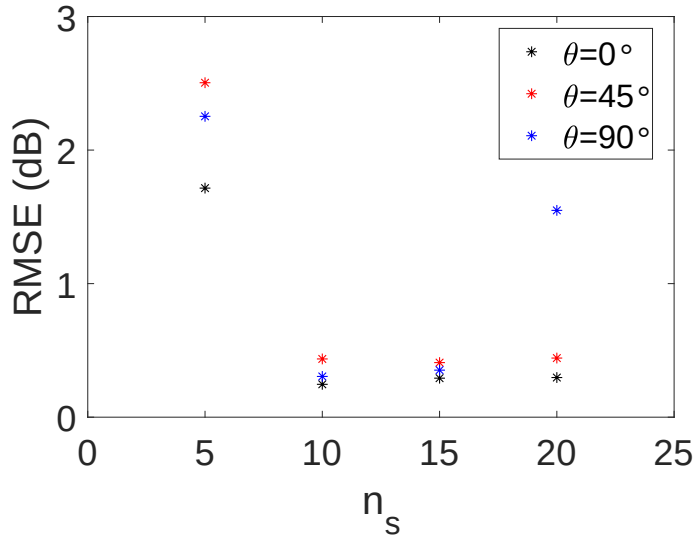

Figure 5.19: The relations between RMSE and n_s for scenario 2.

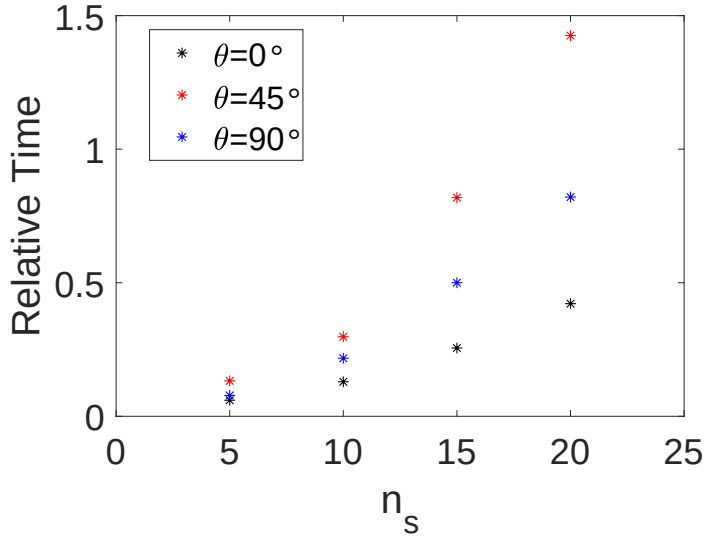

Figure 5.20: The relations between the mean values of the relative computational time and n_s for scenario 2.

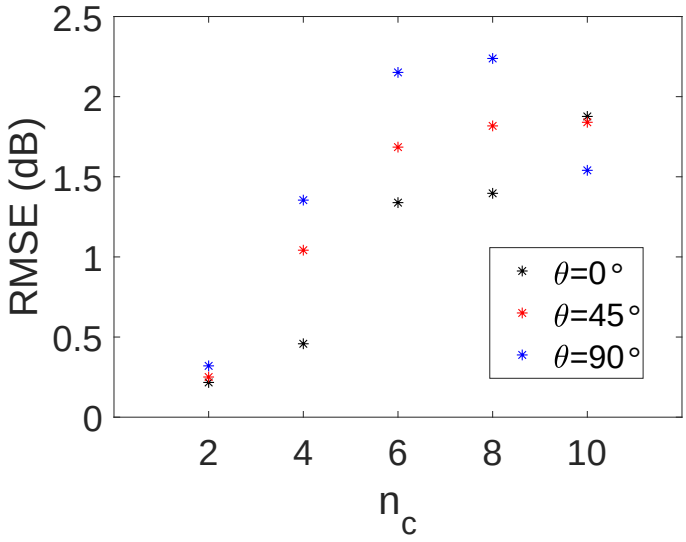

Figure 5.21: The relations between RMSE and n_c for scenario 1.

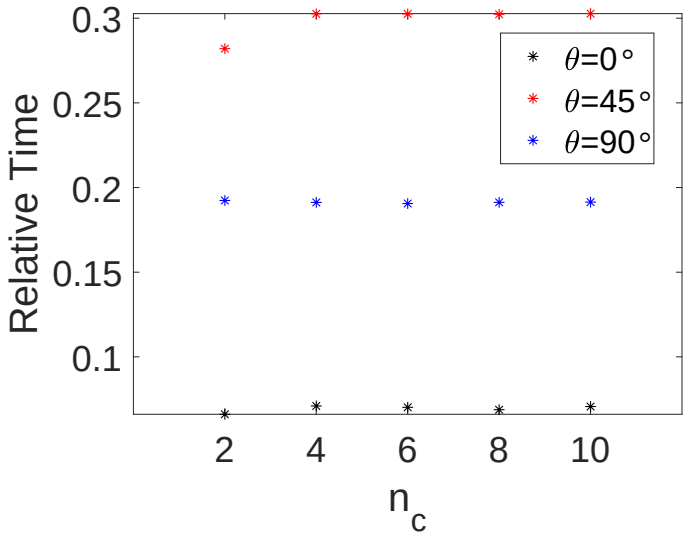

Figure 5.22: The relations between the mean values of the relative computational time and n_c for scenario 1.

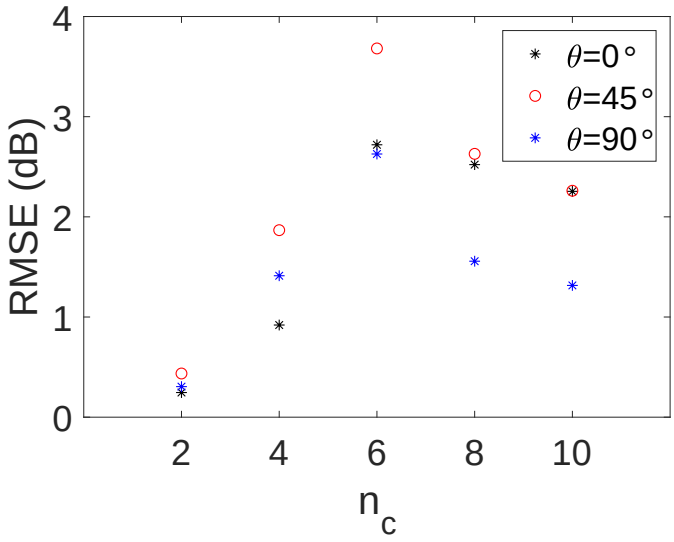

Figure 5.23: The relations between RMSE and n_c for scenario 2.

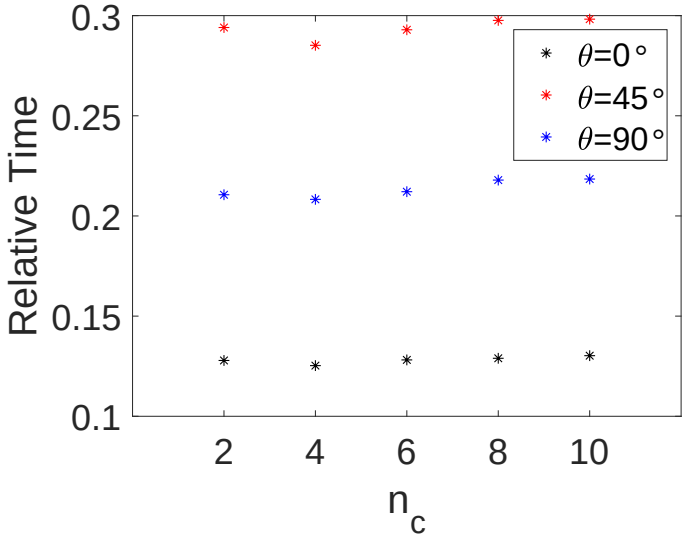

Figure 5.24: The relations between the mean values of the relative computational time and n_c for scenario 2.

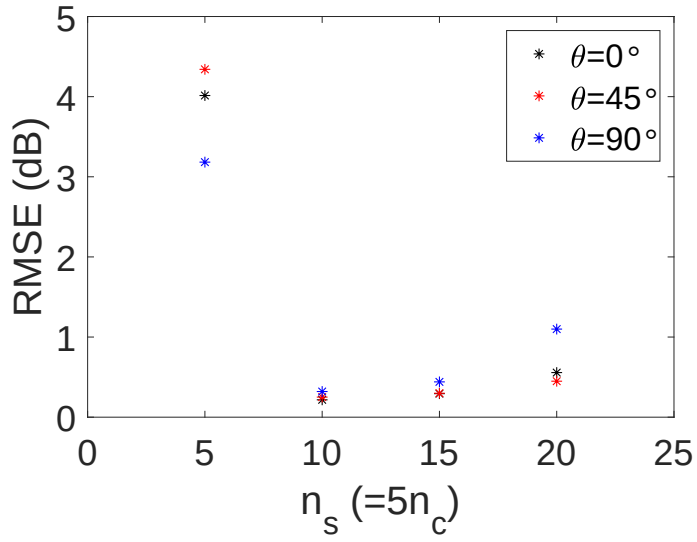

Figure 5.25: The relations between RMSE and $n_{\mathrm{s}} = 5n_{\mathrm{c}}$ for scenario 1.

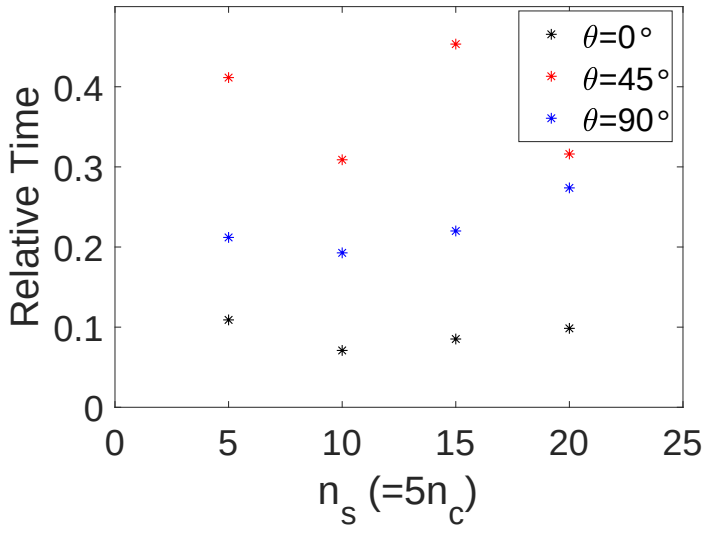

Figure 5.26: The relations between the mean values of the relative computational time and $n_{\mathrm{s}} = 5n_{\mathrm{c}}$ for scenario 1.

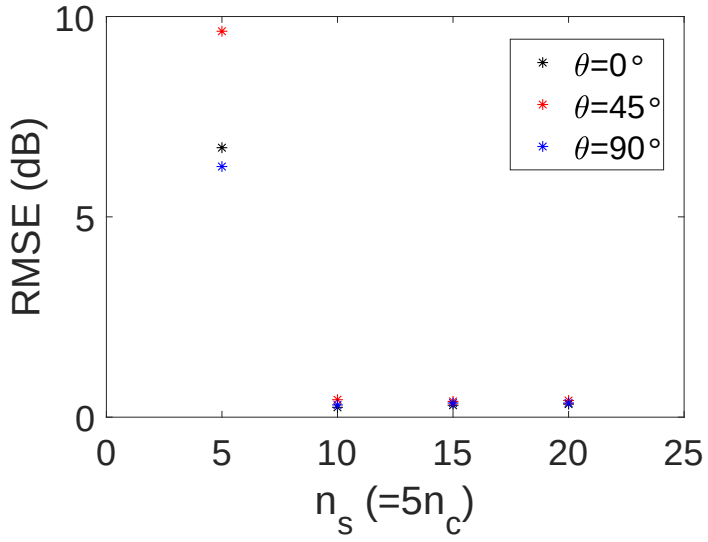

Figure 5.27: The relations between RMSE and $n_s = 5n_c$ for scenario 2.

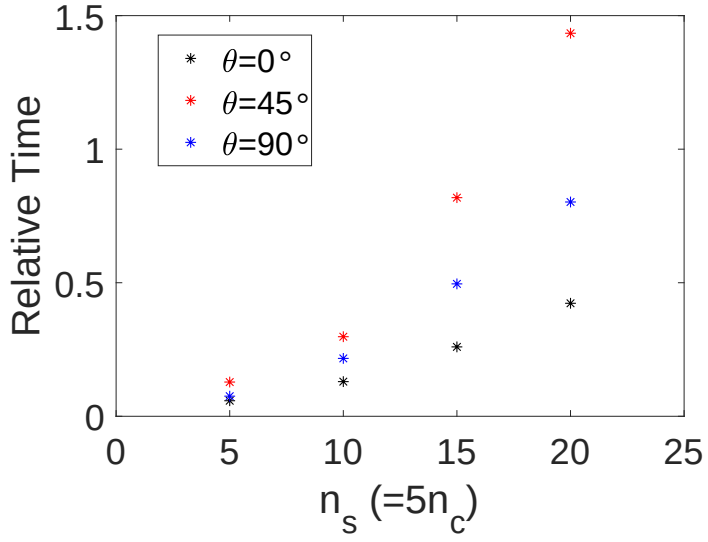

Figure 5.28: The relations between the mean values of the relative computational time and $n_s = 5n_c$ for scenario 2.

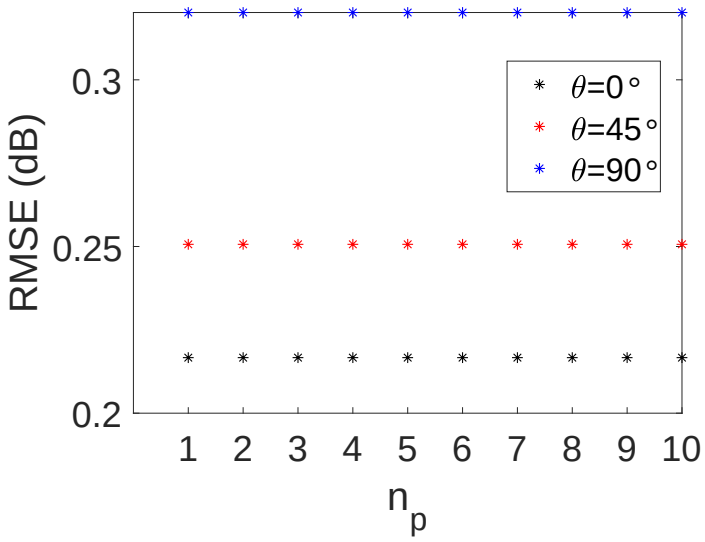

Figure 5.29: The relations between RMSE and small n_{p} for scenario 1.

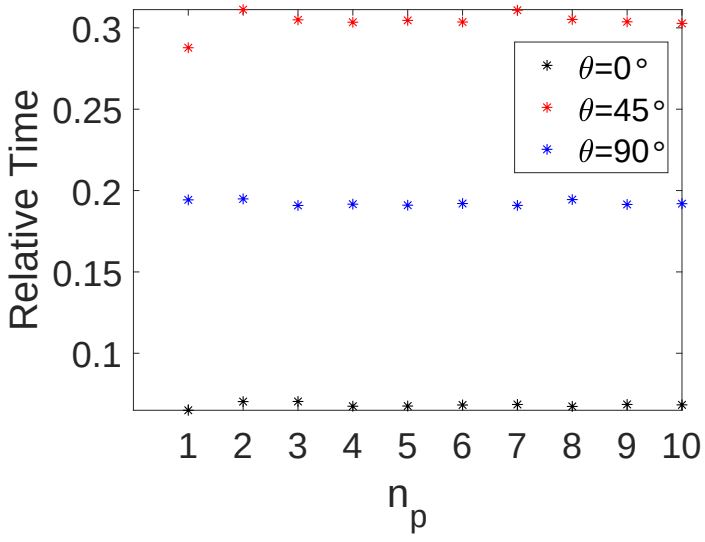

Figure 5.30: The relations between the mean values of the relative computational time and small n_{p} for scenario 1.

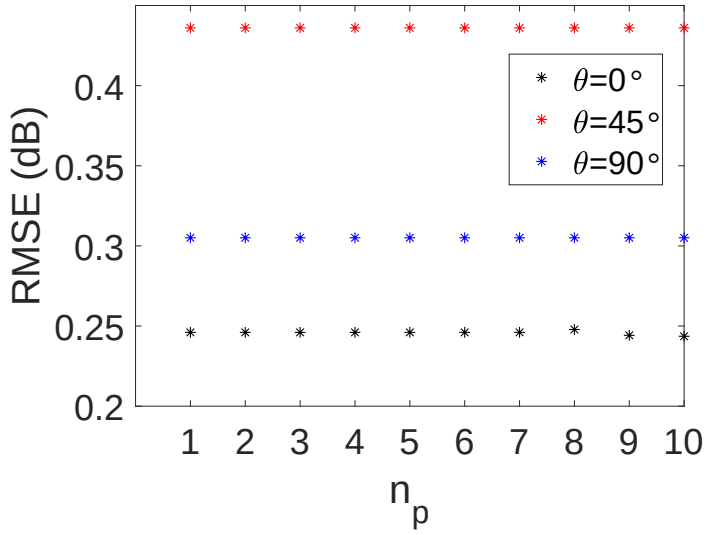

Figure 5.31: The relations between RMSE and small n_{p} for scenario 2.

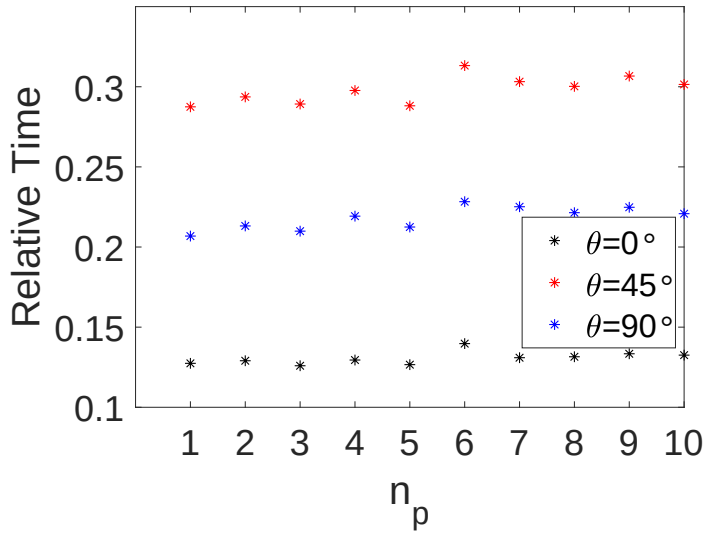

Figure 5.32: The relations between the mean values of the relative computational time and small n_{p} for scenario 2.

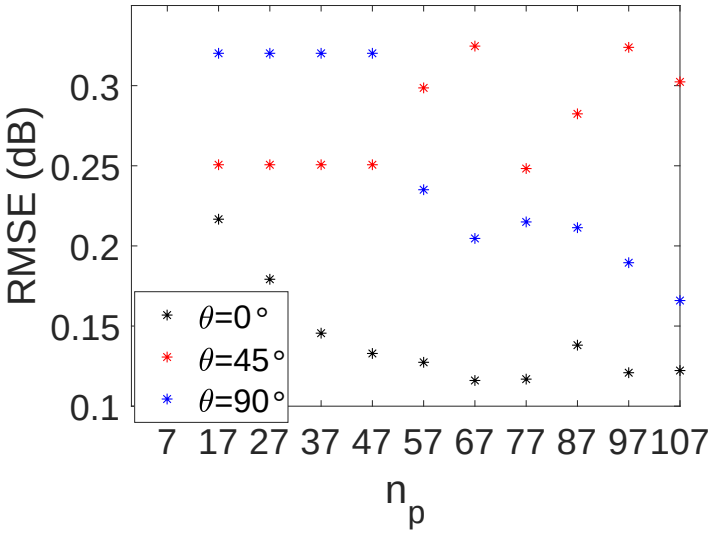

Figure 5.33: The relations between RMSE and large n_{p} for scenario 1.

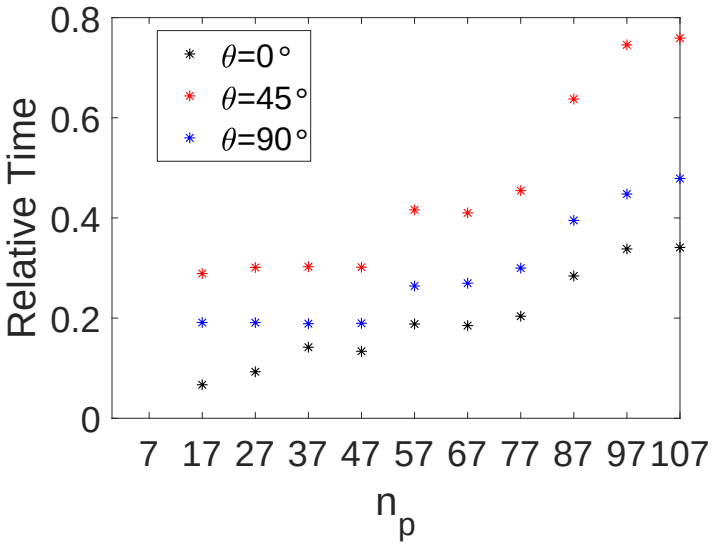

Figure 5.34: The relations between the mean values of the relative computational time and large n_{p} for scenario 1.

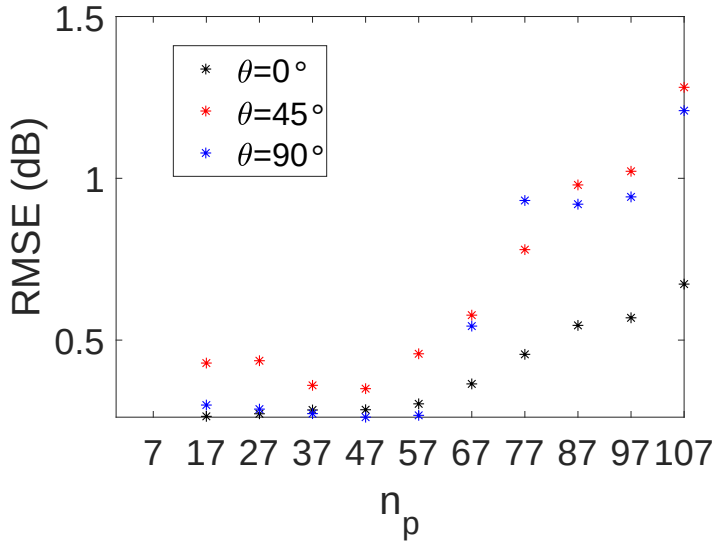

Figure 5.35: The relations between RMSE and large n_{p} for scenario 2.

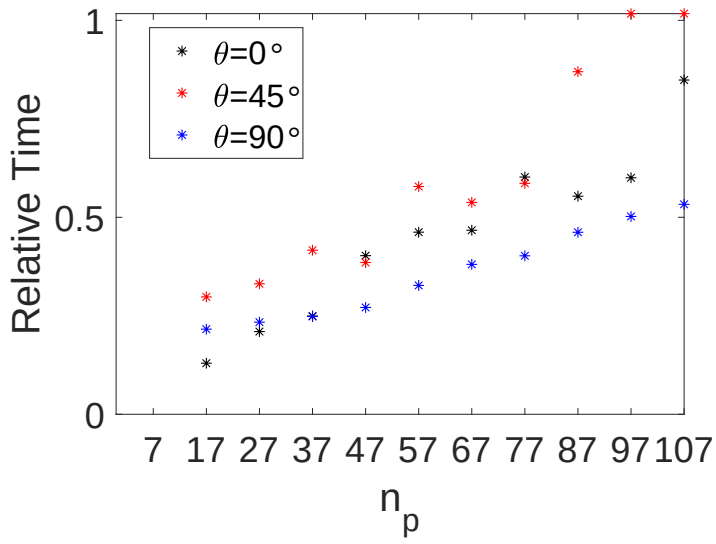

Figure 5.36: The relations between the mean values of the relative computational time and large n_{p} for scenario 2.

5.4 Limitations and Future Applicabilities

This section discusses the limitations and future applicabilities of MKA.

As a limitation of this study, MKA can only deal with a convex PEC object, which should be put between Tx and Rx. Current MKA can not account for the internal reflections of a concave object and the external reflections between two or more objects. In addition, this work is only applied to forward scattering problems, and hence object should be put between Tx and Rx. Although some opaque objects, which can be approximated as PEC, may apply this technique, transparent objects with the transmission such as trees cannot use it.

For applicability in the future, the proposal can be utilized to predict a large number of shielding patterns under various conditions at a high speed in 5G communication system. Conventionally, when the measured value of shadowing gain expires, MIMO is used to search for other beams and the propagation path is switched [150]. However, we want to switch at an earlier time to ensure stable communication. By using the results of this research, a large number of the shadowing patterns varying the size, angle, and location of an object can be simulated at a high speed. Through training these patterns as big data by machine learning, when the measured value of shadowing gain starts to drop, the following shadowing pattern can be predicted. The other beam can be switched before the measured value of shadowing gain expires, which can make stable communication possible [151]. Considering a scenario in which an obstacle is moving between user and base station and blocking the signal, MKA can predict a large number of the shadowing patterns to contribute to a faster beam switching of MIMO for stable mobile communication.

Appendix D shows the comparison between current methods and the proposal. From Appendix D, we can find that MKA can achieve a lower computational memory compared with other numerical methods. In addition, MKA can provide a better predicting accuracy compared with the analytic methods for an arbitrarily shaped object. Moreover, for a rectangular shaped object, MKA can achieve a faster computational time compared with other numerical methods.

5.5 Conclusion

The applicable range of proposal was extended to an arbitrarily shaped cylinder by multiple planes. This work found that, only the space domain of the zeroth plane and the angular spectrum domain of the last plane needed their separate windowing functions for accuracy and computational cost. The details of those windowing functions were introduced, and their necessities were explained. The author validated the proposed method for an PEC elliptical cylinder. Simulations by changing the object's location, direction, and frequencies were conducted. The results showed that the proposed method presents good accuracy with a low RMSE of less than 0.5 dB, compared with the MoM as the reference. Furthermore, the calculation time was improved by 1.4 – 67.2 times compared with the UTD. Objective 2 has been achieved.

Chapter 6

Conclusion

6.1 Summary

This study proposed a 2D MKA for accurately predicting the forward scattering problem within a low computational cost. The proposal was validated for the shadowing gain caused by an rectangular conductor cylinder, by comparing with MoM. This study also proposed the design of the MKA parameters and the combination of the windowing functions to reduce the size of FFT. The applicable range of MKA was extended to the arbitrary shaped cylinder by multiple planes. This study found that, only the space domain of the zeroth plane and the angular spectrum domain of the last plane needed their separate windowing functions for accuracy and computational cost. The author validated the proposal for an elliptical conductor cylinder with the size of the human body at mmWave (17 GHz – 66.5 GHz). The results showed that the proposed method presented good accuracy with a low RMSE of less than 0.5 dB, compared with the MoM as the reference. Furthermore, the calculation time was improved by 1.4 – 67.2 times compared with the UTD for the human-scale problem. The order of computational cost of MKA was $LN \log_2 N$.

6.2 Contribution

This research can provide a fast and accurate forward scattering prediction method of a thick object EM simulation. Not only EM wave, but also other strong-wave forward scattering problems can apply this method. It also contributes to other academic or industry field.

The applicable range of KA is extended to a thick object by MKA. This study proposes the design of the truncation region and resolution of FFT. In the space domain, the windowing function based on FZN is extended to the forward scattering problem. In the angular spectrum domain, a rectangular windowing function is proposed to use for accuracy and computational cost. The paper also proposes a combination of windowing functions in multiple planes for better accuracy and lower calculation time.

6.3 Applicability for 3-dimensional Object

The extension of the applicable range to the 3-dimensional (3D) object can be considered as the future prospect. The 3D arbitrary shaped object will be modelled as the combination of several cuboid. The issues of MKA for 3D problems are the image mirror theory for the curved object and the computational cost. Firstly, the current MKA has the difficulty to deal with the curved mirror. Finding the way for satisfying boundary condition of the curved mirror is considered as a future topic. Secondly, MKA for 3D problem uses 2D FFT, a higher computational cost is needed. The use of GPU for reducing the computational time is also considered as a future study.

Appendix A

Derivations of Resolution and Windowing Size in Space Domain

According to key intuition P2, the phase function $\phi_1(\cdot)$ of Hankel function around $x \simeq 0$ is

$$\phi_1(x) = \frac{k_0}{2b}x^2 \tag{A.1}$$

The spatial windowing boundary with the coordinate of a_i should be n_p phase rotations away from the edge with the coordinate of $w_{0,i}$.

$$\phi_1(a_i) - \phi_1(w_{0,i}) = n_\mathrm{p}\frac{\pi}{2} \tag{A.2a}$$

$$\Rightarrow a_i = \sqrt{w_{0,i}^2 + \frac{2b\pi}{k_0}n_\mathrm{p}} \tag{A.2b}$$

The coordinate a_i', which is 2π phase smaller than a_i, is

$$\phi_1(a_i) - \phi_1(a_i') = 2\pi \tag{A.3a}$$

$$\Rightarrow a_i' = \sqrt{w_{0,i}^2 + \frac{2b\pi}{k_0}(n_\mathrm{p} - 2)} \tag{A.3b}$$

Thus, the size Δa_i of the last phase period within the window is

$$\Delta a_i = a_i - a_i' \tag{A.4a}$$

$$= \sqrt{w_{0,i}^2 + \frac{2b\pi}{k_0}n_\mathrm{p}} - \sqrt{w_{0,i}^2 + \frac{2b\pi}{k_0}(n_\mathrm{p} - 2)} \tag{A.4b}$$

Since Δa_i should be sampled by n_s points, the sampling interval Δx_i should be

$$\Delta a_i = n_\mathrm{s}\Delta x_i \tag{A.5a}$$

$$\Rightarrow \Delta x_i = \frac{\sqrt{w_{0,i}^2 + \frac{2b\pi}{k_0}n_\mathrm{p}} - \sqrt{w_{0,i}^2 + \frac{2b\pi}{k_0}(n_\mathrm{p} - 2)}}{n_\mathrm{s}} \tag{A.5b}$$

The proposed interval $\Delta x'$ should satisfy both Δx of (4.2) and Δx_i as

$$\Delta x' = \min_{i=1,2}(\Delta x, \Delta x_i) \tag{A.6}$$

Since the updated $\Delta x'$ may be smaller than Δx_i, for better accuracy, the window size with sufficient sampling points can be larger than a_i, which just satisfies the minimum requirements of truncation with the phase change number of n_p. Suppose a is the updated coordinate of the windowing boundary. The coordinate a', which is 2π phase smaller than a, is

$$\phi_1(a) - \phi_1(a') = 2\pi \tag{A.7a}$$

$$\Rightarrow a' = \sqrt{a^2 - \frac{4b\pi}{k_0}} \tag{A.7b}$$

Thus, the size Δa of the last phase period within the window is

$$\Delta a = a - a' \tag{A.8a}$$

$$= a - \sqrt{a^2 - \frac{4b\pi}{k_0}} \tag{A.8b}$$

Since Δa should be sampled by n_s points, a can be derived as

$$\Delta x' = \frac{\Delta a}{n_\mathrm{s}} = \frac{a - \sqrt{a^2 - \frac{4b\pi}{k_0}}}{n_\mathrm{s}} \tag{A.9a}$$

$$\Rightarrow a = \frac{n_\mathrm{s}^2 k_0 \Delta x'^2 + 4\pi b}{2 n_\mathrm{s} k_0 \Delta x'} \tag{A.9b}$$

Appendix B

Derivations of Resolution and Windowing Size in Angular Spectrum Domain

In case C1, according to key intuition P4, the size of the phase period everywhere for k_{x} is $2\pi/|w_{0,i}|$ and $2\pi/a$ ($a > w_{0,i}$). Each phase period should be sampled by at least n_{s} points as

$$\min_{i=1,2}(\frac{2\pi}{a}, \frac{2\pi}{|w_{0,i}|}) = n_{\mathrm{s}}\frac{2\pi}{X_1} \tag{B.1a}$$

$$\Rightarrow X_1 = n_{\mathrm{s}} \tag{B.1b}$$

If there is no spatial windowing function, since the term a vanishes, the size of the phase period is $2\pi/|w_{0,i}|$.

$$\min_{i=1,2}(\frac{2\pi}{|w_{0,i}|}) = n_{\mathrm{s}}\frac{2\pi}{X_3} \tag{B.2a}$$

$$\Rightarrow X_3 = \max_{i=1,2} n_{\mathrm{s}}|w_{0,i}| \tag{B.2b}$$

In case C2, according to key intuition P6, the phase function $\phi_2(\cdot)$ of $e^{-\mathrm{j}k_z d}$ around $k_{\mathrm{x}} \simeq 0$ is

$$\phi_2(k_{\mathrm{x}}) = \frac{d}{2k_0}k_{\mathrm{x}}^2 \tag{B.3}$$

For the NLoS condition in case C2, the phase period at poles $k_{\mathrm{x}} = k_0 a/b$ and $k_{\mathrm{x}} = k_0|w_{0,i}|/b$ should be sampled by n_{s} points.

$$\phi_2(k_{\mathrm{x}}) - \phi_2(k_{\mathrm{x}} - n_{\mathrm{s}}\frac{2\pi}{X_2}) = 2\pi \tag{B.4a}$$

$$k_{\mathrm{x}} = \max_{i=1,2}(\frac{k_0 a}{b}, \frac{k_0|w_{0,i}|}{b}) \tag{B.4b}$$

$$\Rightarrow X_2 = \frac{n_{\mathrm{s}} d a}{b} \tag{B.4c}$$

If there is no spatial windowing function, then the pole of $k_{\mathrm{x}} = k_0 a/b$ vanishes.

$$\phi_2(k_{\mathrm{x}}) - \phi_2(k_{\mathrm{x}} - n_{\mathrm{s}}\frac{2\pi}{X_4}) = 2\pi \tag{B.5a}$$

$$k_{\mathrm{x}} = \max_{i=1,2}(\frac{k_0|w_{0,i}|}{b}) \tag{B.5b}$$

$$\Rightarrow X_4 = \max_{i=1,2}\frac{n_{\mathrm{s}} d|w_{0,i}|}{b} \tag{B.5c}$$

For the LoS condition in case C2, the phase period of $\tilde{E}_{0,i}(k_{\mathrm{x}})e^{-\mathrm{j}k_{\mathrm{z}}d}$ at peak $k_{\mathrm{x}} = 0$ is the same as $\tilde{E}_{0,i}(k_{\mathrm{x}})$ due to $\tilde{E}_{0,i}(k_{\mathrm{x}})e^{-\mathrm{j}k_{\mathrm{z}}d}|_{k_{\mathrm{x}}=0} = \tilde{E}_{0,i}(k_{\mathrm{x}})|_{k_{\mathrm{x}}=0}$. Thus, the LoS condition in case C2 has the same conclusion as case C1.

Truncation size k_{w} is calculated by using the Nyquist sampling number n_{c} as

$$\phi_2(k_{\mathrm{w}}) - \phi_2(k_{\mathrm{w}} - n_{\mathrm{c}}\frac{2\pi}{X_\alpha}) = 2\pi \tag{B.6a}$$

$$\Rightarrow k_{\mathrm{w}} = \frac{k_0 X_\alpha}{n_{\mathrm{c}} d} \tag{B.6b}$$

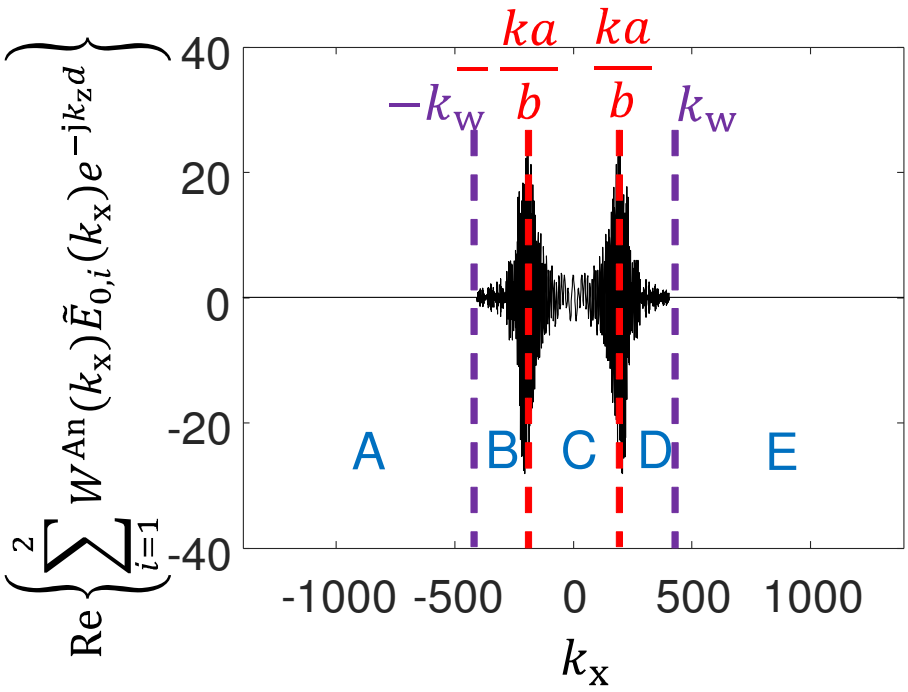

Figure B.1: Five regions of $\sum_{i=1}^{2}\tilde{E}_{0,i}(k_{\mathrm{x}})e^{-\mathrm{j}k_{\mathrm{z}}d}$.

The authors explain the reason for using the Nyquist sampling criterion in the angular spectrum domain. Figure B.1 uses poles $k_{\mathrm{x}} = \pm k_0 a/b$ and boundaries $k_{\mathrm{x}} = \pm k_{\mathrm{w}}$ to separate Fig. 4.5(b) into five regions, i.e., A, B, C, D, and E. Regions A and E cannot be sampled by at least n_{c} points. Regions B and D are sampled from n_{c} to n_{s} points. Region C is sampled by at least n_{s} points. The insufficiently sampled regions A and E can be truncated due

to the cancellation of the radiation integration. The sufficiently sampled regions C should remain due to the contribution of the integral. However, the transition regions B and D, where many peaks of the oscillating $\sum_{i=1}^{2}\tilde{E}_{0,i}(k_{\mathrm{x}})e^{-\mathrm{j}k_z d}$ are around the poles, also play an important role in the integration. If we suddenly truncate by using n_{s} sampling criterion, then transition regions B and D will vanish causing the accuracy issue due to the lack of peaks in $|k_{\mathrm{x}}| \geq k_0 a/b$. The reason for using n_{c} sampling criterion for truncation is because it can retain many peaks with heights over $n_{\mathrm{c}}/n_{\mathrm{s}}$ of the highest peak. The proof is as follows.

Proof Suppose the peak at pole $k_{\mathrm{x}} = k_0 a/b$ is the highest peak with the height of h_1, and the height of the peak at boundary $k_{\mathrm{x}} = k_{\mathrm{w}}$ is h_2. According to key intuition P5, since the envelope of $\tilde{E}_{0,i}(k_{\mathrm{x}})e^{-\mathrm{j}k_z d}$ is k_{x}^{-1}-dependent, we have

$$h_1\frac{k_0 a}{b} = h_2 k_{\mathrm{w}} \tag{B.7}$$

In addition, the sampling numbers of phase periods at $k_{\mathrm{x}} = k_0 a/b$ and $k_{\mathrm{x}} = k_{\mathrm{w}}$ are n_{s} and n_{c}, respectively. Thus, we have

$$\phi_2(\frac{k_0 a}{b}) - \phi_2(\frac{k_0 a}{b} - n_{\mathrm{s}}\frac{2\pi}{X_\alpha}) = 2\pi \tag{B.8a}$$

$$\phi_2(k_{\mathrm{w}}) - \phi_2(k_{\mathrm{w}} - n_{\mathrm{c}}\frac{2\pi}{X_\alpha}) = 2\pi \tag{B.8b}$$

$$\Rightarrow n_{\mathrm{s}}\frac{k_0 a}{b} = n_{\mathrm{c}} k_{\mathrm{w}} \tag{B.8c}$$

From (B.7) and (B.8c), we can prove that

$$h_2 = \frac{n_{\mathrm{c}}}{n_{\mathrm{s}}}h_1 \tag{B.9}$$

□

For the values of $n_c = 2$ and $n_s = 10$, only the peaks with heights less than 20% of h_1, which do not significantly influence the next FT, are truncated. Thus, the accuracy of the truncation is not an issue. For the discretization, it is better not to unify the sampling criteria in the space and angular spectrum domains. If we unify $n_c = 10$ in the angular spectrum domain and want to retain the same peaks with heights over 20% of h_1, then n_s will reach 50 points. According to (4.14), X_α will be 5 times larger than before causing a significant increase in the calculation time. If we unify $n_s = 2$ in the space domain, according to (4.5), where the dominant part is

$$a = \frac{n_{\mathrm{s}}^2 k_0 \Delta x'^2 + 4\pi b}{2 n_{\mathrm{s}} k_0 \Delta x'} \sim \frac{2\pi b}{n_{\mathrm{s}} k_0 \Delta x'} \tag{B.10}$$

a will be 5 times larger than before. According to (4.14b), X_2 will also be 5 times larger than before causing a significant increase in the calculation time. This paper has already shown that the combination of $n_c = 2$ and $n_s = 10$ can present a good accuracy with a low RMSE of less than 0.5 dB. Therefore, there is no need to unify the sampling criteria in the two domains for a lower computational cost.

Appendix C

Determination of Maximum Propagation Angle

The maximum propagation angle θ_{m} is related to the slope of the object. For the object with the varying slopes, the mean value of those slopes can be considered as the represented slope. However, even for the object with a fixed slope, $\tan\theta_{\mathrm{m}}$ can not be directly equal to that slope since the wave propagates to the space, not only along the surface of object. Thus, $\tan\theta_{\mathrm{m}}$ should be larger than the represented slope to make a room for propagating to the space. Therefore, we need find some reference values of θ_{m} to compare with the represented slope. In this study, three assumptions are considered as follows.

- **Assumption 1**
  The minimum and step of reference values of θ_{m} are considered as 15°.
- **Assumption 2**
  Since the larger θ_{m} results the smaller planes interval causing a increase of computational cost, the maximum of reference values of θ_{m} needs to be designed for a low computational cost. According to (5.1), interval with $\theta_{\mathrm{m}} = 45°$ is calculated as 1.6λ, which is small enough for accuracy [146]. Thus, the maximum of reference values of θ_{m} is considered as 45°. It means that only three θ_{m} are considered as the reference values, i.e., 15°, 30°, and 45°.
- **Assumption 3**
  To find a room for propagating to the space, if the represented slope is smaller than 15°, θ_{m} is proposed as 15°. If the represented slope is smaller than 30° but larger than 15°, θ_{m} is proposed as 30°. If the represented slope is larger than 30°, θ_{m} is proposed as 45°.

By using the above assumptions, the value of θ_{m} for an ellipse with the rotation angle of $\theta = 0°$ is calculated as follows. Figure C.1 shows the model of the targeted ellipse with the semi-major and semi-minor of r_1 and r_2, respectively, in ζ-η domain with the origin at the center of the ellipse. The slope $s(\theta_0)$ of the arbitrary points $(r_1\cos\theta_0, r_2\sin\theta_0)$ can be calculated as

$$s(\theta_0) = -\frac{r_2}{r_1}\frac{1}{\tan\theta_0} \tag{C.1}$$

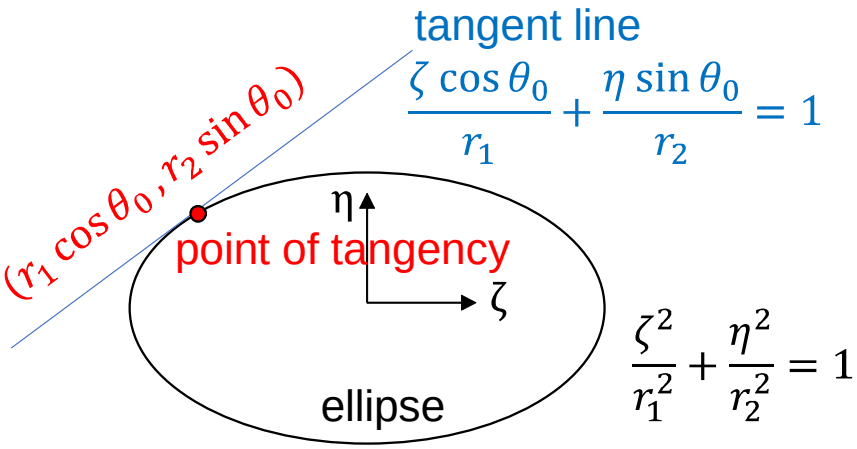

Figure C.1: Model of an ellipse with $\theta = 0°$

considering the symmetry of the ellipse, the mean value of the slopes $\bar{s}$ can be calculated from only the left-upper part $(\zeta < 0, \eta > 0)$ as

$$\bar{s} = \frac{1}{r_1}\int_{\zeta=-r_1}^{\zeta=0} s(\theta_0)\mathrm{d}\zeta \tag{C.2a}$$

$$= \frac{1}{r_1}\int_{\theta_0=\pi}^{\theta_0=\frac{\pi}{2}} -\frac{r_2}{r_1}\frac{1}{\tan\theta_0}\mathrm{d}r_1\cos\theta_0 \tag{C.2b}$$

$$= \frac{r_2}{r_1}\int_{\theta_0=\pi}^{\theta_0=\frac{\pi}{2}} \cos\theta_0\mathrm{d}\theta_0 \tag{C.2c}$$

$$= \frac{r_2}{r_1}\Big[\sin\theta_0\Big]_{\theta_0=\pi}^{\theta_0=\frac{\pi}{2}} \tag{C.2d}$$

$$= \frac{r_2}{r_1} \tag{C.2e}$$

since for each scenario r_2/r_1 is 0.4, which is between $\tan 15°$ and $\tan 30°$, θ_m is defined as 30° according to assumption 3.

Similarly, for ellipses with the rotation angle of $\theta = 45°$ and $\theta = 90°$, we can calculate and define θ_m for them are 45° and 45°, respectively.

Appendix D

Comparison of Computional Complexity of UTD, MKA, MoM, and MLFMA

The computational complexities of all the methods are derived by an order calculation of frequency.

Since UTD is frequency-independent for an analytically shaped object such as the circle and ellipse, but needs a linear integral for an arbitrarily shaped object, the computational complexity of UTD t^{UTD} is

$$t^{\mathrm{UTD}} \sim \begin{cases} O\left(f^0\right) & \text{(for analytically shaped object)} \\ O\left(f\right) & \text{(otherwise)} \end{cases} \tag{D.1}$$

For MKA, according to (5.6), the unit of X' is the meter. Thus, if the frequency become higher with the same distance parameter, X' will increase with the $O\left(f\right)$. On the other hand, according to (B.10) in Appendix A, $\Delta x'$ is equivalent to

$$\Delta x' = \frac{2\pi b}{n_{\mathrm{s}} k_0 a} = \frac{2\pi b}{n_{\mathrm{s}} k_0 \sqrt{w_{0,i}^2 + \frac{2\pi k_0}{b} n_{\mathrm{p}}}} \tag{D.2}$$

Since the dominate part of (D.2) is

$$\Delta x' \sim \frac{2\pi b}{n_{\mathrm{s}} k_0 w_{0,i}} \tag{D.3}$$

there is no unit for $\Delta x'$. Therefore, $N = X'/\Delta x'$ increases with the $O\left(f\right)$.

For the parameter L, it is determined by the ratio of the thickness and the interval of planes. According to (5.1), the interval of planes is proportional to the wavelength for case of $\theta_{\mathrm{m}} \neq 0$. Thus, the computational complexity of L with a fixed thickness increases with the $O\left(f\right)$. However, for the object with a rectangular cross section such as the car

or building, θ_{m} is zero. Then, the interval of planes can be infinite large, which makes L frequency-independent. Therefore, the computational complexity of MKA t^{MKA} is

$$t^{\mathrm{MKA}} \sim \begin{cases} O\left(f \log_2 f\right) & \text{(for rectangular cross-section object)} \\ O\left(f^2 \log_2 f\right) & \text{(otherwise)} \end{cases} \tag{D.4}$$

On the other hand, the computational cost of 2D MoM is $O\left(M^3\right)$, where M is the number of meshes. As state of the art, its fast variant MLFMA reduces the computational cost from $O\left(M^3\right)$ to $O\left(M \log_2 M\right)$. Since M increases with the $O\left(f\right)$. Therefore, the computational complexities of MoM t^{MoM} and MLFMA t^{MLFMA} are

$$t^{\mathrm{MoM}} \sim O\left(f^3\right) \tag{D.5}$$

$$t^{\mathrm{MLFMA}} \sim O\left(f \log_2 f\right) \tag{D.6}$$

Although above all imply that UTD may be faster than MKA at a higher frequency in case of $\theta_{\mathrm{m}} \neq 0$, they have not discussed the time for finding diffraction and refection points. For an arbitrarily shaped object, it is not possible to estimate the search time for the diffraction and reflection points. Even if UTD is faster than MKA at a higher frequency, the accuracy is still an issue for ray-based UTD such as the tunnel environment, where multiple reflections are the main propagation phenomenon and are difficult to predict by ray-based approaches. Moreover, there is a problem for UTD that the curvature, diffraction points, reflection points, and integral path may not be found precisely for the arbitrarily shaped object, which cause error of calculation accuracy. Furthermore, the formulation of UTD may be more difficult for some analytically shaped object (e.g., ellipse).

Similarly, above all imply that MLFMA may be faster than MKA at a higher frequency in case of $\theta_{\mathrm{m}} \neq 0$. However, for the computational memory, they have the same frequency dependency, and MKA may have the lower memory compared with MLFMA. The author derives it as follows. Considering (D.3) for $\Delta x'$, since the dominate part of X' is

$$X' = \frac{n_{\mathrm{s}}(c - Ld)|w_{L,i}|}{b + Ld} \sim \frac{n_{\mathrm{s}} c |w_{L,i}|}{b} \tag{D.7}$$

MKA's memory N will be

$$N \sim \frac{n_{\mathrm{s}}^2 c |w_{0,i} w_{L,i}|}{\lambda b^2} \tag{D.8}$$

For the sake of simplicity, a circular cylinder with a radius r is considered as the shadowing object. Then, the MLFMA's memory M is considered as the meshes number of the circular boundary as

$$M = \frac{2\pi r n_{\mathrm{s}}}{\lambda} \tag{D.9}$$

The radio of M and N is

$$\frac{M}{N} = \frac{2\pi r b^2}{n_{\mathrm{s}} c |w_{0,i} w_{L,i}|} > \frac{2\pi b^2}{n_{\mathrm{s}} c r} \tag{D.10}$$

If we consider the often-used $n_{\mathrm{s}} = 10$, then M/N becomes

$$\frac{M}{N} \sim 0.6 \frac{b^2}{cr} \tag{D.11}$$

Since the shadowing scenario in 5G usually has the condition of $b \leq c, r$, the MLFMA's memory is a least $0.6b^2/(cr)$ times larger than MKA. Therefore, we can conclude that MKA has a lower memory compared with MLFMA.

Appendix E

Step Approximation for An Arbitrarily Shaped Object

An ellipse is modelled as a polygon by the step approximation, as shown in Fig. E.1. MoM is applied to compare the shadowing gains between the original ellipse and the polygon approximation. The simulation condition is the same as scenario 1 in Chapter 5, where three rotation angles are considered, i.e., $\theta = 0°$, $\theta = 45°$, and $\theta = 90°$. The accuracy of the polygon approximation is validated by comparing with the original ellipse as shown in Fig. E.2 - Fig. E.4. From the results, we can find that the step approximation has a good accuracy for forward scattering problem.

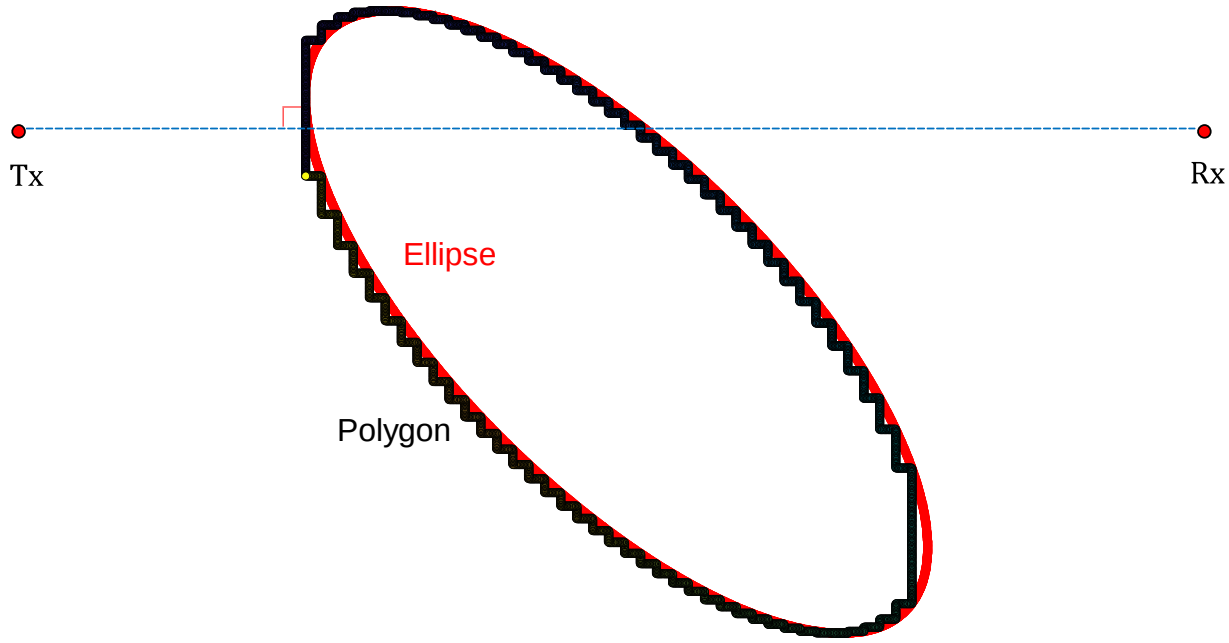

Figure E.1: Model of step approximation

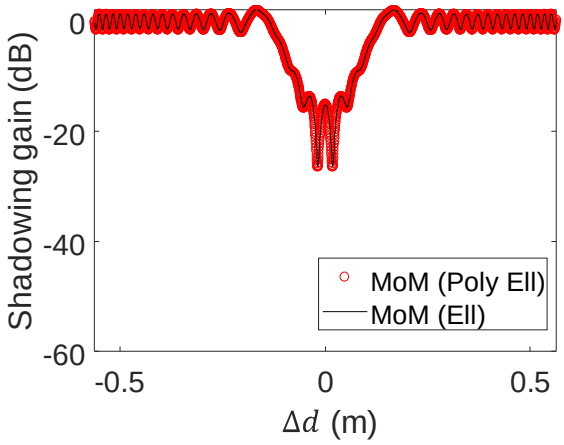

Figure E.2: Comparison the shadowing gains between polygon and ellipse for $\theta = 0°$

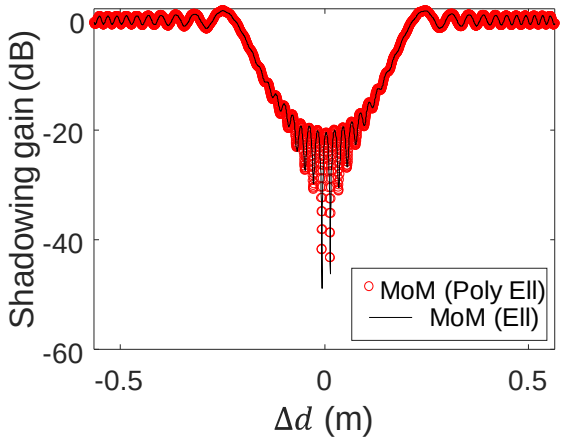

Figure E.3: Comparison the shadowing gains between polygon and ellipse for $\theta = 45°$

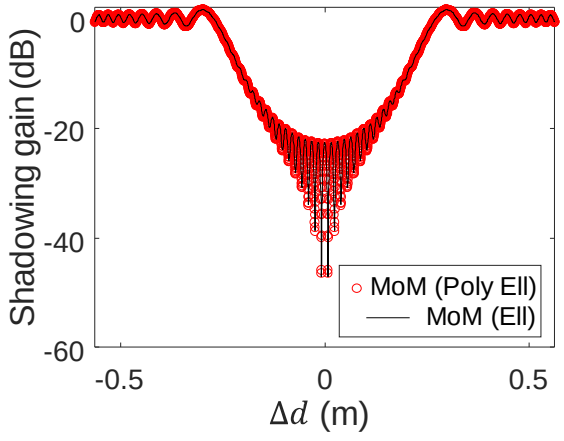

Figure E.4: Comparison the shadowing gains between polygon and ellipse for $\theta = 90°$

Appendix F

MATLAB Code

The MATLAB code for MKA is shown in F.1.

Listing F.1: MKA code

```
tic

% Initial parameters

c =  299792458;
f = 66.5E9;
lambda = c / f;
angular_frequency = 2 * pi * f;
permeability  = 4*pi*10^-7;
permittivity = 1/(permeability*c^2);
impedance = (permeability/permittivity)^0.5;
k_0 = 2 * pi / lambda;
I_0=1;
r_1=0.25;
r_2=0.1;
d_1=2;
d_2=8;
n_s=10;
n_c=2;
n_p=7;
epsilon=10^(-6);
theta_m=30;
theta=0;
delta_d=0;
interval=lambda./(deg2rad(theta_m)).^2;
E_free=-k_0^2*I_0/(4*angular_frequency*permittivity)...
    .*besselh(0,2,k_0*(d_1+d_2));
L=ceil(2*sqrt(r_1^2*cosd(theta)^2+r_2^2*sind(theta)^2)/interval);
w1p=(1/r_1/r_2*sqrt(2)*sqrt(r_1^2*cosd(2*theta)+r_1^2-...
    r_2^2*cosd(2*theta)+r_2^2-2*(-sqrt(r_1^2*cosd(theta)^2+...
    r_2^2*sind(theta)^2)+2*sqrt(r_1^2*cosd(theta)^2+...
```

```
    r_2^2*sind(theta)^2)/L)^2)+sind(2*theta)*(-sqrt(r_1^2*...
    cosd(theta)^2+r_2^2*sind(theta)^2)+2*sqrt(r_1^2*cosd(theta)^2+...
    r_2^2*sind(theta)^2)/L)*(1/r_1^2-1/r_2^2))/2/...
    (sind(theta)^2/r_1^2+cosd(theta)^2/r_2^2);
w1m=(-1/r_1/r_2*sqrt(2)*sqrt(r_1^2*cosd(2*theta)+r_1^2-...
    r_2^2*cosd(2*theta)+r_2^2-2*(-sqrt(r_1^2*cosd(theta)^2+...
    r_2^2*sind(theta)^2)+2*sqrt(r_1^2*cosd(theta)^2+...
    r_2^2*sind(theta)^2)/L)^2)+sind(2*theta)*(-sqrt(r_1^2*...
    cosd(theta)^2+r_2^2*sind(theta)^2)+2*sqrt(r_1^2*cosd(theta)^2+...
    r_2^2*sind(theta)^2)/L)*(1/r_1^2-1/r_2^2))/2/(sind(theta)^2/...
    r_1^2+cosd(theta)^2/r_2^2);
d=2*sqrt(r_1^2*cosd(theta)^2+r_2^2*sind(theta)^2)/L;

% Designed parameters

for n_p_candidate=n_p:10000
    if sqrt(w1p^2+2*pi/k_0*n_p_candidate*(d_1-sqrt(r_1^2*...
            cosd(theta)^2+r_2^2*sind(theta)^2)))-sqrt(w1p^2+...
            2*pi/k_0*(n_p_candidate-2)*(d_1-sqrt(r_1^2*cosd(theta)^2+...
            r_2^2*sind(theta)^2)))<=10*pi/sqrt(k_0^2+(-log(epsilon)/d)^2)
        break;
    end
end
n_p=n_p_candidate;
rd1=w1p-delta_d;
rd2=w1m-delta_d;
rb11 = sqrt((rd1)^2+2*(d_1-sqrt(r_1^2*cosd(theta)^2+r_2^2*...
    sind(theta)^2))/k_0*n_p*pi);
rb12 = sqrt((rd2)^2+2*(d_1-sqrt(r_1^2*cosd(theta)^2+r_2^2*...
    sind(theta)^2))/k_0*n_p*pi);
rb13 = sqrt(2*(d_1-sqrt(r_1^2*cosd(theta)^2+r_2^2*sind(theta)^2))/...
    k_0*n_p*pi);
RD1=(1/r_1/r_2*sqrt(2)*sqrt(r_1^2*cosd(2*theta)+r_1^2-r_2^2*...
    cosd(2*theta)+r_2^2-2*(-sqrt(r_1^2*cosd(theta)^2+r_2^2*...
    sind(theta)^2)+(L-1)*2*sqrt(r_1^2*cosd(theta)^2+r_2^2*...
    sind(theta)^2)/L)^2)+sind(2*theta)*(-sqrt(r_1^2*cosd(theta)^2+...
    r_2^2*sind(theta)^2)+(L-1)*2*sqrt(r_1^2*cosd(theta)^2+...
    r_2^2*sind(theta)^2)/L)*(1/r_1^2-1/r_2^2))/2/(sind(theta)^2/...
    r_1^2+cosd(theta)^2/r_2^2);
RD2=(-1/r_1/r_2*sqrt(2)*sqrt(r_1^2*cosd(2*theta)+r_1^2-r_2^2*...
    cosd(2*theta)+r_2^2-2*(-sqrt(r_1^2*cosd(theta)^2+r_2^2*...
    sind(theta)^2)+(L-1)*2*sqrt(r_1^2*cosd(theta)^2+r_2^2*...
    sind(theta)^2)/L)^2)+sind(2*theta)*(-sqrt(r_1^2*cosd(theta)^2+...
    r_2^2*sind(theta)^2)+(L-1)*2*sqrt(r_1^2*cosd(theta)^2+r_2^2*...
    sind(theta)^2)/L)*(1/r_1^2-1/r_2^2))/2/(sind(theta)^2/r_1^2+...
    cosd(theta)^2/r_2^2);
```

```
if delta_d<w1p && delta_d>w1m
    delta_x=min((rb11-sqrt((rb11)^2-4*pi*(d_1-sqrt(r_1^2*cosd(theta)^2+...
        r_2^2*sind(theta)^2))/k_0))/n_s,(rb12-sqrt((rb12)^2-4*pi*...
        (d_1-sqrt(r_1^2*cosd(theta)^2+r_2^2*sind(theta)^2))/k_0))/n_s);
    T=n_s*max([abs(rb11),abs(rb12),(d_2+sqrt(r_1^2*cosd(theta)^2+...
        r_2^2*sind(theta)^2)-(L-1)*2*sqrt(r_1^2*cosd(theta)^2+...
        r_2^2*sind(theta)^2)/L)/(d_1-sqrt(r_1^2*cosd(theta)^2+...
        r_2^2*sind(theta)^2)+(L-1)*2*sqrt(r_1^2*cosd(theta)^2+...
        r_2^2*sind(theta)^2)/L)*abs(RD1),(d_2+sqrt(r_1^2*cosd(theta)^2+...
        r_2^2*sind(theta)^2)-(L-1)*2*sqrt(r_1^2*cosd(theta)^2+r_2^2*...
        sind(theta)^2)/L)/(d_1-sqrt(r_1^2*cosd(theta)^2+r_2^2*...
        sind(theta)^2)+(L-1)*2*sqrt(r_1^2*cosd(theta)^2+r_2^2*...
        sind(theta)^2)/L)*abs(RD2)]);
    N=ceil(T/delta_x);
    if mod(N,2)==1
        N=N+1;
    end
    T=N*delta_x;
else
    delta_x=(rb13-sqrt((rb13)^2-4*pi*(d_1-sqrt(r_1^2*cosd(theta)^2+...
        r_2^2*sind(theta)^2))/k_0))/n_s;
    T=n_s*abs(rb13);
    N=ceil(T/delta_x);
    if mod(N,2)==1
        N=N+1;
    end
    T=N*delta_x;
end
Tx=[-d_1;T/2];
Rx=[d_2;T/2];
x=(delta_x*(-N/2+1):delta_x:delta_x*(N/2))+T/2;
grids=[repmat(-sqrt(r_1^2*cosd(theta)^2+r_2^2*sind(theta)^2),1,N);x];
rho_inc=sqrt((grids(1,:)-Tx(1,:)).^2+(grids(2,:)-Tx(2,:)).^2);
E_0=-k_0^2*I_0/(4*angular_frequency*permittivity).*besselh(0,2,k_0*...
    rho_inc);
rho_scat=sqrt((grids(1,:)-Rx(1,:)).^2+(grids(2,:)-Rx(2,:)).^2);
k_x=2*pi*(-N/2+1:N/2)/T;
k_z=sqrt(k_0^2-k_x.^2);
k_z1=k_z;
id=find(real(k_z)==0);
k_z1(id)=-k_z(id);
Window_an=zeros(1,N);
if (T/n_c)/(d_2+sqrt(r_1^2*cosd(theta)^2+r_2^2*sind(theta)^2)-(L-1)*...
        2*sqrt(r_1^2*cosd(theta)^2+r_2^2*sind(theta)^2)/L)<1
    k_w=k_0*(T/n_c)/(d_2+sqrt(r_1^2*cosd(theta)^2+r_2^2*sind(theta)^2)-...
        (L-1)*2*sqrt(r_1^2*cosd(theta)^2+r_2^2*sind(theta)^2)/L);
```

```
    if N/2+ceil(-T/2/pi*k_w)>0
        id_k_w=(N/2+ceil(-T/2/pi*k_w):N/2+ceil(T/2/pi*k_w));
        Window_an(id_k_w)=1;
    else
        Window_an(:)=1;
    end
else
    Window_an(:)=1;
end
if delta_d>w1p
    Window_sp_1=(cos(pi*(rho_inc+rho_scat-d_1-d_2)./(sqrt((d_1...
        -sqrt(r_1^2*cosd(theta)^2+r_2^2*sind(theta)^2)).^2+rb11.^2)...
        +sqrt((d_2+sqrt(r_1^2*cosd(theta)^2+r_2^2*sind(theta)^2)).^2+...
        rb11.^2)-d_1-d_2))+1)/2;
    id1=find(abs(grids(2,:)-T/2)>rb13|grids(2,:)<T/2+w1p-delta_d);
else
    Window_sp_1=(cos(pi*(rho_inc+rho_scat-sqrt((d_1-sqrt(r_1^2*...
        cosd(theta)^2+r_2^2*sind(theta)^2)).^2+rd1.^2)-sqrt((d_2+...
        sqrt(r_1^2*cosd(theta)^2+r_2^2*sind(theta)^2)).^2+rd1.^2)./...
        (sqrt((d_1-sqrt(r_1^2*cosd(theta)^2+r_2^2*sind(theta)^2)).^2+...
        rb11.^2)+sqrt((d_2+sqrt(r_1^2*cosd(theta)^2+r_2^2*...
        sind(theta)^2)).^2+rb11.^2)-sqrt((d_1-sqrt(r_1^2*...
        cosd(theta)^2+r_2^2*sind(theta)^2)).^2+rd1.^2)-sqrt((d_2+...
        sqrt(r_1^2*cosd(theta)^2+r_2^2*sind(theta)^2)).^2+rd1.^2)))+1)/2;
    id1=find(abs(grids(2,:)-T/2)>rb11|grids(2,:)<T/2+w1p-delta_d);
end
if delta_d<w1m
    Window_sp_2=(cos(pi*(rho_inc+rho_scat-d_1-d_2)./(sqrt((d_1-...
        sqrt(r_1^2*cosd(theta)^2+r_2^2*sind(theta)^2)).^2+rb12.^2)+...
        sqrt((d_2+sqrt(r_1^2*cosd(theta)^2+r_2^2*sind(theta)^2)).^2+...
        rb12.^2)-d_1-d_2))+1)/2;
    id2=find(abs(grids(2,:)-T/2)>rb13|grids(2,:)>T/2+w1m-delta_d);
else
    Window_sp_2=(cos(pi*(rho_inc+rho_scat-sqrt((d_1-sqrt(r_1^2*...
        cosd(theta)^2+r_2^2*sind(theta)^2)).^2+rd2.^2)-sqrt((d_2+...
        sqrt(r_1^2*cosd(theta)^2+r_2^2*sind(theta)^2)).^2+rd2.^2)./...
        (sqrt((d_1-sqrt(r_1^2*cosd(theta)^2+r_2^2*sind(theta)^2)).^2+...
        rb12.^2)+sqrt((d_2+sqrt(r_1^2*cosd(theta)^2+r_2^2*...
        sind(theta)^2)).^2+rb12.^2)-sqrt((d_1-sqrt(r_1^2*...
        cosd(theta)^2+r_2^2*sind(theta)^2)).^2+rd2.^2)-sqrt((d_2+...
        sqrt(r_1^2*cosd(theta)^2+r_2^2*sind(theta)^2)).^2+rd2.^2)))+1)/2;
    id2=find(abs(grids(2,:)-T/2)>rb12|grids(2,:)>T/2+w1m-delta_d);
end

% Implementation of MKA
```

```
Er=E_0.*Window_sp_1;
Er(id1)=0;
El=E_0.*Window_sp_2;
El(id2)=0;
for l=1:L-1
    tilde_Er=ifft(Er.*exp(-2*pi*1j*(N/2-1)/N*(0:N-1))).*exp(-2*pi*...
        1j*(N/2-1)/N*(0:N-1)).*exp(2*pi*1j*(N/2-1)^2/N);
    Er_KA=fft(tilde_Er.*exp(2*pi*1j*(N/2-1)/N*(0:N-1)).*exp(-1j*k_z1*...
        d)).*exp(2*pi*1j*(N/2-1)/N*(0:N-1)).*exp(-2*pi*1j*(N/2-1)^2/N);
    tilde_El=ifft(El.*exp(-2*pi*1j*(N/2-1)/N*(0:N-1))).*exp(-2*pi*...
        1j*(N/2-1)/N*(0:N-1)).*exp(2*pi*1j*(N/2-1)^2/N);
    El_KA=fft(tilde_El.*exp(2*pi*1j*(N/2-1)/N*(0:N-1)).*exp(-1j*k_z1*...
        d)).*exp(2*pi*1j*(N/2-1)/N*(0:N-1)).*exp(-2*pi*1j*(N/2-1)^2/N);
    w2p=max((1/r_1/r_2*sqrt(2)*sqrt(abs(r_1^2*cosd(2*theta)+r_1^2-...
        r_2^2*cosd(2*theta)+r_2^2-2*(-sqrt(r_1^2*cosd(theta)^2+r_2^2*...
        sind(theta)^2)+l*2*sqrt(r_1^2*cosd(theta)^2+r_2^2*...
        sind(theta)^2)/L)^2))+sind(2*theta)*(-sqrt(r_1^2*cosd(theta)^2+...
        r_2^2*sind(theta)^2)+l*2*sqrt(r_1^2*cosd(theta)^2+r_2^2*...
        sind(theta)^2)/L)*(1/r_1^2-1/r_2^2))/2/(sind(theta)^2/r_1^2+...
        cosd(theta)^2/r_2^2),(1/r_1/r_2*sqrt(2)*sqrt(abs(r_1^2*...
        cosd(2*theta)+r_1^2-r_2^2*cosd(2*theta)+r_2^2-2*(-sqrt(r_1^2*...
        cosd(theta)^2+r_2^2*sind(theta)^2)+(l+1)*2*sqrt(r_1^2*...
        cosd(theta)^2+r_2^2*sind(theta)^2)/L)^2))+sind(2*theta)*...
        (-sqrt(r_1^2*cosd(theta)^2+r_2^2*sind(theta)^2)+(l+1)*2*...
        sqrt(r_1^2*cosd(theta)^2+r_2^2*sind(theta)^2)/L)*(1/r_1^2-...
        1/r_2^2))/2/(sind(theta)^2/r_1^2+cosd(theta)^2/r_2^2));
    w2m=min((-1/r_1/r_2*sqrt(2)*sqrt(abs(r_1^2*cosd(2*theta)+r_1^2-...
        r_2^2*cosd(2*theta)+r_2^2-2*(-sqrt(r_1^2*cosd(theta)^2+r_2^2*...
        sind(theta)^2)+l*2*sqrt(r_1^2*cosd(theta)^2+r_2^2*...
        sind(theta)^2)/L)^2))+sind(2*theta)*(-sqrt(r_1^2*cosd(theta)^2+...
        r_2^2*sind(theta)^2)+l*2*sqrt(r_1^2*cosd(theta)^2+r_2^2*...
        sind(theta)^2)/L)*(1/r_1^2-1/r_2^2))/2/(sind(theta)^2/r_1^2+...
        cosd(theta)^2/r_2^2),(-1/r_1/r_2*sqrt(2)*sqrt(abs(r_1^2*cosd(2*...
        theta)+r_1^2-r_2^2*cosd(2*theta)+r_2^2-2*(-sqrt(r_1^2*...
        cosd(theta)^2+r_2^2*sind(theta)^2)+(l+1)*2*sqrt(r_1^2*...
        cosd(theta)^2+r_2^2*sind(theta)^2)/L)^2))+sind(2*theta)*...
        (-sqrt(r_1^2*cosd(theta)^2+r_2^2*sind(theta)^2)+(l+1)*2*...
        sqrt(r_1^2*cosd(theta)^2+r_2^2*sind(theta)^2)/L)*(1/r_1^2-...
        1/r_2^2))/2/(sind(theta)^2/r_1^2+cosd(theta)^2/r_2^2));
    w3p=(1/r_1/r_2*sqrt(2)*sqrt(abs(r_1^2*cosd(2*theta)+r_1^2-r_2^2*...
        cosd(2*theta)+r_2^2-2*(-sqrt(r_1^2*cosd(theta)^2+r_2^2*...
        sind(theta)^2)+l*2*sqrt(r_1^2*cosd(theta)^2+r_2^2*...
        sind(theta)^2)/L)^2))+sind(2*theta)*(-sqrt(r_1^2*cosd(theta)^2+...
        r_2^2*sind(theta)^2)+l*2*sqrt(r_1^2*cosd(theta)^2+r_2^2*...
        sind(theta)^2)/L)*(1/r_1^2-1/r_2^2))/2/(sind(theta)^2/r_1^2+...
        cosd(theta)^2/r_2^2);
```

```
    w3m=(-1/r_1/r_2*sqrt(2)*sqrt(abs(r_1^2*cosd(2*theta)+r_1^2-r_2^2*...
        cosd(2*theta)+r_2^2-2*(-sqrt(r_1^2*cosd(theta)^2+r_2^2*...
        sind(theta)^2)+l*2*sqrt(r_1^2*cosd(theta)^2+r_2^2*...
        sind(theta)^2)/L)^2))+sind(2*theta)*(-sqrt(r_1^2*cosd(theta)^2+...
        r_2^2*sind(theta)^2)+l*2*sqrt(r_1^2*cosd(theta)^2+r_2^2*...
        sind(theta)^2)/L)*(1/r_1^2-1/r_2^2))/2/(sind(theta)^2/r_1^2+...
        cosd(theta)^2/r_2^2);
    Er_MKA=zeros(1,N);
    El_MKA=zeros(1,N);
    id3=ceil(-(-N/2+1)+1+(w2p-delta_d)/delta_x);
    id5=round(-(-N/2+1)+1+(w3p-delta_d)/delta_x);
    if 2*id5-N<=0
        Er_MKA(id3:1:(2*id5-1))=Er_KA(id3:1:(2*id5-1))-...
            Er_KA((2*id5-id3):-1:1);
    else
        Er_MKA(id3:1:N)=Er_KA(id3:1:N)-Er_KA((2*id5-id3):-1:(2*id5-N));
    end
    id4=floor(-(-N/2+1)+1+(w2m-delta_d)/delta_x);
    id6=round(-(-N/2+1)+1+(w3m-delta_d)/delta_x);
    if 2*id6-1>N
        El_MKA((2*id6-N):1:id4)=El_KA((2*id6-N):1:id4)-...
            El_KA(N:-1:(2*id6-id4));
    else
        El_MKA(1:1:id4)=El_KA(1:1:id4)-El_KA((2*id6-1):-1:(2*id6-id4));
    end
    Er=Er_MKA;
    El=El_MKA;
end
E_L=Er+El;
tilde_E=ifft(E_L.*exp(-2*pi*1j*(N/2-1)/N*(0:N-1))).*exp(-2*pi*1j*...
    (N/2-1)/N*(0:N-1)).*exp(2*pi*1j*(N/2-1)^2/N);
E_desired=fft(tilde_E.*Window_an.*exp(2*pi*1j*(N/2-1)/N*(0:N-1)).*...
    exp(-1j*k_z1*(d_2+(sqrt(r_1^2*cosd(theta)^2+r_2^2*sind(theta)^2)-...
    (L-1)*2*sqrt(r_1^2*cosd(theta)^2+r_2^2*sind(theta)^2)/L)))).*...
    exp(2*pi*1j*(N/2-1)/N*(0:N-1)).*exp(-2*pi*1j*(N/2-1)^2/N);

% Post-processing

SG_MKA=mag2db(abs(E_desired(N/2)))-mag2db(abs(E_free));
Time_MKA=toc;
```

Bibliography

[1] NTT DOCOMO, INC., DOCOMO 5G White Paper, 5G Radio Access: Requirement, Concept and Technologies, July, 2014.

[2] CISCO, Cisco Visual Networking Index: Mobile Data Traffic Forecast Update, 2015-2020, 2017.

[3] METIS, "Mobile and wireless communications Enablers for the Twenty-twenty Information Society," *in EU 7th Framework Programmer.* (https://www.metis2020.com/)

[4] 5GCM white paper, "5G Channel Model for bands up to 100 GHz," *in Global Communications Conference, 3rd Workshop on Mobile Communication in Higher Frequency Bands,* Washington DC, U.S.A, May, 2016.

[5] 3GPP TR38.900, Channel model for frequency spectrum above 6 GHz, June, 2016.

[6] ITU-R, "Studies on frequency-related matters for International Mobile Telecommunications identification including possible additional allocations to the mobile services on a primary basis in portions of the frequency range between 24.25 and 86 GHz for the future development of International Mobile Telecommunication for 2020 and beyond," *in The World Radio-communication Conference-19,* p. 296, Geneva, July, 2016.

[7] MIWEBA, Deliverable D5.1, Channel Modelling and Characterization, June, 2014.

[8] J. G. Andrews, S. Buzzi, W. Choi, S. V. Hanly, A. Lozano, A. C. K. Soong, and J. C. Zhang, "What will 5G be?" *IEEE J. Sel. Areas Commun.,* vol. 32, no. 6, pp. 1065-1082, June 2014.

[9] S. Rangan, T. S. Rappaport, and E. Erkip, "Millimeter-wave cellular wireless networks: Potentials and challenges," *Proc. IEEE,* vol. 102, no. 3, pp. 366-385, Mar. 2014.

[10] H. T. Friis, "A note on a simple transmission formula," *Proc. IRE,* vol. 34, no. 5, pp. 254-256, May 1946.

[11] T. S. Rappaport, G. R. MacCartney, S. Sun, H. Yan, and S. Deng, "Small-Scale, Local Area, and Transitional Millimeter Wave Propagation for 5G Communications," *IEEE Trans. Antennas Propag.,* vol. 65, no. 12, pp. 6474-6490, Dec. 2017.

[12] M. K. Samimi and T. S. Rappaport, "3-D millimeter-wave statistical channel model for 5G wireless system design," *IEEE Trans. Microw. Theory Techn.,* vol. 64, no. 7, pp. 2207-2225, Jul. 2016.

[13] S. Sun, G. R. MacCartney, Jr., M. K. Samimi, and T. S. Rappaport, "Synthesizing omnidirectional antenna patterns, received power and path loss from directional antennas for 5G millimeter-wave communications," *in Proc. IEEE Global Commun. Conf. (GLOBECOM),* Dec. 2015, pp. 3948-3953.

[14] S. Sun, T. S. Rappaport, R. W. Heath, Jr., A. Nix, and S. Rangan, "MIMO for millimeter-wave wireless communications: Beamforming, spatial multiplexing, or both?" *IEEE Commun. Mag.,* vol. 52, no. 12, pp. 110-121, Dec. 2014.

[15] Iswandi, T. Aoyagi, M. Kim, and J. Takada, "The utilization of body skeleton model for modeling the dynamic BAN channels," *in 2012 6th European Conference on Antennas and Propagation (EUCAP),* 2012, pp. 540-543.

[16] S. Ali and M. Junaid Mughal, "Narrowband Characterization of the 60GHz Indoor Radio Channel in the Presence of Human Bodies," *in Proceedings of the 6th International Conference on Emerging Technologies,* pp. 226-229, 2010.

[17] Y. Huang, A. Charbonneau, L. Talbi, and T. A. Denidni, "Effect of human body upon line-of-sigth indoor radio," *in Canadian Conference on Electrical and Computer Engineering,* pp. 1775-1778, 2006.

[18] A. D. C. Queiroz and L. C. Trintinalia, "An Analysis of Human Body Shadowing Models for Ray-tracing Radio Channel Characterization," *in SBMO/IEEE MTT-S IMOC,* Porto de Galinhas, 2015.

[19] T. Sarkar, Z. Ji, K. Kim, A. Medouri, and M. Salazar-Plama, "A Survey of Various Propagation Models for Mobile Communications," *IEEE Trans. Antennas Propag.,* vol. 45, no. 3, pp. 51-82, June 2003.

[20] R. D. Murch, K. W. Cheung, M. S. Fong, J. H. M. Sau, and J. Chuang, "A New Approach to Indoor Propagation Prediction," *in Proc. IEEE VTC,* Stockholm, Sweden, vol. 3, 1994, pp. 1737-1740.

[21] J. Walfisch and H. L. Bertoni, "A Theoretical Model of UHF Propagation in Urban Environments," *IEEE Trans. Antennas Propag.,* vol. 36, no. 12, pp. 1788-1796, Dec. 1998.

[22] Z. J. Csendes and P. Silvester, "Numerical Solution of Dielectric Loaded Waveguides: I-Finite-Element Analysis," *IEEE Trans. Microw. Theory Techn.,* vol. 18, no. 12, pp. 1124-1131, Dec. 1970.

[23] R. F. Harrington, Field Computation by Moment Method, New York, USA: Macmillan, 1968, pp. 1-6.

[24] W. C. Chew, J. M. Jin, E. Michielssen, and J. Song, Fast and Efficient Algorithms in Computational Electromagnetic, Boston, USA: Artech House, 2001.

[25] K. S. Yee, "Numerical Solution of Initial Boundary Value Problems Involving Maxwell's Equation in Isotropic Media," *IEEE Trans. Antennas Propag.,* vol. 14, no. 3, pp. 302-307, Apr. 1966.

[26] J. E. Greivenkamp, *Field Guide to Geometrical Optics*, Bellingham, WA: SPIE press, 2004, pp. 19-20.

[27] J. B. Keller, "Geometric Theory of Diffraction," *J.Opt.Soc.Am.,* vol. 52, no. 2, pp. 116-130, 1962.

[28] R. G. Kouyoumjian and P. H. Pathak, "A Uniform Geometrical Theory of Diffraction for An Edge in a Perfectly Conducting Surface," *Proc. IEEE,* vol. 62, no. 11, pp. 1448-1461, Nov. 1974.

[29] A. Toccafondi and R. Tiberio, "An incremental theory of double edge diffraction," *Radio Science,* vol. 42, no. 06, pp. 1-13, Dec. 2007.

[30] T. Lertwiriyaprapa, P. H. Pathak, and J. L. Volakis, "A uniform geometrical theory of diffraction for predicting fields of sources near or on thin planar positive/negative material discontinuities," *Radio Science,* vol. 42, no. 06, pp. 1-14, Dec. 2007.

[31] P. D. Holm, "UTD-diffraction coefficients for higher order wedge diffracted fields," *IEEE Trans. Antennas Propag.,* vol. 44, no. 6, pp. 879-888, June 1996.

[32] J. B. Andersen, "UTD multiple-edge transition zone diffraction," *IEEE Trans. Antennas Propag.,* vol. 45, no. 7, pp. 1093-1097, July 1997.

[33] J. -. Rouviere, N. Douchin, and P. F. Combes, "Diffraction by lossy dielectric wedges using both heuristic UTD formulations and FDTD," *IEEE Trans. Antennas Propag.,* vol. 47, no. 11, pp. 1702-1708, Nov. 1999.

[34] T. Griesser and C. Balanis, "Dihedral corner reflector backscatter using higher order reflections and diffractions," *IEEE Trans. Antennas Propag.,* vol. 35, no. 11, pp. 1235-1247, Nov. 1987.

[35] R. Paknys and D. R. Jackson, "The relation between creeping waves, leaky waves, and surface waves," *IEEE Trans. Antennas Propag.,* vol. 53, no. 3, pp. 898-907, Mar. 2005.

[36] G. Koutitas and C. Tzaras, "A UTD solution for multiple rounded surfaces," *IEEE Trans. Antennas Propag.,* vol. 54, no. 4, pp. 1277-1283, Apr. 2006.

[37] D. M. Hailu, I. A. Ehtezazi, M. Neshat, G. S. A. Shaker, and S. Safavi-Naeini, "Hybrid Spectral-Domain Ray Tracing Method for Fast Analysis of Millimeter-Wave and Terahertz-Integrated Antennas," *IEEE Trans. THz Sci. Technol.,* vol. 1, no. 2, pp. 425-434, Nov. 2011.

[38] K. Goto and L. H. Loc, "High-frequency asymptotic analysis for scattered field by a conducting cylinder," *in 2013 International Symposium on Electromagnetic Theory,* 2013, pp. 782-785.

[39] P. H. Pathak, G. Carluccio, and M. Albani, "The Uniform Geometrical Theory of Diffraction and Some of Its Applications," *IEEE Antennas Propag. Mag.,* vol. 55, no. 4, pp. 41-69, Aug. 2013.

[40] G. Koutitas and C. Tzaras, "A Slope UTD Solution for a Cascade of Multishaped Canonical Objects," *IEEE Trans. Antennas Propag.,* vol. 54, no. 10, pp. 2969-2976, Oct. 2006.

[41] R. Tiberio and R. Kouyoumjian, "Calculation of the high-frequency diffraction by two nearby edges illuminated at grazing incidence," *IEEE Trans. Antennas Propag.,* vol. 32, no. 11, pp. 1186-1196, Nov. 1984.

[42] R. J. Luebbers, "A heuristic UTD slope diffraction coefficient for rough lossy wedges," *IEEE Trans. Antennas Propag.,* vol. 37, no. 2, pp. 206-211, Feb. 1989.

[43] P. Pathak, W. Burnside, and R. Marhefka, "A uniform GTD analysis of the diffraction of electromagnetic waves by a smooth convex surface," *IEEE Trans. Antennas Propag.,* vol. 26, no. 5, pp. 631-642, Sep. 1980.

[44] P. Y. Ufimtsev, Fundamentals of the Physical Theory of Diffraction, Hoboken, New Jersey, pp. 1-48, Wiley, 2013.

[45] K. Hentschel and N. Y. Zhu, Gustav Robert Kirchhoff's Treatise "On The Theory Of Light Rays" (1882), World Scientific, 2017.

[46] C. Bourlier, G. Berginc, and J. Saillard, "The Kirchhoff analysis from one- and two-dimensional random surface with the statistical shadowing function," *in IGARSS 2001. Scanning the Present and Resolving the Future. Proceedings. IEEE 2001 International Geoscience and Remote Sensing Symposium (Cat. No.01CH37217),* 2001, pp. 2427-2429, vol. 5.

[47] C. Bourlier, N. Dechamps, and G. Berginc, "Electromagnetic scattering from rough surfaces with the first- and second-order Kirchhoff approximation in high-frequency limit," *in IGARSS 2003. 2003 IEEE International Geoscience and Remote Sensing Symposium. Proceedings (IEEE Cat. No.03CH37477),* 2003, pp. 115-117, vol. 1.

[48] Y. Du, J. A. Kong, W. Yan, Z. Wang, and L. Peng, "A Statistical Integral Equation Model for Shadow-Corrected EM Scattering From a Gaussian Rough Surface," *IEEE Trans. Antennas Propag.,* vol. 55, no. 6, pp. 1843-1855, June 2007.

[49] C. Yang and L. X. Guo, "Application of the Small Slope Approximation for EM Scattering from the Rough Sea Surface," *in 2008 International Conference on Microwave and Millimeter Wave Technology,* 2008, pp. 999-1002.

[50] Z. L. Wang, F. Xu, Y. Q. Jin, and H. Ogura, "A double Kirchhoff approximation for very rough surface scattering using the stochastic functional approach," *Radio Science,* vol. 40, no. 4, pp. 1-10, Aug. 2005.

[51] D. Comite, M. T. Falconi, P. Lombardo, F. S. Marzano, and A. Galli, "Investigating the shadow radiation of 3-dimensional radar targets in the near field," *in 2017 European Radar Conference*, 2017, pp. 17-20.

[52] P. T. C. Lam, S. W. Lee, and R. Acosta, Secondary Pattern Computation of an Arbitrarily Shaped Main Reflector, Cleveland, Ohio, USA: Lewis Research Center, Nov. 1984.

[53] B. J. Dean and P. C. Pedersen, "Angular spectrum based formulation of rough surface scattering with applications to surface characterization," *in 1996 IEEE Ultrasonics Symposium. Proceedings,* 1996, pp. 693-696, vol. 1.

[54] R. Zhang and L. Cai, "A packet-level model for UWB channel with people shadowing process based on angular spectrum analysis," *IEEE Trans. Wireless Commun.,* vol. 8, no. 8, pp. 4048-4055, Aug. 2009.

[55] F. Varray, A. Ramalli, C. Cachard, P. Tortoli, and O. Basset, "Fundamental and second-harmonic ultrasound field computation of inhomogeneous nonlinear medium with a generalized angular spectrum method," *IEEE Trans. Ultrason., Ferroelectr., Freq. Control,* vol. 58, no. 7, pp. 1366-1376, July 2011.

[56] U. Vyas and D. Christensen, "Ultrasound beam simulations in inhomogeneous tissue geometries using the hybrid angular spectrum method," *IEEE Trans. Ultrason., Ferroelectr., Freq. Control,* vol. 59, no. 6, pp. 1093-1100, June 2012.

[57] T. Okamoto, "2.5D higher order ambisonics for a sound field described by angular spectrum coefficients," *in 2016 IEEE International Conference on Acoustics, Speech and Signal Processing (ICASSP),* 2016, pp. 326-330.

[58] A. Haniz, T. Matsumura, and F. Kojima, "Efficient Joint Sensing of Sparse Angular-Frequency Spectrum based on Compressive Sensing," *in 2020 IEEE 31st Annual International Symposium on Personal, Indoor and Mobile Radio Communications,* 2020, pp. 1-7.

[59] H. Peng, "A New Model of Ultrasonic Imaging System Based on Plane Wave Transmission and Angular Spectrum Propagation Principle," *in 2007 IEEE International Conference on Integration Technology,* 2007, pp. 307-310.

[60] M. Pasovic, M. Danilouchkine, P. van Neer, O. Basset, C. Cachard, A. F. W. van der Steen, and N. de Jong, Nico, "Angular spectrum method for the estimation of the lateral profile of the ultrasound pressure field of the third harmonic," *in 2009 IEEE International Ultrasonics Symposium,* 2009, pp. 2801-2804.

[61] C. D. Arvanitis, C. Crake, N. McDannold, and G. T. Clement, "Passive Acoustic Mapping with the Angular Spectrum Method," *IEEE Trans. Med. Imag.,* vol. 36, no. 4, pp. 983-993, Apr. 2017.

[62] J. Puskely and Z. Novacek, "Comparison of different approaches for reconstruction of radiation patterns," *in 15th Conference on Microwave Techniques COMITE 2010,* 2010, pp. 199-202.

[63] C. Hung and R. Mittra, "Secondary pattern and focal plane distribution of reflector antennas under wide angle scanning," *in 1982 Antennas and Propagation Society International Symposium,* 1982, pp. 616-619.

[64] Y. V. Krivosheev, A. V. Shishlov, A. K. Tobolev, and I. L. Vilenko, "Fresnel field to far field transformation using sparse field samples," *in 2012 International Conference on Mathematical Methods in Electromagnetic Theory,* 2012, pp. 237-242.

[65] M. E. Yanik and M. Torlak, "Near-Field MIMO-SAR Millimeter-Wave Imaging With Sparsely Sampled Aperture Data," *IEEE Access,* vol. 7, pp. 31801-31819, 2019.

[66] A. W. Glisson, "Equivalent current excitation for an aperture antenna embedded in an arbitrarily shaped impedance surface," *IEEE Trans. Antennas Propag.,* vol. 50, no. 7, pp. 966-970, July 2002.

[67] M. A. Maisto, G. Leone, A. Brancaccio, and R. Solimene, "Efficient Planar Near-Field Measurements for Radiation Pattern Evaluation by a Warping Strategy," *IEEE Access,* vol. 9, pp. 62255-62265, 2021.

[68] R. J. Pogorzelski, "Full Hemisphere Aperture-Antenna Far-Field Patterns From Planar Near-Field Measurements," *IEEE Trans. Antennas Propag.,* vol. 67, no. 2, pp. 1170-1179, Feb. 2019.

[69] S. Oh and J. Yun, "New Method for Predicting the Electromagnetic Field at a Finite Distance Using Fresnel Field Transformation," *IEEE Antennas Wireless Propag. Lett.,* vol. 7, pp. 291-293, 2008.

[70] Z. H. Firouzeh, A. Zeidaabadi-Nezhad, and H. Mirmohammad-Sadeghi, "An Optimum Meshing to Compute The Radiation Integrals of Reflector Antennas by FFT Method," *in 2007 Asia-Pacific Microwave Conference,* 2007, pp. 1-4.

[71] Y. Kan, Y. Zhu, L. Tang, and Q. Fu, "Fast integral method for near-field cross section imaging at millimeter wave," *in 2016 CIE International Conference on Radar (RADAR),* 2016, pp. 1-4.

[72] A. W. Mathis and A. F. Peterson, "Efficient electromagnetic analysis of a doubly infinite array of rectangular apertures," *IEEE Trans. Microw. Theory Techn.,* vol. 46, no. 1, pp. 46-54, Jan. 1998.

[73] A. Yaghjian, "An overview of near-field antenna measurements," *IEEE Trans. Antennas Propag.,* vol. 34, no. 1, pp. 30-45, Jan. 1986.

[74] D. S. Jones, "Diffraction by a thick semi-infinite plate," *Proc. Roy. Soc. London,* Ser. A, vol. 217, pp. 153-175, 1953.

[75] K. K. Mei and J. G. Van Bladel, "Scattering by perfectly conducting rectangular cylinders," *IEEE Trans. Antennas Propag.,* vol.11, pp. 185-192, 1963.

[76] W. D. Burnside, C. L. Yu, and R. J. Marhefka, "A technique to combine the geometrical theory of diffraction and the moment method," *IEEE Trans. Antennas Propag.,* vol. 23, pp. 551-558, 1975.

[77] R. Mittra and S. W. Lee, Analytical Techniques in the Theory of Guided Waves, Macmillan, 1971.

[78] M. Plonus, R. Williams, and S. Wang, "Radar cross section of curved plates using geometrical and physical diffraction techniques," *IEEE Trans. Antennas Propag.,* vol. 26, no. 3, pp. 488-493, May 1978.

[79] D. -. Duan, Y. Rahmat-Samii, and J. P. Mahon, "Scattering from a circular disk: a comparative study of PTD and GTD techniques," *Proc. IEEE,* vol. 79, no. 10, pp. 1472-1480, Oct. 1991.

[80] M. Ando and T. Kinoshita, "PO and PTD analyses in polarization prediction for plane wave diffraction from a large circular disk," *in Digest on Antennas and Propagation Society International Symposium,* 1989, pp. 1282-1285, vol. 3.

[81] Dah-Weih Duan and Yahya Rahmat-Samii, "A generalized diffraction synthesis technique for high performance reflector antennas," *IEEE Trans. Antennas Propag.,* vol. 43, no. 1, pp. 27-40, Jan. 1995.

[82] U. Jakobus and F. M. Landstorfer, "Improved PO-MM hybrid formulation for scattering from three-dimensional perfectly conducting bodies of arbitrary shape," *IEEE Trans. Antennas Propag.,* vol. 43, no. 2, pp. 162-169, Feb. 1995.

[83] D. -. Duan and Y. Rahmat-Samii, "Axial field of a symmetric paraboloidal antenna: a PO/PTD solution," *in Proceedings of IEEE Antennas and Propagation Society International Symposium and URSI National Radio Science Meeting,* 1994, pp. 38-41, vol. 1.

[84] U. Jakobus and F. M. Landstorfer, "Improvement of the PO-MoM hybrid method by accounting for effects of perfectly conducting wedges," *IEEE Trans. Antennas Propag.,* vol. 43, no. 10, pp. 1123-1129, Oct. 1995.

[85] H. H. Syed and J. L. Volakis, "PTD analysis of impedance structures," *IEEE Trans. Antennas Propag.,* vol. 44, no. 7, pp. 983-988, July 1996.

[86] Shyh-Kang Jeng, "Near-field scattering by physical theory of diffraction and shooting and bouncing rays," *in IEEE Antennas and Propagation Society International Symposium 1997. Digest, 1997,* pp. 1176-1179, vol. 2.

[87] R. L. Eigel, A. J. Terzuoli, and G. Nesti, "Bistatic scattering characterization of a complex object," *in IEEE 1999 International Geoscience and Remote Sensing Symposium. IGARSS'99 (Cat. No.99CH36293),* 1999, pp. 455-457, vol. 1.

[88] A. Michaeli, "Equivalent edge currents for arbitrary aspects of observation," *IEEE Trans. Antennas Propag.,* vol. 32, no. 3, pp. 252-258, Mar. 1984.

[89] Dong-Ho Han, A. C. Polycarpou, and C. A. Balanis, "Hybrid analysis of reflector antennas including higher order interactions and blockage effects," *IEEE Trans. Antennas Propag.,* vol. 50, no. 11, pp. 1514-1524, Nov. 2002.

[90] T. Shijo, L. Rodriguez, and M. Ando, "The Modified Surface-Normal Vectors in the Physical Optics," *IEEE Trans. Antennas Propag.,* vol. 56, no. 12, pp. 3714-3722, Dec. 2008.

[91] P. Y. Ufimtsev, "The 50-Year Anniversary Of the PTD: Comments on the PTD's Origin and Development," *IEEE Antennas Propag. Mag.,* vol. 55, no. 3, pp. 18-28, June 2013.

[92] W. Huang, Z. Zhao, R. Zhao, J. Wang, Z. Nie, and Q. H. Liu, "GO/PO and PTD With Virtual Divergence Factor for Fast Analysis of Scattering From Concave Complex Targets," *IEEE Trans. Antennas Propag.,* vol. 63, no. 5, pp. 2170-2179, May 2015.

[93] T. Fan, L. Guo, B. Lv, and W. Liu, "An Improved Backward SBR-PO/PTD Hybrid Method for the Backward Scattering Prediction of an Electrically Large Target," *IEEE Antennas Wireless Propag. Lett.,* vol. 15, pp. 512-515, 2016.

[94] Z. Liu and C. Wang, "Closed-form PO-PTD solution for fast electromagnetic scattering prediction," *in 2015 IEEE 5th Asia-Pacific Conference on Synthetic Aperture Radar (APSAR),* 2015, pp. 477-480.

[95] T. Fan, L. Guo, and Z. Liu, "SBR-PO/PTD method for backward scattering of airplane model and application to ISAR image," *in 2015 Asia-Pacific Microwave Conference (APMC),* 2015, pp. 1-3.

[96] G. Apaydin, F. Hacivelioglu, L. Sevgi, W. B. Gordon, and P. Y. Ufimtsev, "Diffraction at a Rectangular Plate: First-Order PTD Approximation," *IEEE Trans. Antennas Propag.,* vol. 64, no. 5, pp. 1891-1899, May 2016.

[97] J. Liu and L. Guo, "Computation of scattering from the convex surfaces with PTD-SPM," *in 2016 IEEE MTT-S International Conference on Numerical Electromagnetic and Multiphysics Modeling and Optimization (NEMO),* 2016, pp. 1-2.

[98] G. Apaydin, L. Sevgi, and P. Y. Ufimtsev, "Extension of PTD for Finite Objects With Rounded Edges: Diffraction at a Soft Trilateral Cylinder," *IEEE Antennas Wireless Propag. Lett.,* vol. 16, pp. 2590-2593, 2017.

[99] S. Haykin and M. Moher, Modern wireless communications, pp. 24-29, Library of Congress Cateloging-in-Publication, 2003.

[100] Les Barclay, Propagation of Radiowaves, pp.129-138, publisher.Institute of Engineering and Technology, London, United Kingdom. Second edition 2003.

[101] K. Buiilington, "Radio Propagation at Frequencies above 30 Megacycles," *Proc. IRE,* vol. 35, issue. 10, pp. 1122-1136, Oct. 1947.

[102] M. Levy, Parabolic Equation Methods for Electromagnetic Wave Propagation, UK: IET, Jan. 2000, p. 184.

[103] M. D. Feit and J. A. Fleck, "Calculation of dispersion in graded-index multimode fibers by a propagating-beam method," *Appl. Opt,* vol. 18, no. 16, pp. 2843-2851, Aug. 1979.

[104] F. J. Harris, "On the use of windows for harmonic analysis with the discrete Fourier transform," *Proc. IEEE*, vol. 66, no. 1, pp. 51-83, Jan. 1978.

[105] H. Hu, Z. Chen, S. Chai, and J. Mao, "Research on mobile communication radio propagation characteristic based on 3DPE," *in 2005 Asia-Pacific Microwave Conference Proceedings*, Hong Kong, 2005, p. 3.

[106] P. Zhang, L. Bai, Z. Wu, and F. Li, "Effect of window function on absorbing layers top boundary in parabolic equation," *in Proceedings of 2014 3rd Asia-Pacific Conference on Antennas and Propagation*, Harbin, China, 2014, pp. 849-852.

[107] H. F. Rasool, X. Pan, and X. Sheng, "Radiowave propagation prediction in the presence of multiple knife edges using 3D parabolic equation method," *in 2018 International Applied Computational Electromagnetics Society Symposium*, China, 2018, pp. 1-2.

[108] L. Guo and X. Guan, "A vector parabolic equation method for propagation predictions over 3-D irregular terrains," *in 2018 IEEE International Conference on Computational Electromagnetics*, 2018, pp. 1-4.

[109] T. Kohama and M. Ando, "Localization of Radiation Integrals Using the Fresnel Zone Numbers," *IEICE Trans. Elec.,* vol. 95, no. 5, pp. 928-935, 2012.

[110] T. Kohama, K. Ito, and M. Ando, "Abbreviated analysis of electromagnetic fields based upon locality of scattering phenomena," *in 2011 IEEE International Conference on Microwave Technology and Computational Electromagnetics,* 2011, pp. 372-375.

[111] M. Ando, T. Kohama, K. Ito, T. Shijo, T. Hirano, and J. Hirokawa, "High frequency locality embodied in terms of Fresnel zone number for matrix size reduction in method of moments," *in 2011 International Conference on Electromagnetics in Advanced Applications,* 2011, pp. 1432-1435.

[112] M. Ando, P. Lu, and T. Kohama, "Discussion of physical optics surface integration for deep interpretation of GTD," *in 2012 IEEE-APS Topical Conference on Antennas and Propagation in Wireless Communications (APWC),* 2012, pp. 1141-1144.

[113] M. Ando, M. Ali, P. Lu, and T. Kohama, "Application of fresnel zone numbers localization for equivalent edge currents line integration," *in 2013 International Symposium on Electromagnetic Theory,* 2013, pp. 1061-1063.

[114] T. Kohama and M. Ando, "Novel techniques for abbreviated analysis of high frequency scattering using the fresnel zone numbers," *in 2013 IEEE Antennas and Propagation Society International Symposium (APSURSI),* 2013, pp. 1894-1895.

[115] J. R. Kuttler and R. Janaswamy, "Improved Fourier transform methods for solving the parabolic wave equation," *Radio Science,* vol. 37, no. 2, pp. 1-11, Apr. 2002.

[116] X. Guan, L. Guo, Q. Li, and Y. Wang, "A 3D parabolic equation method for knife-edge diffraction modeling," *in 2017 International Applied Computational Electromagnetics Society Symposium,* 2017, pp. 1-2.

[117] X. Han, J. Li, C. Jing, and Z. Fang, "A 3D parabolic equation model with higher-order operator approximation," *in Global Oceans 2020: Singapore - U.S. Gulf Coast,* 2020, pp. 1-5.

[118] B. Roa and L. Carin, "A hybrid (parabolic equation)-(Gaussian beam) algorithm for wave propagation through large inhomogeneous regions," *IEEE Trans. Antennas Propag.,* vol. 46, no. 5, pp. 700-709, May 1998.

[119] N. Noori, S. Safavi-Naeini, and H. Oraizi, "A new three-dimensional vector parabolic equation approach for modeling radio wave propagation in tunnels," *in 2005 IEEE Antennas and Propagation Society International Symposium,* 2005, pp. 314-317, vol. 4B.

[120] G. Apaydin and L. Sevgi, "A Novel Split-Step Parabolic-Equation Package for Surface-Wave Propagation Prediction Along Multiple Mixed Irregular-Terrain Paths," *IEEE Antennas Propag. Mag.,* vol. 52, no. 4, pp. 90-97, Aug. 2010.

[121] C. A. Zelley and C. C. Constantinou, "A three-dimensional parabolic equation applied to VHF/UHF propagation over irregular terrain," *IEEE Trans. Antennas Propag.,* vol. 47, no. 10, pp. 1586-1596, Oct. 1999.

[122] Z. He and R. S. Chen, "A Vector Meshless Parabolic Equation Method for Three-Dimensional Electromagnetic Scatterings," *IEEE Trans. Antennas Propag.,* vol. 63, no. 6, pp. 2595-2603, June 2015.

[123] L. Guo and X. Guan, "A Vector Parabolic Equation Method for Propagation Predictions Over 3-D Irregular Terrains," *in 2018 IEEE International Conference on Computational Electromagnetics (ICCEM),* 2018, pp. 1-4.

[124] D. Dockery and J. R. Kuttler, "An improved impedance-boundary algorithm for Fourier split-step solutions of the parabolic wave equation," *IEEE Trans. Antennas Propag.,* vol. 44, no. 12, pp. 1592-1599, Dec. 1996.

[125] M. A. N. da Silva, E. Costa, and M. Liniger, "Analysis of the effects from lateral variations of irregular terrain based on a three-dimensional parabolic equation," *in Proceedings of the Fourth European Conference on Antennas and Propagation,* 2010, pp. 1-4.

[126] M. A. N. Silva, E. Costa, and M. Liniger, "Analysis of the Effects of Irregular Terrain on Radio Wave Propagation Based on a Three-Dimensional Parabolic Equation," *IEEE Trans. Antennas Propag.,* vol. 60, no. 4, pp. 2138-2143, Apr. 2012.

[127] X. Guan, L. Guo, Y. Wang, and Q. Li, "Applying perfectly absorbing thin screen to the 3D parabolic equation method," *in 2017 Sixth Asia-Pacific Conference on Antennas and Propagation (APCAP),* 2017, pp. 1-3.

[128] G. Apaydin and L. Sevgi, "Calibration of Three-Dimensional Parabolic-Equation Propagation Models with the Rectangular Waveguide Problem," *IEEE Antennas Propag. Mag.,* vol. 54, no. 6, pp. 102-116, Dec. 2012.

[129] J. R. Kuttler, "Differences between the narrow-angle and wide-angle propagators in the split-step Fourier solution of the parabolic wave equation," *IEEE Trans. Antennas Propag.,* vol. 47, no. 7, pp. 1131-1140, July 1999.

[130] Z. E. Ahdab and F. Akleman, "Groundwave propagation in a nonhomogeneous atmosphere: Prediction using 3D parabolic equation," *in 2017 International Applied Computational Electromagnetics Society Symposium - Italy,* 2017, pp. 1-2.

[131] M. S. Lytaev, "Higher-order 3D Parabolic Equation for Radio Wave Propagation Modeling in a Street Canyon," *in 2019 IEEE Conference of Russian Young Researchers in Electrical and Electronic Engineering (EIConRus),* 2019, pp. 873-876.

[132] M. F. Levy, "Horizontal parabolic equation solution of radiowave propagation problems on large domains," *IEEE Trans. Antennas Propag.,* vol. 43, no. 2, pp. 137-144, Feb. 1995.

[133] O. Benhmammouch, N. Caouren, and A. Khenchaf, "Modeling of roughness effects on electromagnetic waves propagation above sea surface using 3D parabolic equation," *in 2009 IEEE International Geoscience and Remote Sensing Symposium,* 2009, pp. II-817-II-820.

[134] C. Tang, L. Fu, W. Pan, Q. Li, and J. Huang, "Optimized Pseudo-Pad Fourier Migrator in Terms of Propagation Angles," *IEEE Access,* vol. 8, pp. 32054-32065, 2020.

[135] R. Janaswamy, "Path loss predictions in the presence of buildings on flat terrain: a 3-D vector parabolic equation approach," *IEEE Trans. Antennas Propag.,* vol. 51, no. 8, pp. 1716-1728, Aug. 2003.

[136] Z. El Ahdab and F. Akleman, "Radiowave Propagation Analysis With a Bidirectional 3-D Vector Parabolic Equation Method," *IEEE Trans. Antennas Propag.,* vol. 65, no. 4, pp. 1958-1966, Apr. 2017.

[137] R. Zhang, H. Wang, and L. Zhang, "Study on Fourier transform methods in A 3-D parabolic equation," *in 2014 XXXIth URSI General Assembly and Scientific Symposium (URSI GASS),* 2014, pp. 1-4.

[138] J. R. Wait, "The scope of impedance boundary conditions in radio propagation," *IEEE Trans. Geosci. Remote Sens.,* vol. 28, no. 4, pp. 721-723, July 1990.

[139] G. Apaydin and L. Sevgi, "Two-Way Propagation Modeling in Waveguides With Three-Dimensional Finite-Element and Split-Step Fourier-Based PE Approaches," *IEEE Antennas Wireless Propag. Lett.,* vol. 10, pp. 975-978, 2011.

[140] C. V. Aviloff, "Two-way solution of underwater sound propagation problem in two- and three-dimensional environment by pseudodifferential parabolic equation technique," *in Proceedings of OCEANS'94,* 1994, pp. III/159-III/162, vol. 3.

[141] Y. Liu, Z. Zeng, X. Liu, and Z. He, "Wave Propagation Modeling in Curved Tunnels with Three-Dimensional ADI-PE Method," *in 2020 IEEE MTT-S International Conference on Numerical Electromagnetic and Multiphysics Modeling and Optimization (NEMO),* 2020, pp. 1-3.

[142] C. A. Balanis, Antenna Theory, Hoboken, New Jersey, USA: Wiley, 2016, pp. 620-637.

[143] G. Apaydin and L. Sevgi, Radio Wave Propagation and Parabolic Equation Modeling, Hoboken, New Jersey, USA: Wiley-IEEE Press, 2017.

[144] X. Du, K. Saito, J. Takada, and P. Hanpinitsak, "A Novel Mirror Kirchhoff Approximation Method for Predicting the Shadowing Effect by a Metal Cuboid," *Progress In Electromagnetics Research M*, vol. 104, no. 18, pp. 199-212, Sep. 2021.

[145] W. H. Southwell, "Validity of the Fresnel approximation in the near field," *JOSA,* vol. 71, no. 1, pp. 7-14, 1981.

[146] X. Du and J. Takada, "Mirror Kirchhoff Approximation for Predicting Shadowing Effect by a PEC Convex Cylinder," *in 2021 International Applied Computational Electromagnetics Society Symposium,* Hamilton, Canada, Aug. 2021.

[147] P. Pathak, "An asymptotic analysis of the scattering of plane waves by a smooth convex cylinder," *Radio Science,* vol. 14, no. 3, pp. 419-435, June 1979.

[148] C. A. Balanis, *Advanced Engineering Electromagnetics*, Wiley, Hoboken, New Jersey, Chapters 6 and 7, 2012.

[149] A. Ludwig, "Computation of Radiation Patterns Involving Numerical Double Integration," *IEEE Trans. Antennas Propag.*, vol. 16, no. 6, pp. 767-769, 1968.

[150] Y. Oguma, T. Nishio, K. Yamamoto, and M. Morikura, "Implementation and evaluation of reactive base station selection for human blockage in mmWave communications," *in 2015 21st Asia-Pacific Conference on Communications*, 2015, pp. 199-203.

[151] Y. Oguma, T. Nishio, K. Yamamoto, and M. Morikura, "Performance modeling of camera-assisted proactive base station selection for human blockage problem in mmWave communications," *in 2016 IEEE Wireless Communications and Networking Conference*, 2016, pp. 1-7.

Publications

Journal

1. X. Du, K. Saito, J. Takada, and P. Hanpinitsak, "A Novel Mirror Kirchhoff Approximation Method for Predicting the Shadowing Effect by a Metal Cuboid," *Progress In Electromagnetics Research M*, vol. 104, no. 18, pp. 199-212, Sep. 2021.

2. X. Du and J. Takada, "Low computational cost Mirror Kirchhoff Approximation for Predicting Shadowing Effect," *IEEE Access*, accepted.

International Conference

1. X. Du, K. Saito, J. Takada, M. Nakamura, M. Sasaki, and Y. Takatori, "Shadowing Measurement of Various Obstacles on Millimeter-Wave Bands in Indoor Environment," *in 2018 Asian Workshop on Antennas and Propagation*, AVANI Pattaya Resort, Pattaya, Thailand, July 2018.

2. X. Du, K. Saito, J. Takada, and P. Hanpinitsak, "A Novel Mirror Kirchhoff Approximation Method for Predicting the Shadowing Effect by a Metal Cuboid," *in 2nd Post European Cooperation in Science and Technology (COST) Inclusive Radio Communication Networks for 5G and Beyond (Post-IRACON) Meeting*, online, EURACON, Feb. 2021.

3. X. Du and J. Takada, "Mirror Kirchhoff Approximation for Predicting Shadowing Effect by a PEC Convex Cylinder," *in 2021 The Applied Computation Electromagnetics Society*, online, Hamilton, Canada, Aug. 2021.

4. X. Du, K. Saito, J. Takada, and P. Hanpinitsak, "A Novel Mirror Kirchhoff Approximation Method for Predicting Shadowing Gain," *in XXXIV General Assembly and Scientific Symposium (GASS) of the International Union of Radio Science*, online, Rome, Italy, Aug. 2021.

Domestic Conference

1. 杜 キン, 平野 拓一, 齋藤 健太郎, 高田 潤一, 電波伝播測定用5GHz帯方形パッチアンテナの設計, 平成29年度電子情報通信学会東京支部学生会研究発表会, B-1, no.52, 東海大学高輪キャンパス (Tokai Univ.), 東京, 2017年3月. X. DU, T. HIRANO, K. SAITO, and J. TAKADA, "Design of a Rectangular Patch Antenna for Radio Propagation

Measurement ," *in 2017 IEICE Tokyo Section Student Activity Committee,* B-1, no.52, Tokai Univ., Tokyo, Mar. 2017.

2. 杜 キン, 齋藤 健太郎, 高田 潤一, 中村 光貴, 佐々木 元晴, 鷹取 泰司, 屋内環境におけるミリ波帯伝搬チャネルの障害物による遮蔽損失特性, 電子情報通信学会 信学技報, vol. 117, no. 382, AP2017-155, pp. 25-29, 国際電気通信基礎技術研究所 (ATR), 京都, 2018 年 1 月. X. Du, K. Saito, J. Takada, M. Nakamura, M. Sasaki, and Y. Takatori, "Shadowing Effect of Obstacles on Millimeter-wave Band Propagation Channel in Indoor Environment," *in IEICE Tech. Rep.,* vol. 117, no. 382, AP2017-155, pp. 25-29, ATR, Kyoto, Jan. 2018.

3. 杜 キン, 齋藤 健太郎, 高田 潤一, 中村 光貴, 佐々木 元晴, 鷹取 泰司, 屋内環境におけるミリ波帯伝搬チャネルの障害物による遮蔽損失特性, 日本学術会議 電気電子工学委員会 URSI 分科会 非電離媒質伝搬・リモートセンシング小委員会, NTT ドコモ R & D センタ (NTT), 横須賀, 2018 年 3 月. X. Du, K. Saito, J. Takada, M. Nakamura, M. Sasaki, and Y. Takatori, "Shadowing Effect of Obstacles on Millimeter-wave Band Propagation Channel in Indoor Environment," *in INTERNATIONAL UNION OF RADIO SCIENCE Commission F Japanese Committee,* NTT, Yokosuka, Mar. 2018.

4. 杜 キン, 齋藤 健太郎, 高田 潤一, 中村 光貴, 山田 渉, 鷹取 泰司, ミリ波帯伝搬チャネルにおける物理光学近似に基づく遮蔽損失の予測手法, 電子情報通信学会 信学技報, vol. 118, no. 504, AP2018-192, pp. 35-40, 旅館湯乃家 （Yunoya）, 福島, 2019 年 3 月. X. Du, K. Saito, J. Takada, M. Nakamura, W. Yamada, and Y. Takatori, "Shadowing Effect Prediction based on Physical Optics Approach for Millimetre Wave Mobile Communication," *in IEICE Tech. Rep.,* vol. 118, no. 504, AP2018-192, pp. 35-40, Yunoya, Fukushima, Mar. 2019.

5. 杜 キン, 齋藤 健太郎, 高田 潤一, 中村 光貴, 山田 渉, 鷹取 泰司, ミリ波帯伝搬における見通し波遮蔽損失の実験及び予測手法, 2019 年度 IEICE ソサイエティ大会, 大阪大学豊中キャンパス (Osaka Univ.), 大阪, 2019 年 9 月. X. Du, K. Saito, J. Takada, M. Nakamura, W. Yamada, and Y. Takatori, "Measurement and Prediction Models for Obstruction Losses of Line-of-sight Wave in the Millimeter Wave Band," *in 2019 IEICE Society Conference,* Osaka Univ., Osaka, Sep. 2019.

6. 杜 キン, 齋藤 健太郎, 高田 潤一, 中村 光貴, 山田 渉, 鷹取 泰司, ミリ波帯において見通し線上における障害物による遮蔽損失の解析手法と実験, 革新的無線通信技術に関する横断型研究会, 北海道大学 (Hokkaido Univ.), 札幌, 2019 年 10 月. X. Du, K. Saito, J. Takada, M. Nakamura, W. Yamada, and Y. Takatori, "Measurement and Prediction Models of the Line-of-sight Obstruction Losses at Millimeter Wave Radio," *in Multiple Innovative Kenkyu-kai Association for wireless communication,* Hokkaido Univ., Sapporo, Oct. 2019.

7. 杜 キン, 齋藤 健太郎, 高田 潤一, 中村 光貴, 山田 渉, 鷹取 泰司, 東京工業大学環境・社会理工学院融合理工学系高田研究室, Microwave Workshops and Exhibition, パシフィコ横浜 (Pacifico), 横浜, 2019 年 11 月.

8. X. Du and J. Takada, "Low Computational Cost Kirchhoff Approximation for Single Diffraction Problem," *in 2022 IEICE General Conference,* online, Mar. 2022, submitted.

Patent

1. 杜 キン, 齋藤 健太郎, 高田 潤一, 中村 光貴, 鷹取 泰司, 守山 貴庸, 山田 渉, 久野 伸晃, 厚みのある遮蔽物による電波遮蔽損失計算方法及び装置, 特願 2020-135647, 2020 年.

Award

1. Student Paper Competition - Honorable Mention Award, in *ACES*, Aug. 2021.